UC Merced
UC Merced Electronic Theses and Dissertations

Title
Engineering 3D Nanostructures for a Multitude of Applications

Permalink
https://escholarship.org/uc/item/30f1b9fc

Author
Flores, Jose Fernando

Publication Date
2015

Copyright Information
This work is made available under the terms of a Creative Commons Attribution License, availalbe at https://creativecommons.org/licenses/by/4.0/

Peer reviewed|Thesis/dissertation

UNIVERSITY OF CALIFORNIA, MERCED

Engineering 3D Nanostructures for a Multitude of Applications

A Thesis submitted in partial satisfaction of the requirements for the degree of
Master of Science

in

Biological Engineering and Small-scale Technologies

by

Jose Fernando Flores

Committee in charge:
Professor Jennifer Q. Lu, Chair
Professor Sayantani Gosh
Professor Min-Hwan Lee

2015

Signature Page

The Thesis of Jose Fernando Flores is approved, and it is acceptable in quality and form for publication on microfilm and electronically:

_____
Associate Professor Sayantani Ghosh

_____
Assistant Professor Min-Hwan Lee

_____
Associate Professor Jennifer Q. Lu   Chair

UNIVERSITY OF CALIFORNIA, MERCED.
2015

Dedications:

With God's blessing:

> The work, energy, and time that it took to reach this checkpoint could not be possible without the infinite support and encouragement of my ever hardworking grandparents, **Zoila G. Lopez** and **Salomon A. Lopez**, and my dear mother **Lucrecia M. Lopez Galindo**. Although never present, they were the reminder that perseverance and hard work leads to advancement. To you I say - "*This merit is yours and not mine. Time for me to seek my own*"

> This odyssey may have never started without the kindness of a great friend and rival - *David Pan*. He, who in times of strangers, accepted my offer of help and introduced me to the one person that has single handedly (with headaches and disappointments) shaped me into a respectable scientist and man, and has now alter my future.

> To you, ***Jennifer Q. Lu***, *I heartedly dedicate this thesis.*

The Qur'an **(5:32)** says:

> And if any ***one*** saved a life - it would be as if he saved the life of ***all mankind***.

Contents

List of Figures

Acknowledgments

Abstract

Engineering 3D Nanostructures for a Multitude of Applications

Jose Fernando Flores

Biological Engineering and Small-scale Technologies

University of California, Merced.   2015

Professor Jennifer Q. Lu — Chair

Architectures of 3D hierarchical nanostructure arrays consisting of 1D nanostructures offers a large surface area and an unobstructed electron transport pathway which are of great technological importance for energy applications. I have developed nanomanufacturing methods to consistently and reproducibly obtain 3D hierarchical architectures through the controllable synthesis of 1D zinc oxide (ZnO) and carbon nanofibers. I have demonstrated that by adjusting the catalyst properties, engineered 3D morphologies of ZnO and carbon nanofibers can be achieved on metal current collectors. Three approaches were generated to produce such hierarchical structures, using as-synthesized 1D nanostructures as scaffolds, and I have used a multi-pronged approach to functionalize these 3D surfaces. By oxidation of a few layers of outer carbon, quinone functional groups can be formed by air annealing. As a result, more than 100% enhancement in energy storage capability has been observed. I have also developed polymer electrografting techniques, both on ZnO and on carbon surfaces. Using grafted polymers as templates, a N and O co-doped carbon layer is conformably deposited on carbon nanostructures. This new carbon heterostructure leads to a greatly enhanced oxygen reduction capability. With grafted polymer as template, I have successfully generated densely populated nanoparticles on ZnO nanowire surfaces. Rationally, these nanoparticles can be then used to grow 3D branched structures. Due to the greatly enhanced surface area, I have shown that the photoactivity of ZnO is increased both as an oxidant for dyes and for photoelectrochemical systems. This set of robust nanomanufacturing protocols are transformative and can served as platforms for a myriad of application such as future environmentally conscious energy technologies.

Chapter 1

Nanostructured Materials: Background and Motivation

1.1   1D Nanostructures

One-dimensional (1D) nanomaterials such as nanotubes and nanowires offer exciting properties resulting from radial confinement. The unconfined dimension along the length of 1D nanomaterials provides a path to communicate/manifest these properties. Their technological significances have been increasingly demonstrated.[1–11] Since the discovery of carbon nanotubes by Iijima[12] the interest for 1D nanomaterials has vastly increase. Both vapor transport-based and solution-based deposition techniques have been widely exploited for the growth of a variety of 1D nanomaterials.[6,11,13–17] In both cases the synthesis of nanostructures are dictated by *nucleation* and *growth*. Generally (non-catalyzed), as the concentrations of precursor units (atoms, ions, or molecules) increases, they aggregate forming nuclei or clusters through homogeneous *nucleation*. These clusters now serve as seeds for directed continuous *growth* in order to form larger nanostructures.

Catalysts seeds mainly play three important roles in nanostructure growth. First, they are heterogeneous nucleation sites where precursor units can deposit.[5,9,12,14] Secondly, they influence (catalyze) the decomposition of the precursor material into nanomaterial precipitates.[18–20] Third, they promote the precipitation of precursor for the nanomaterials due to limited solubility.[18,21,22] Consequently, they

influence diameter and directionality of growth due to their size and material properties.[15,19,20,22] These roles are influenced by catalysts crystallinity, lattice mismatch, elemental composition, preferential orientation, *etc.*

1.1.1   Thermodynamics on Nanostructures

Since catalyst are critical for nanostructure growth, especially 1D, it is important to understand their size limitations. Therefore the thermodynamic minimal radius of a nanostructure was calculated to be:

$$r_{min} = \frac{2\sigma_{LV}V_L}{RT\ln\sigma} = \frac{2\sigma_{LV}V_L}{\Delta\mu}$$

where σ_{LV} is the liquid-vapor surface free energy, V_L is the molar volume, R is the gas constant, T is the temperature, and σ is the vapor phase supersaturation.[23] Alternatively it can be represented in terms of the driving force where $\Delta\mu$ is the chemical potential difference between the precursor source and catalyst seed.[24] Although the minimal radius and growth rate ($\Delta\mu/RT$) can be estimated, other factors such as surface diffusion and heterogeneous seed catalysts need to be accounted for. These factors are critical and provide plausible explanations to enhanced growth rates and nanometer-scale diameters of some nanostructures. An important note to consider is that nanoparticle catalysts are extremely susceptible to the Gibbs-Thomson effect, which describes how the effective pressure in a liquid droplet is related to the curvature of the droplet — the Gibbs-Thomson equation is given bellow.[25] Decreasing the melting temperature, by consequence, would decrease the evaporation temperature. This melting point depression can further increase the activity of a nanocatalyst in much the same way that kinetics in liquid are faster than in solids. A drawback is that it can also evaporate away the nanocatalyst and prohibit growth.

"Gibbs-Thomson" Equation:

$$\Delta T_m(r) = T_{Bm} \, \frac{4\sigma_{SL}}{H_{Bf} \, \rho_S \, r}$$

where ΔT_m is the melting point depression, r is the particle radius, T_{Bm} is the bulk melting temperature, σ_{SL} is the solid-liquid surface free energy, H_{Bf} is the bulk enthalpy of fusion, and ρ_S is the density of solid.

1.1.2 Kinetics of Nanostructure Growth

To create a 1D nanostructures, the growth rate of a certain crystallographic plane must be larger than all other planes. The equal symmetry of crystal growth must be disturbed to allow unidirectional growth.[26] Here 1D growth refers to the fast growth rate along the vertical "c-axis" direction, and a much slower lateral "a-axis" and "b-axis".

A catalyst seed can break the symmetry of growth by providing a more energetically favorable nucleation site than the resultant nanostructure crystal. For example: Lets assume a crystal has symmetrical growth in all directions and a catalyst of a different material than the crystal is used; then the chemical potential between the catalyst and precursor source ($\Delta\mu_{C-S}$) is greater than the chemical potential between the precursor source and crystal ($\Delta\mu_{S-K}$); therefore, nanomaterial precursor is accommodated and precipitated preferentially by the catalyst instead of the crystal, thus the growth rate is expected to be fastest at the catalyst-crystal interface, because the chemical potential of catalyst and crystal ($\Delta\mu_{C-K}$) is greater than precursor-crystal ($\Delta\mu_{S-K}$). Wu, Y. and Yang, P. have demonstrated such catalytic growth phenomena with *in situ* TEM experiments of Ge nanowires using Au nanocatalyst.[27] This highlights the importance of catalysts in 1D nanostructure growth. One can see that adjustable nanostructure growth is possible by engineering catalysts.

Limited research in bimetallic nanocatalysis for 1D nanomaterial growth is due

to the lack of nanocatalyst synthesis capability. To achieve controllable synthesis, the first step is to establish a methodology to generate highly ordered and uniform sized nanocatalysts with tailored properties.

1.2   ZnO Nanostructures

Zinc oxide (ZnO) is a II-VI compound semiconductor with a direct band gap of around 3.4 eV (near-UV) and preferential wurtzite crystal structure.[28–30] Research in ZnO started around the 1930s but it faded out of interest partially due to the inability to dope as n- and p-type for optoelectronics.[28] New found interest in ZnO arose from the possibility to create nanostructures for UV optoelectronics, transparent conductive coatings, and spintronics applications. The challenge to achieve such applications is still p-type doping.[30]

Material wise, ZnO crystal structure is mainly wurtzite but a cubic zinc blende structure is also possible as shown in Figure 1.1. In wurtzite, one Zn-ion is surrounded tetrahedrally by four oxygen-ions and *vice versa* with lattice parameters $a = 0.3296$ and $c = 0.5207$ nm. Piezoelectricity in ZnO originates from the partial ionic bonding and lack of center of symmetry. Interestingly, ZnO has a strong tendency for self-organized growth. Under suitable conditions ZnO can grow into a multiple nanostructures, including quantum dots, tetrapods, combs, brushes, nails, tubes, walls, flowers, or propellers.[29,30] ZnO has three fast growth directions: $\langle 2\bar{1}\bar{1}0\rangle$, $\langle 01\bar{1}0\rangle$, and $\pm[0001]$, the last one being more prominent in 1D nanostructure growth.

Wurtzite　　　　　Cubic Zinc Blende
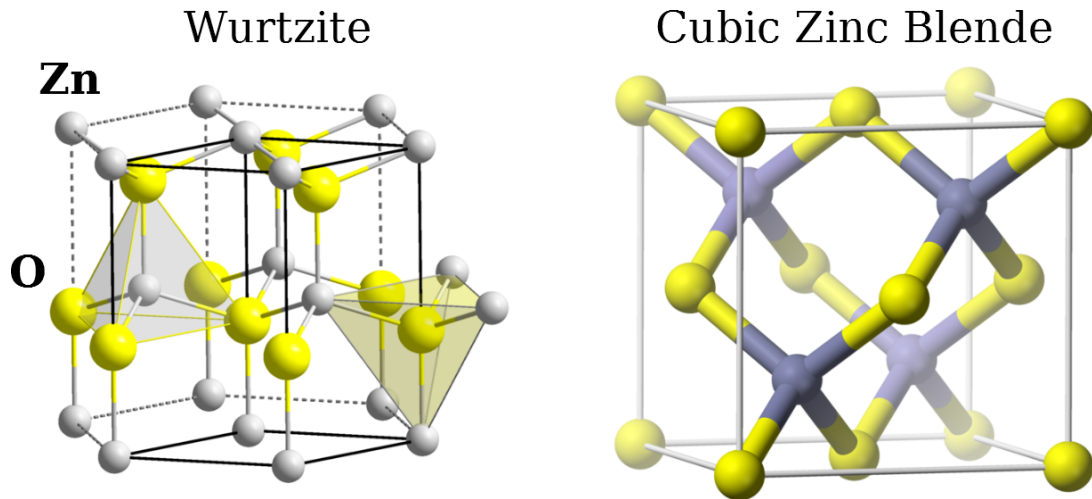
Figure 1.1: ZnO crystal structures models. Yellow spheres represent oxygen atoms, while gray and blue represent zinc atoms. (modified from Wikipedia)

ZnO is environmentally friendly and available; 10^5 tons per year are produced.[28] Currently, ZnO is utilized as an additive in concrete and tires, in cosmetics as a UV-blocking agent, and as a transparent oxide coating in windows to blocks UV-rays, and either block (cool) or reflect (heat) IR-light for energy savings. Future applications of ZnO include diodes, photonic devices including solar cells and water splitting, gas and biological sensors, piezoelectric devices, transparent conductive oxides, field emitters, and as dyes and toxins degradation photocatalyst.[28–31] Overcoming the drawbacks, such as a low charge carrier mobility, low thermal conductivity, and difficult p-type doping can open the gates to new ZnO based technologies. Additional disadvantages include, poor chemical stability in both strong acids and bases and a four-times stronger electron-phonon coupling when compared to GaN.[31] Nanostructures with a 3D architecture can provide the enhanced performance necessary to counterbalance ZnO drawbacks. The larger active surface area combined with 1D electron pathways would solve the mobility and conductivity issues.

1.3   Carbon Nanostructures

Carbon low cost, environmentally friendliness, stability, and light-weight make it a sought after material for energy applications. Depending on synthesis procedures a multitude of carbon nanostructures can be developed (Figure 1.2).[32] Graphitic nanostructures are highly desirable due to their high electron mobility at room temperature, a high specific surface area, a high thermal conductivity, excellent mechanic strength, *etc.* These properties are due to the carbon atoms being densely packed in a regular sp^2-bonded atomic-scale hexagonal pattern.[33] If connected graphitic structures are synthesized then the conductivity of carbon material would be excellent, which is the reason why efforts in graphene, nanotubes, fullerenes and their composites are often explored.
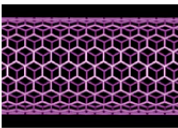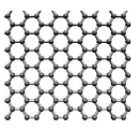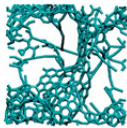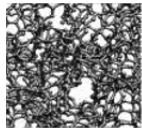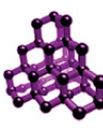
Material	Carbon onions	Carbon nanotubes	Graphene	Activated carbon	Carbide derived carbon	Templated carbon
Dimensionality	0D	1D	2D	3D	3D	3D
Conductivity	High	High	High	Low	Moderate	Low
Volumetric capacitance	Low	Low	Moderate	High	High	Low
Cost	High	High	Moderate	Low	Moderate	High
Structure						

Figure 1.2: Carbon nanostructures useful for energy applications. (Adapted from Jiang *et al.*[32])

The applications for carbon devices in energy systems include supercapacitors,[34,35] batteries (largely Li-ion),[36] dye-sensitized solar cells (DSSCs),[37] and fuel cells.[38,39] Nanocarbon-based materials have been widely studied as supercapacitor electrode materials, due to their high electrical conductivity, high surface area, and low cost. As supercapacitors, the porous structure of carbon nanostructures improves the accessibility of the electrolyte to the electrode surface, while providing electrically conductive channels which enhances the performance. By combining carbon nanostructures and pseudo-species, *e.g.*, transition metal oxides, redox reactions can be realized. The roles of carbon nanostructures include: increasing the specific loading of pseudo-species for higher energy density, enhanc-

ing the charge transport between pseudo-species and electrode for higher power and rate capabilities, and improving the adhesion of pseudo-species for enhanced cycling stability. Carbon nanostructures are ideal candidates as lithium-ion battery anodes because of high lithium storage capability and the robust structure for repeated charge/discharge cycles, with improved resistance to age degradation. The combination of the excellent electrical conductivity and the porous structure makes carbon nanostructures a promising anode/cathode material for building DSSCs with enhanced photovoltaic properties and superior performance. Carbon nanostructures for fuel cells are normally used as the catalyst support due to its high conductivity and large specific surface area, but additionally defected or doped carbons have shown good stand-alone catalytic activities. The non-agglomerated morphology and porous structure of carbon nanostructures facilitate the loading and dispersion of catalysts. Moreover, interconnected carbon networks promote fast electron transport between the reaction sites and the electrode.

The key features of carbon nanomaterials are their 3D porous structure and high electrical conductivity. These unique features have enabled various promising energy applications either independently or as composites. Better control of the structures (*e.g.*: porosity, surface area, conductivity, and thickness) by tuning the synthesis conditions and choosing appropriate catalyst precursors can potentially improve the overall performance of the carbon nanostructure or composite. Large-scale and low-cost fabrication of these materials and composites is another critical issue for their practical applications since most of the energy devices need a significant amount of materials for operation. Therefore the design of devices must be engineered starting at the synthesis level.

Aside from energy systems and due to their high specific surface area, tunable surface behavior, and high mechanical strength, carbon nanostructures can also been used in water remediation, such as the cleanup of oil and removal of heavy

metal ions and soluble organic contaminants. It is easy to imagine many more energy and environmental applications from carbon nanostructures will emerge in the near future.

1.4 Motivation — Controllable synthesis of 3D nanostructures

Inspiration is drawn by the ability of alloys to bring forth new technology break-throughs such as bronze, brass, and steels. I'm motivated by the results of intensive research performed on ZnO nanostructure growth utilizing monometallic catalyst.[13,21,40–44] I set forth to study bimetallics effect on ZnO nanostructure growth. Bimetallic catalysts research has shown capable of catalyzing reactions more efficiently than monometallic catalysts.[45] As consequence bimetallic alloys hold great potential to enhance the growth of ZnO nanostructures. The goal of the research was to first discover the effects of different bimetallic catalyst on morphology and second to find the limitations of catalytic growth. The objective was to manipulate the morphology and reduce the temperature of growth to allow for device integration.

One of 1D nanostructures major expected application is as energy devices. Semiconductors nanostructures in specific hold great potentials to be developed into advanced technological devices. The size of 1D nano-semiconductors alters many of their physical properties and the unconstrained dimension can direct the conduction of electrons, phonons, and photons.[4] Main applications of semiconductor 1D nanostructures are in photovoltaics, electrochemical energy storage (batteries), and thermoelectrics. ZnO has been sought out as a major player because of its physical and optoelectronic properties. Recent reports on carbon heterostructures enhancing photocatalytic activity inspired great interest to research more into the mechanisms behind enhancement. The goal focus on systematically

studying the photoactivity enhancements from processing and carbon coating. The objective was to develop a versatile photoelectrode for water splitting, water treatment, and solar cells.

The interest in control synthesis and manipulation of carbon nanostructures is due to the possibilities of developing synthesis methods that will allow the broad utilization of nanostrucutured carbon for commercial development. The focus being to provide materials for renewable energy systems. The goal was to develop a pluripotent platform for the consistent study of carbon nanomaterials in electrochemical systems, answering the challenge for comparison presented by the plethora of carbon systems that exist in literature. The objective was to synthesize a ready-to-use carbon electrode that would be stable even in harsh environments that normally accompany electrochemical systems.

> ***Focus of this thesis is the correlation and synergy of catalysts and 1D nanomaterial synthesis for energy systems***.

The efforts and accomplishments for these two are the essence of my research and are discussed in the following chapters. The format of the thesis follows a two part sequence, zinc oxide then carbon nanofibers, subdivided into chapters that focus on a specific phenomena/study.

Part I

Controlled Synthesis of ZnO Nanostructures

Chapter 2

Bimetallic Catalyst-Cocatalyst for ZnO Nanostructures Growth

It has been suggested that catalysts play a critical role for enabling 1D nanomaterial formation for vapor transport-based approach. This role is exemplified by the fact that single-walled carbon nanotubes (CNTs) cannot be readily produced without using catalyst nanoparticles.[46] Catalysts also provide an essential means to control diameter and crystal orientation.[15,18–22]

Over the years, two major categories have been established to generate catalysts nanoparticles. One is the vacuum based thin film deposition technique that includes ion sputtering deposition, e-beam or thermal evaporation, laser ablation and molecular beam epitaxy. All these methods have been proven to be effective for 1D nanomaterial growth.[17,47–49] The film thickness has been adjusted to tailor the average diameter and density of 1D nanostructures.[49–53] However, catalyst composition cannot be readily adjusted by these physical methods. In addition, deposition of nanometer thick films requires an ultrahigh vacuum system and carefully monitoring of deposition parameters proved to be costly. Furthermore, it is difficult to deposit a conformal layer uniformly on non-flat surfaces.

The solution-based synthesis is more cost effective compared to the vacuum based approach.[14,46,54–57] Catalyst coated substrates can be prepared by pyrolysis

of catalyst precursors such as salts or organometallic compounds.[14,46] Catalyst nanoparticles can also be synthesized in the form of colloids.[15] The solution-based approach offers greatly improved control in catalyst composition at low cost. Still, both catalyst film thickness as well as coating uniformity over a large surface area cannot be well controlled by the aforementioned solution approaches. Another method that has been extensively investigated is to use block copolymer micelles as nanoreactors to generate well-dispersed catalyst nanoparticles with uniform size and periodicity.[20,40,54–59] We previously reported that catalyst-containing micelles can be deposited not only uniformly but also conformally on uneven surfaces. Horizontally aligned and suspended CNTs with similar diameter have been generated.[60] Nevertheless, block copolymer templates are expensive.

Harnessing the ability of pyridine-based polymers to sequester metal species, we have employed poly(4-vinylpyridine) (P4VP) homopolymer as a low cost alternative to block copolymers to derive catalysis nanoparticles. We have demonstrated the capability of P4VP template to synthesize a catalyst-cocatalyst system with controlled size and composition. *This enabled the study of the role of catalyst composition in vapor-based 1D ZnO synthesis.* We have observed that catalyst composition can be used to adjust 1D ZnO morphology. The tendency of Zn vapor incorporation modulated by catalyst composition is a determining factor. Due to its unique properties and rich morphologies, ZnO has been employed as a model system to examine the role of catalyst in 1D nanomaterial synthesis.[2,10,61–70] Vapor-based synthesis of nanowires is widely accepted to follow the absorption, diffusion and precipitation method better known as the vapor-liquid-solid (VLS) method postulated by Wagner *et al.*[71] For ZnO nanowires, Zn vapor, produced by the carbothermal decomposition of ZnO powder by graphite,[24,41] is carried downstream to be adsorbed by the catalyst. After Zn saturation of the catalyst, Zn precipitates to form ZnO. ZnO deposition reaction equations are listed bellow:

$$2ZnO(s) + C(s) \rightarrow Zn(g) + CO_2(g)$$

$$ZnO(s) + C(s) \leftrightharpoons Zn(g) + CO(g)$$

$$ZnO(s) + CO(g) \rightarrow Zn(g) + CO_2(g)$$

$$ZnO(s) + (1-x)CO(g) \leftrightharpoons ZnO_x(g) + (1-x)CO_x(g)$$

$$2Zn(g) + O_2(g) \rightarrow 2ZnO(s)$$
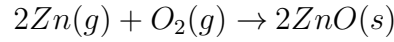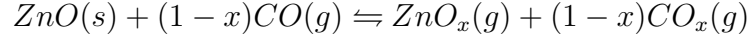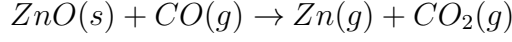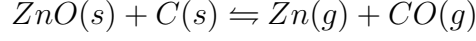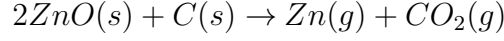
Furthermore, the conformal coating ability of polymeric materials, in which catalyst species are incorporated, together with the selective interaction with the Zn rich surfaces of as grown 1D ZnO nanostructures, allow even deposition of catalysts on a surface with topography. Therefore, 3D structures that are composed of high-density nanobrushes emanating from these intricate surfaces can be created. The ability of generating semiconducting 1D nanostructures arranged in 3D will enable a multitude of applications, such as photocatalysis, solar cells, and water splitting.

2.1 Experimental

Synthesis of ZnO Nanowires performed by the chemical vapor deposition method inside of a quartz tube furnace, from catalyst loaded SiO_2 wafers.

2.1.1 Catalyst Preparation

Employing the polymer template we can control the catalyst deposition uniformly over large substrates, as well as the stoichiometric composition of catalyst. Poly(4-Vinyl Pyridine) (P4VP) is purchased form polymer source and used without purification. Metal salts, used as received from Sigma-Aldrich, include: Tin(II) Acetylacetone, Zinc(II) Acetylacetone, Gallium(II) Acetylacetone, Iron(III) Acetylace-

tone, Yttrium(III) Acetylacetone, Aluminum(II) Acetylacetone. Silicon wafers with 100 nm oxide layer are purchased from University Wafers. Wafers are cleaned by pirahna method, a boiling mixture of H_2SO_4 and H_2O_2 (3:1) soaking for 30 mins and extensive rinsed in DI water.

Polymeric solution and casting

Catalyst coating solution is prepared by dissolving P4VP, and each metal salts separately in reagent grade butanol. Once fully dissolved, various stoichiometric amounts of the two metal salts are mixed together, polymer solution is later introduced drop-wise. The final polymer concentration is 0.275 wt.% and a metal-to-polymer ratio of 0.8, to ensure the complete complexation of metal with polymer. Polymer spin casting is as follows, Si wafers are removed from DI water and blow dried before loading into spin coater. Two layers of catalyst solution (0.5 ml) are spin casted at 3000 rpm for 90 seconds with 30 seconds soft bake at 140 ℃ after each layer to burn off excess solvent.

Pre-growth sample preparation

After catalysts loading, the samples are treated with UV-Ozone at 150 ℃ for 30 mins to gently remove polymer template leaving behind only the metal catalyst. After UV-Ozone treatment, the samples are annealed at 450 ℃ for 1 hour and naturally cooled down to room temperature. At this point samples are ready for ZnO growth.

2.1.2   ZnO Nanowire Growth

The growth of the ZnO nanowires takes place inside a quartz tube furnace. Three temperature controlled heating zones permits control over the source and sample temperature. The source is a powder mixture of Graphite and Zinc Oxide, each purchased from Alfa-Aesar.

A typical growth is as follows. A catalyst sample held by an alumina holder is placed inside the quartz tube. Then 0.8 g of source powders is loaded into an alumina boat and placed 18 cm away from sample, in a different heating zone. The furnace is heated while maintaining vacuum, with the source outside of the heating unit, until the start of growth. When the desired growth temperatures of source and sample are reach, the source is brought back into the heating unit and the camber is filled with a mixture of Ar (98%) and O_2 (2%) and maintained at 3 Torr during growth. After 20 mins of growth, all the heaters are turn off, the furnace is opened and the O_2 supply cut off. The furnace is then fan cooled to room temperature and their substrates extracted.

2.1.3 Characterization

After deposition of a polymer and organometallic solution mixture on Si substrates followed by solvent removal, Fourier transform infrared spectra (Nicolet 380 FT-IR) were collected to verify the formation of coordination bonds between metal species and N of pyridine rings. Atomic force microscopy (AFM, XE-70, Park System) was employed to characterize catalyst size in non-contact mode. X-ray photoelectron spectroscopy (XPS, PHI-5000C ESCA system from Perkin-Elmer) was used to study catalyst composition. Monochromatic Mg Kα with photon energy of 1253.6 eV was selected as the X-ray source. Scanning Electron Microscopy (SEM, FEI XL30) was used to examine ZnO morphology.

2.2 Results and Discussion

2.2.1 Nanocatalyst

The polymer template is successful at sequestering metal species. FTIR spectra of P4VP-Metal system coated on top of SiO_2 wafers reveals the complexation of monometallic Zn, Sn, and bimetallic Sn-Zn species, as observed in Figure 2.1.

The new band at 1620 cm^{-1} indicates that Zn(II)-pyridine and Sn (II)-pyridine complexes have been formed. Comparing the complexation tendency between Zn(II) and Sn(II) in the form of acetylacetone, the greater change of the band associated with pyridinic ring indicates that Zn has a stronger tendency to complex with pyridine group. This can be postulated on the basis that Zn(II) has partially unfilled d orbitals while Sn(II) has filled 3d orbitals. However, the 4th electron shell of Sn has been partially filled with 2 electrons and thus can act as a Lewis acid to form a complex with the pyridine ligand,[72] as supported by the FTIR spectrum of Sn(II) pyridine. As expected, the FTIR spectrum of P4VP/(Sn/Zn) shows the combination of both effects. This demonstrates the effectiveness of P4VP to sequester and deliver metal nanoparticles with tunable composition.
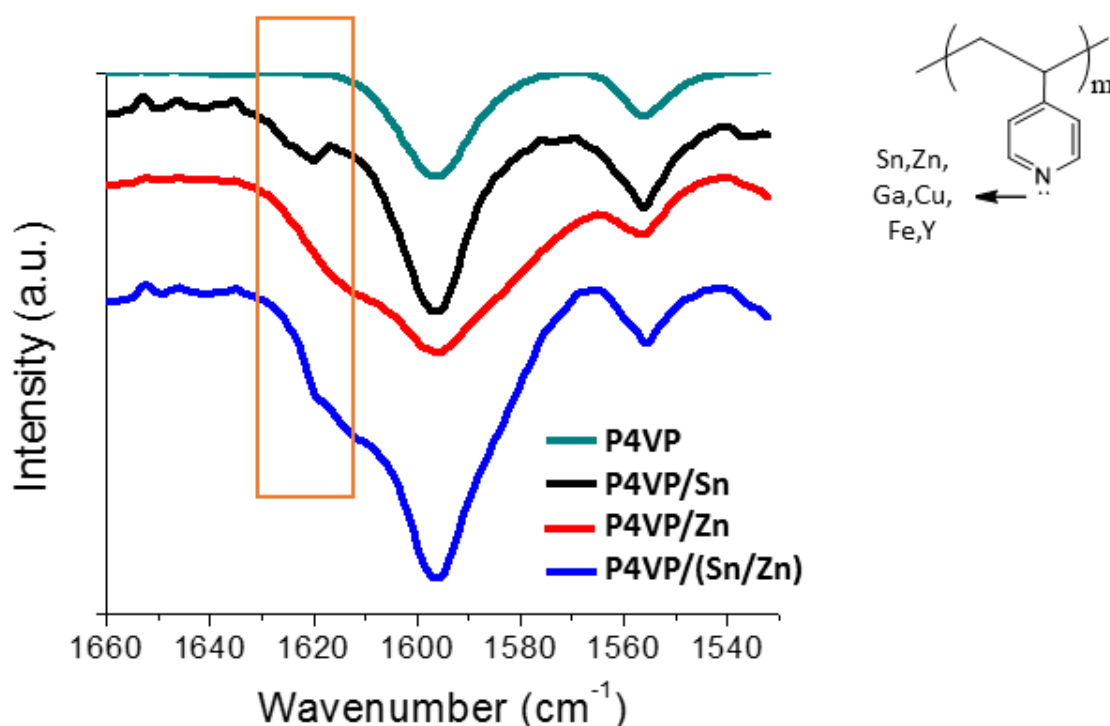
Figure 2.1: FTIR spectra of P4VP, P4VP/Sn, P4VP/Zn, P4VP/(Sn/Zn) respectively. Insert is P4VP chemical structure depicting the metal sequestration route.

Figure 2.2 contains a set of AFM images and corresponding XPS elemental analysis of nanoparticles prepared using selected solutions. The binding energy peaks located at 485.6, 933.6, 1022 and 1117.4 eV indicate the formation of SnO,

CuO, ZnO, and Ga_2O_3 respectively.[73] Together with AFM height images, it can be concluded that nanoscale particles, $(Zn/Sn)O_x$, $(Zn/Cu)O_x$, and $(Zn/Ga)O_x$ have been formed.

Using the polymer template approach to incorporate a variety of metal species, a catalyst-cocatalyst system in which ZnO is catalyst and metal oxides such as SnO, Ga_2O_3, CuO, Y_2O_3, and Fe_2O_3 are cocatalysts were prepared. The synergetic interactions of these catalyst-cocatalyst became the focus of the study. It has been reported that a catalyst-cocatalyst system offers synergistic or complementary effects to promote the controllable growth of 1D nanostructures, especially 1D carbon nanomaterials.[42,43,45,74–80]

Figure 2.3 is a set of XPS of $(Zn/Sn)O_x$ and $(Zn/Ga)O_x$ catalyst-cocatalyst systems with tuned atomic ratios. The arrow indicates the increase of Sn or Ga content. For $(Zn/Sn)O_x$ catalyst in Figure 2.3(a), the atomic ratio of Zn to Sn is 2.02, 0.68, and 0.26 respectively. In the case of $(Zn/Ga)O_x$ in Figure 2.3(b), the atomic ratio of Zn to Ga is 6.06, 3.11, and 0.82 respectively. Therefore atomic ratio of Zn to Sn and Zn to Ga can be rationally adjusted by metal precursor loading. The ratio differences can be explained by the metal-pyridine coordinations.[81] Zinc can readily form six coordinations with pyridine groups, Tin can coordinate with two pyridine groups, but gallium can only form one coordination. It is therefore expected that the XPS follows the metal-sequestration trend, Zn>Sn>Ga.
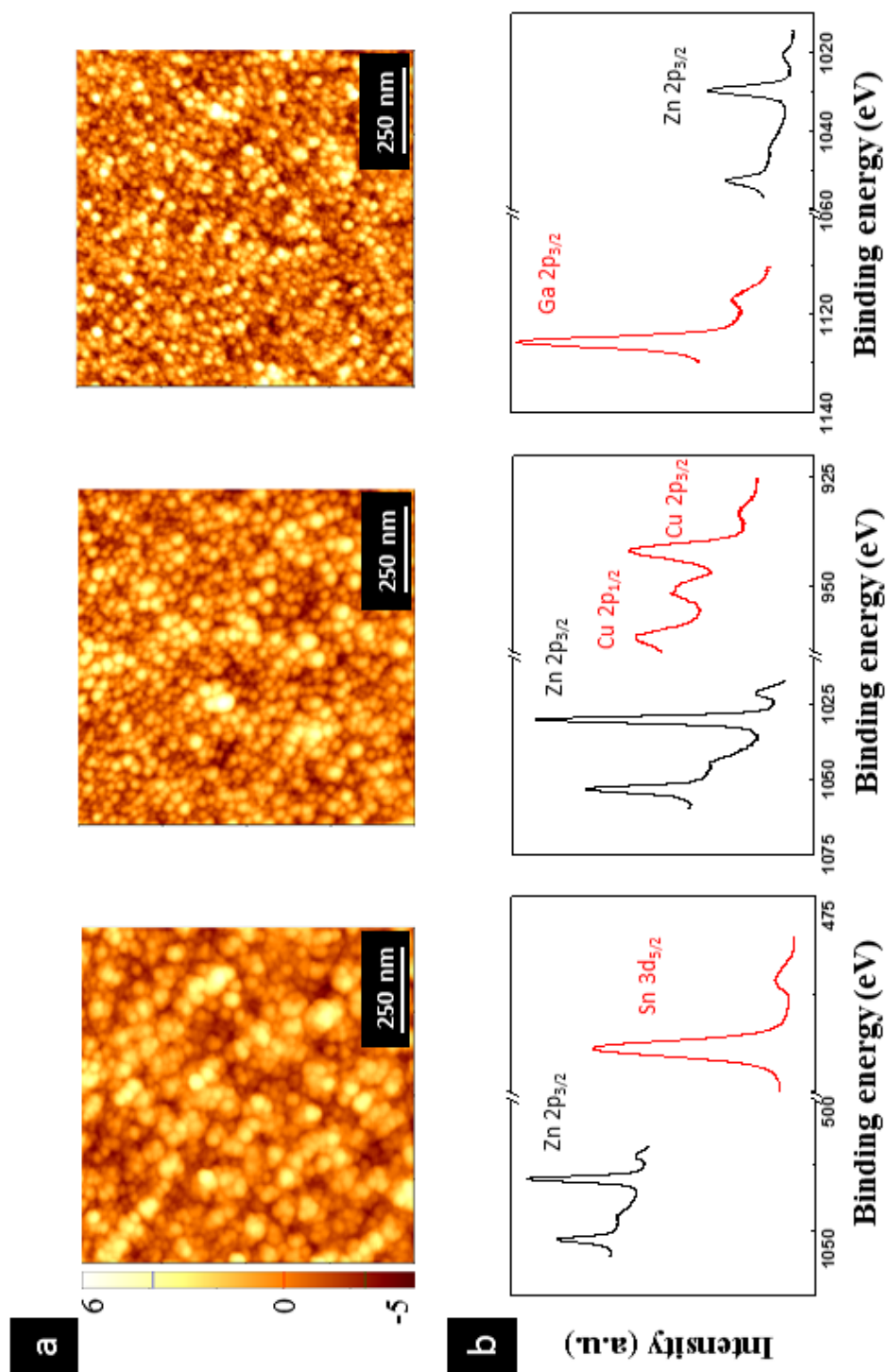
Figure 2.2: Catalyst nanoparticles derived from P4VP (M_w = 19,000 g/mol) template. (a) AFM height images of $(Zn/Sn)O_x$, $(Zn/Cu)O_x$, and $(Zn/Ga)O_x$ respectively (scan area: 1 x 1 μm, height scale: nm); (b) Corresponding XPS spectroscopy analysis.
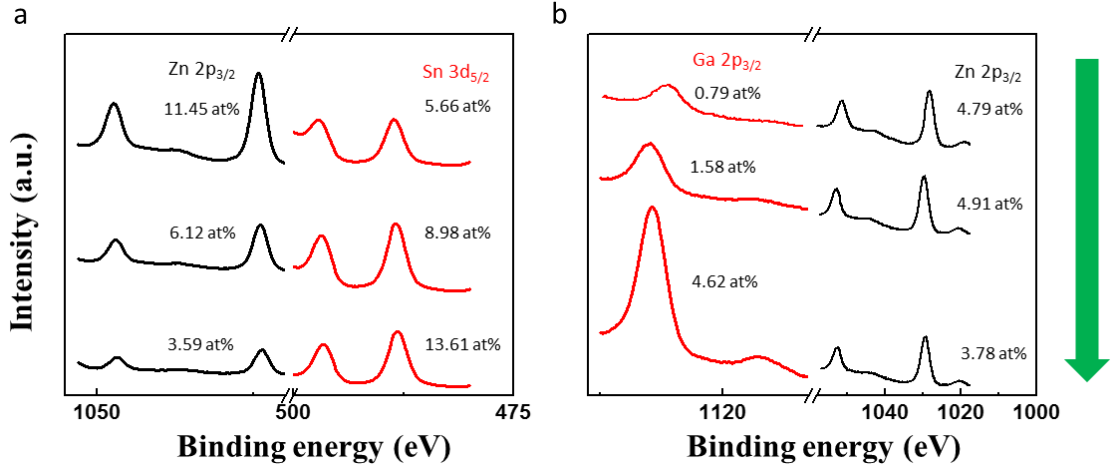
Figure 2.3: XPS of catalyst-cocatalysts with adjusted atomic ratios. (a)$(Zn/Sn)O_x$; (b)$(Zn/Ga)O_x$.

2.2.2 Effect of Catalyst Composition on ZnO Nanowire Growth

Using the polymer template approach to incorporate a variety of metal species, catalyst and catalyst-cocatalyst can be readily synthesized. The ZnO catalyst system doped with other metal oxides (SnO, Ga_2O_3, CuO, Y_2O_3, and Fe_2O_3) as cocatalyst have been prepared to investigate the role of catalyst composition on growth in both vapor-based and solution-based approaches. For the purpose of comparison, single metal oxide catalysts were used as references.

Figure 2.4 is a set of SEM images of 1D ZnO nanostructures grown using single metal oxides catalysts, and their corresponding catalyst-cocatalyst system, respectively. Ample experimental results indicate that catalyst composition play an important role in determining 1D nanostructure morphology.[14,44,82] Analogous to the effect of Ag,[44] Al_2O_3 and Ga_2O_3 promotes asymmetric growth and formation of nanobelts. In general, the use of metal oxide nanoparticles in the absence of ZnO, gives rise to random or less vertically aligned nanostructures as shown in Figure 2.4(a–d). The addition of ZnO into metal oxide catalysts results in more vertically oriented ZnO 1D nanostructures as shown in Figure 2.4(e–h).

These results further support the contention that ZnO can promote the epitaxial growth, corroborating the results of other groups.[14,44]

We further investigated the formation of 1D ZnO nanostructure using catalyst-cocatalyst systems where catalyst is ZnO and cocatalysts are metal oxides such as Fe_2O_3, Ga_2O_3, Y_2O_3 and CuO. Pure ZnO catalysts were not be able to grow 1D ZnO nanomaterials at 550 °C or lower temperature in our CVD system, as shown in Figure 2.6. However, all catalyst-cocatalyst systems tested so far allow the growth 1D ZnO nanomaterials at lower temperature, *i.e.* 525 °C, as demonstrated by the SEM images in Figure 2.5. Comparing growth results at different temperatures, 550 vs. 525 °C, higher growth temperature gives smaller-diameter nanostructures in general except for CuO. This result can be attributed to different melting temperatures of cocatalyst species and their ability to incorporate Zn vapor. Y_2O_3 has the highest melting temperature and it cannot be reduced by Zn vapor because of the low electronegativity of Y. Therefore, $(Zn/Y)O_x$ catalyst is most likely to promote a vapor-solid-solid (VSS) process, thus giving smaller diameter and less vertically aligned 1D nanostructures. In contrast, Fe_2O_3, CuO, and Ga_2O_3 can be reduced to metallic species due to their higher electronegativity. Therefore, the growth of 1D ZnO nanostructures is greatly affected by the melting temperature of Fe, Cu, and Ga. Compared to Fe and Cu, Ga possesses a very low melting temperature. Thus, partial evaporation of Ga might be responsible for the formation of small diameter nanostructures. The epitaxial relationship between ZnO and $(Zn/Ga)O_x$ also promotes the formation of vertically aligned 1D ZnO nanostructures.[83,84]

Both $(Zn/Fe)O_x$ and $(Zn/Cu)O_x$ produce large diameter rods at 525 °C. Nevertheless, at 550 °C, $(Zn/Fe)O_x$ produces smaller diameter nanorods whereas $(Zn/Cu)O_x$ induces the formation of larger diameter nanorods. Both Fe_2O_3 and CuO can be reduced by Zn vapor during the initial stage. Yet, due to the different melting temperature between Fe and Cu (1538 °C for Fe vs. 1085 °C for Cu), the
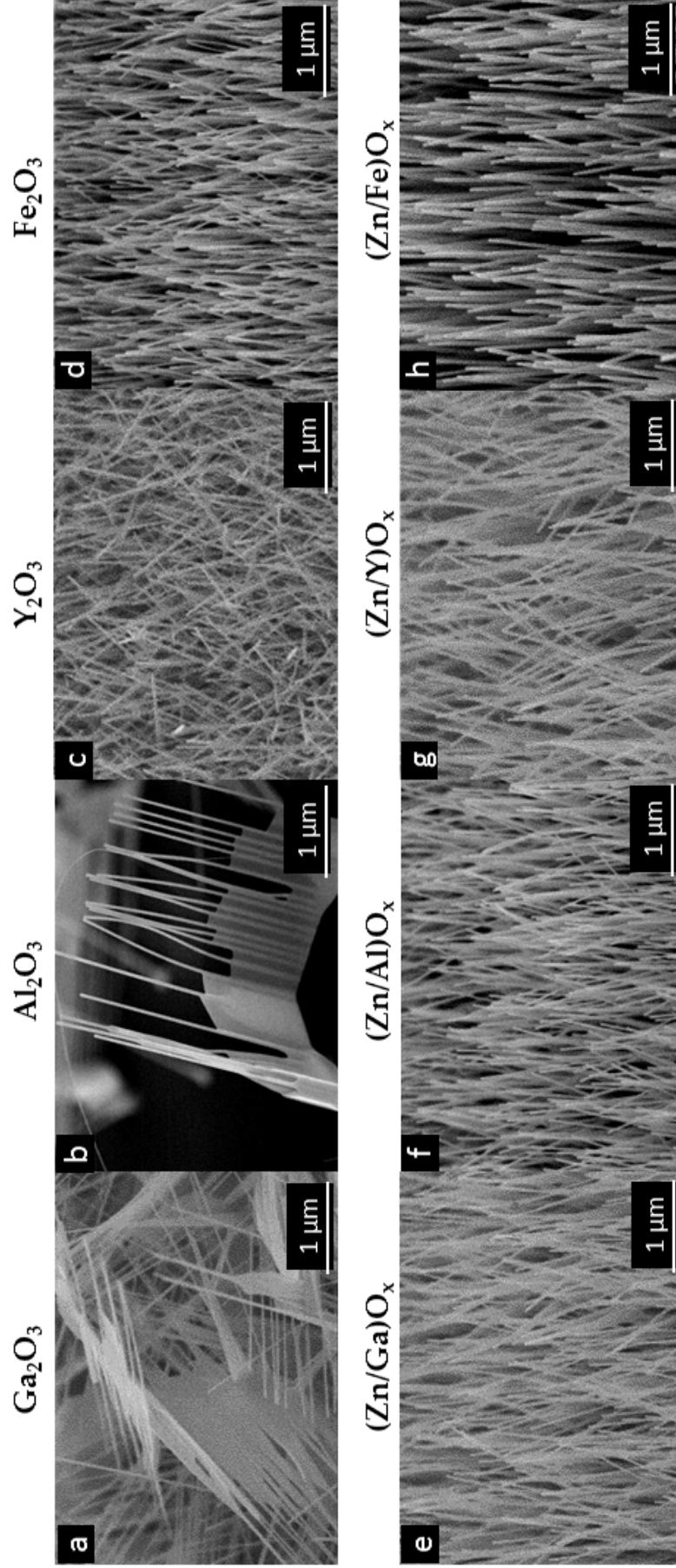
Figure 2.4: SEM images of 1D ZnO nanostructures grown using single metal oxide catalysts and cocatalysts of ZnO with other metal oxides. (a–d) are ZnO nanowires grown by Ga₂O₃, Al₂O₃, Y₂O₃, and Fe₂O₃ respectively; (e–h) are ZnO nanowires grown by those metal oxide catalysts with ZnO doping respectively.
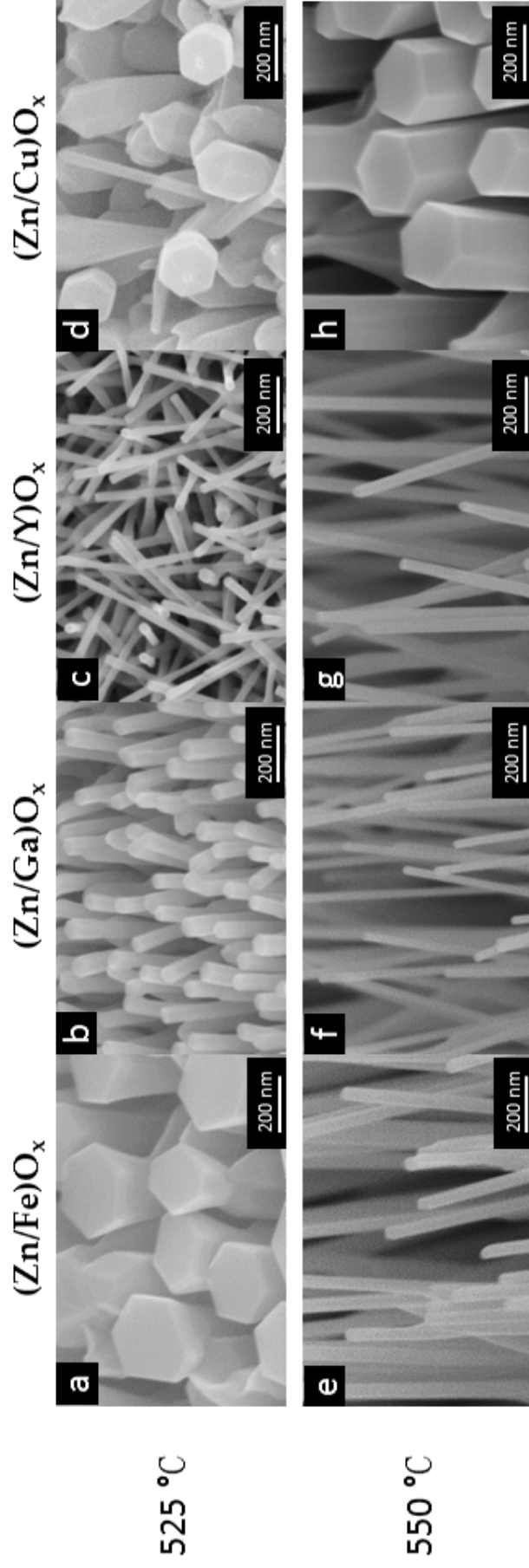
Figure 2.5: SEM images of ZnO nanowires grown by different cocatalysts. (a–d) are the nanowires grown by $(Zn/Fe)O_x$, $(Zn/Ga)O_x$, $(Zn/Y)O_x$, and $(Zn/Cu)O_x$ at 525 °C respectively; (e–h) are the nanowires grown at 550 °C using same catalysts respectively.

growth at 550 °C is most likely a VSS process for $(Zn/Fe)O_x$ and a vapor-liquid-solid (VLS) process for $(Zn/Cu)O_x$. In conclusion, the cocatalyst property can play an influential role in ZnO nanowire growth. These new findings provide a way to adjust 1D nanostructure morphology.

Figure 2.6 is a set of SEM images of 1D ZnO nanostructures using SnO, $(Zn/Sn)O_x$ and ZnO grown at various temperatures. The chemical composition of $(Zn/Sn)O_x$ has been analyzed by XPS in Figure 2.3(a) showing the control of catalyst-cocatalyst composition. Comparing the growth results using $(Zn/Sn)O_x$ and ZnO, adding Sn leads to the growth of longer 1D ZnO nanostructures at lower temperature. The possible mechanism is that Sn has higher electronegativity than Zn, so during the initial stage of the growth, it is expected that SnO can be reduced by Zn vapor. VLS would most likely take place due to the low melting temperature of Sn and the high solubility of Zn according to the phase diagram.[85] Therefore, the growth rate of 1D ZnO nanostructures will be enhanced. Indeed, the fact that the length of 1D ZnO nanostructures synthesized using $(Zn/Sn)O_x$ is greater than those using ZnO catalyst at 550 and 600 °C proves this contention. Catalyst-cocatalyst advantage can be observed by the growth at 525 °C where $(Zn/Sn)O_x$ promotes the growth of about 0.5 μm tall vertically aligned ZnO nanowires. SnO catalyzed ZnO nanowires show disordered orientation demonstrating the need of catalyst-cocatalyst system. No growth is observed using SnO at 600 °C, which is plausibly due to the loss of low-melting temperature Sn at higher growth temperature. This finding further supports that 1D nanomaterial morphology, length, diameter, and even the starting growth temperature, can be adjusted by tuning a catalyst-cocatalyst composition.

To compare the composition effect trends of vapor deposition, a hydrothermal growth was utilized using the same prepared catalysts. The hydrothermal growths were produced by my colleague, Yang Liu. Figure 2.3(b) shows the XPS data of $(Zn/Ga)O_x$ catalysts with tuned atomic ratios of Zn to Ga. The growth results

using those different $(Zn/Ga)O_x$ catalysts are shown in Figure 2.7. The result of increasing the amount of Ga is that the diameter of ZnO nanostructures increases in both vapor deposition and hydrothermal process, but the density of nanowires decreases significantly in the hydrothermal process. In the vapor-based process, pure ZnO seeds cannot generate 1D ZnO nanostructures at 525 °C. Adding Ga into the ZnO seeds promotes vapor-based growth as aforementioned. Furthermore, higher Ga content increases the ability to incorporate Zn vapor, enhancing VLS growth.

Recently our group has demonstrated that Ga_2O_3 nanoparticles are not stable in the hydrothermal synthesis.[86] During the hydrothermal synthesis, the higher the percentage of Ga is, the less stable the $(Zn/Ga)O_x$ system will be. Consequently, the resulting lower density of catalysts with predominately larger diameter caused by their instability in the growth media lead to sparsely populated microscopic sized 1D structures. Therefore, the length and diameter of 1D ZnO nanostructures can be adjusted in both vapor transport based and hydrothermal approaches using catalyst composition.

2.3 3D Growth Enabled by Polymer Template

Little mention was given to the incredible versatility of the homopolymer template method. In addition to the ability to adjust the catalyst composition, P4VP homopolymer can be employed to uniformly distribute catalyst payload onto topographic surfaces. The conformal coating ability of high molecular weight polymer enable the deposition of the catalyst-containing polymer thin layer on a sloped surface such as sidewalls of trenches. Owing to the selective interaction of pyridyl groups with Zn rich surface, a catalyst-containing polymer thin layer can also be formed on the surfaces of as-grown 1D nanostructures. The Zn(II) acetylacetonate-P4VP solution with a polymer M_w of 36,300 g/mol was used to deposit ZnO catalyst nanoparticles on sidewalls. Figure 2.8(a) is a representative
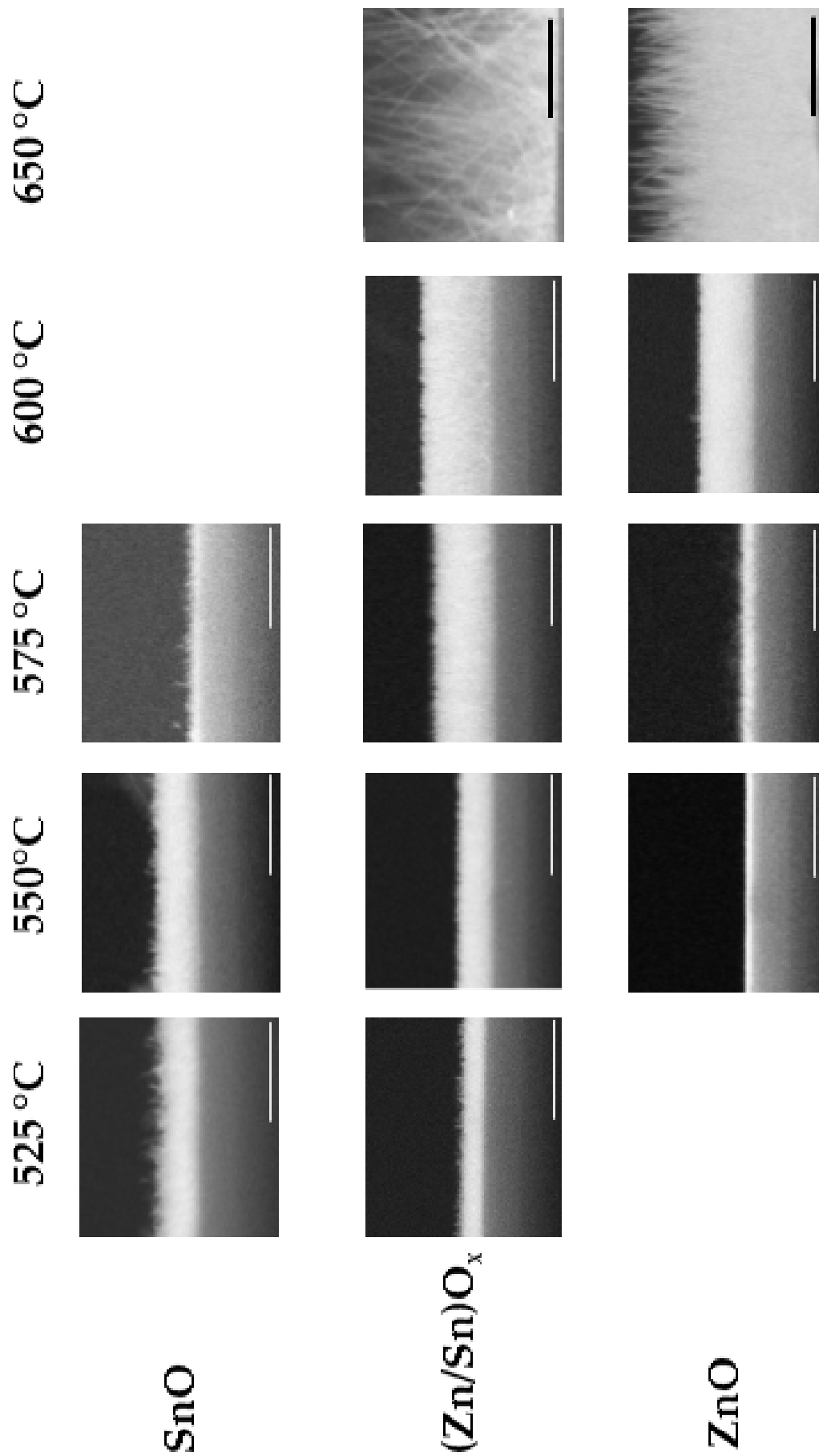
Figure 2.6: Cross-sectional SEM images of ZnO nanowires grown by SnO, $(Zn/Sn)O_x$ and ZnO at different temperatures. Scale bars are 2 μm for all the images.
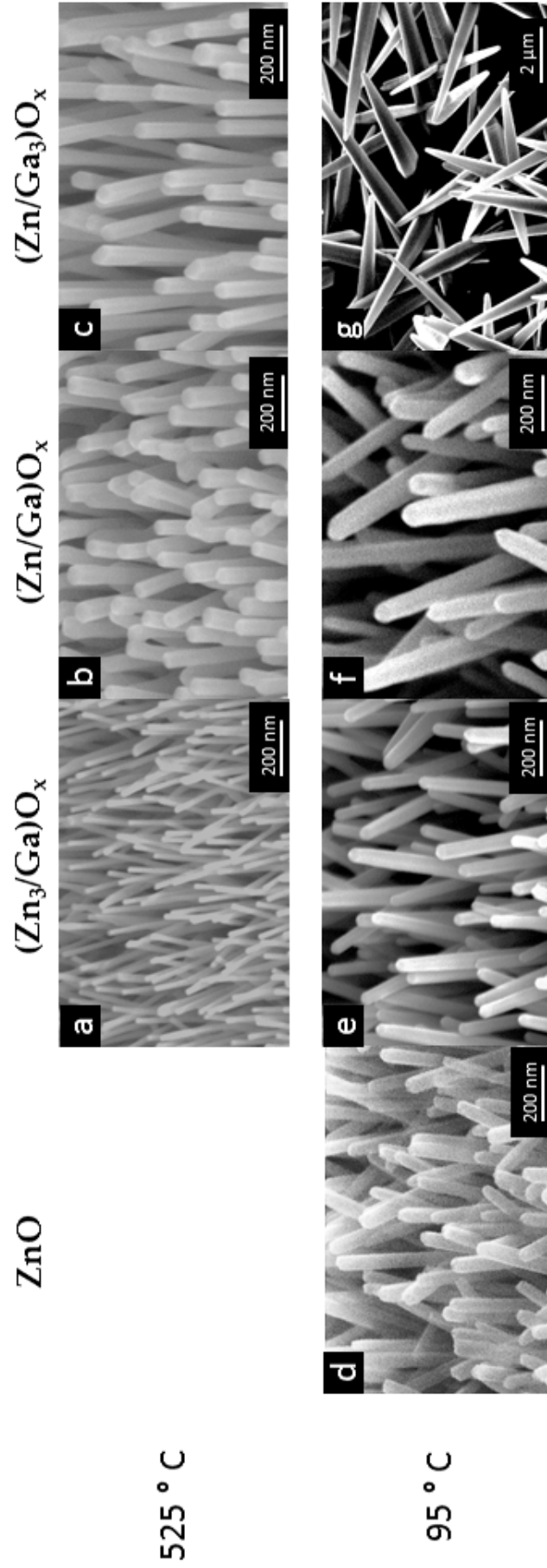
Figure 2.7: SEM images of ZnO nanowires grown by $(Zn/Ga)O_x$ cocatalysts with different Ga to Zn ratios. (a–c) are ZnO nanowires grown by vapor-based method at 525 °C with Ga to Zn ratio of 1:3, 1:1, 3:1 respectively. (d–g) are ZnO nanowires grown by hydrothermal method at 95 °C with Ga to Zn ratio of 1:3, 1:1, 3:1 respectively.

SEM image of ZnO nanowire growth result on a sidewall of a trench. Uniform and small nanowires that are aligned horizontally have been successfully synthesized.
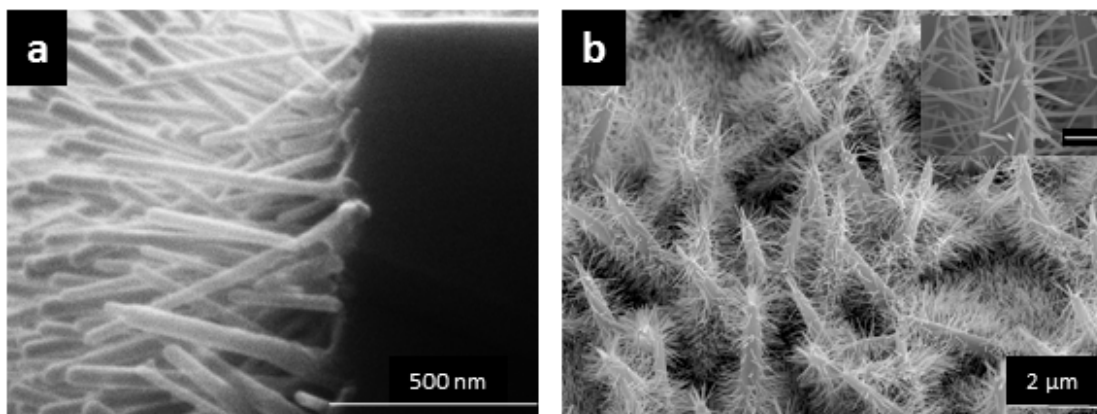
Figure 2.8: 3D growth using the polymer template approach. (a) horizontally aligned nanostructures on the side wall of a trench. (b) 3D branched growth. Scale bar in the inset is 200 nm.

The homopolymer template approach can also be used to fabricate highly branched 3D structures. After the growth of 1D ZnO nanostructures followed by deposition of catalyst species on surfaces of the as-grown ZnO nanostructures, a sequential growth was carried out using the vapor-based approach. Figure 2.8(b) contains the SEM image after the second growth showing that highly branched structures have been formed. This method to generate 3D nanostructures can afford uniform and well-defined 3D structures over a large surface area. Such a structure is highly desirable for energy related applications.

The 3D branched growth results were produced by my colleague, Yang Liu. They are here shown to assist with the essence of the chapter and the importance of the polymer template.

2.4   Future Work

The synergetic effects of bimetallic catalyst can be explored more in detail. Information regarding the role of each cocatalysts during the growth would be useful for designing advanced nano-devices, or improving the fabrication throughput.

Using a combination of surface elemental spectroscopy techniques (XPS or XAS) and high-resolution electron imaging techniques (SEM or TEM), it is possible to discover the interactions of each nanocatalysts in growth. Many of the here tested metal catalysts would benefit from a further systematic study of their compositions, as is the case of Al, which has the ability to produced nanoribbons at certain cocatalyst ratios. These studies can provide much needed insight at the catalytic process for the control synthesis of ZnO nanostructures.

Photoluminescence experiments can also be useful to discover the effects on the energy band gap, due to the use of bimetallic catalysts. This information is critical for nano-electronic devices, such as field-effect transistors. Lastly, it is worthwhile to explore the ability to implement both the polymer template method and the bimetallic catalysts approach for other technologically important semiconductor nanostructures.

2.5   Conclusion

Among all the catalyst formation and deposition techniques, vacuum-based thin film deposition is expensive and time consuming, and cannot coat catalyst uniformly on sidewalls readily due to shadowing effect. Stoichiometry control is also a challenge. Conventional solution-based deposition methods cannot effectively deposit nanocatalysts uniformly over a large surface area nor conformally on surfaces with significant topography. In contrast, this low-cost homopolymer template approach has demonstrated the formation of catalysts with not only engineered composition and size, but also uniform coating across a large surface area and on the sidewalls of trenches and on surfaces of nanostructures as well. Thus, this approach has enabled the systematic study of the role of catalyst composition on the vapor-based growth. We have revealed that the ratio of catalyst to cocatalyst will affect growth substantially. ZnO seed promotes vertically aligned nanostructures. The tendency of cocatalyst to incorporate Zn is critical. This finding can be a basis

for investigating using a catalysts-cocatalyst system in which catalyst is the same as the material for promoting epitaxial growth whereas cocatalyst will interact with 1D nanomaterial precursor for enhanced growth rate. Additionally, tailoring the catalyst-cocatalyst ratio enable us to define 1D ZnO morphology. Furthermore, we have exploited the conformal coating nature of P4VP homopolymer to deposit a catalyst thin layer on a sloped surface and on the surfaces of as-grown 1D nanostructures. Horizontally aligned 1D ZnO nanostructures and highly branched ZnO nanostructures can be synthesized reproducibly by this polymer template approach. It is expected that tuning catalyst composition to investigate 1D growth and forming 3D nanostructures, enabled by this polymer template approach, can be applicable to a broad field of 1D nanomaterial synthesis.

Chapter 3

Photoactivity Enhancement of ZnO Nanostructures

The harvesting of solar energy has been desired since before the discovery of photosynthesis. Semiconductors photocatalyst, including ZnO, allows the chemical storage of solar energy in H_2 by means of water splitting. The direct band gap properties of zinc oxide (3.2 eV) makes it suitable for visible-light water splitting applications. A major obstacle in water splitting and solar cells has been the visible-light absorption. Band gaps ideally between 1.1 to 1.7 eV are not easily attainable, and preventing the of the recombination of the electron-hole pairs produced after excitation is key to avoid the reduction of efficiency.[87–92] Recently carbon-metal-oxide heterostructures have shown to improve the performance of ZnO[37,92–96] and titanium oxide (TiO_2), a well known photocatalyst.[88,90,97] In this mechanism, carbon is proposed to act as current collector, effectively suppressing recombination events by shuttling the exciton electron away and allowing for surface reactions to take place. Other similar approaches have been studied with core-shell heterostructures.[90,96,98–101] For example, Zhong *et al.* demonstrated that applying a layer of GaN on top of ZnO nanowires can act as anti-photocorrosive and visible-light-sensitive surface for water splitting, at the same time, the band bending allows for holes to migrate towards the nanowire/water

interface for oxidation reactions to occur.[99] A more brute-force, yet highly effective mechanism to increase photoactivity is to maximize surface areas with 3D nanostructures.[88,102–106] This is only effective until shadowing effects of nearby nanostructures impede the use of available surface area, thus high-aspect-ratio nanowires are the preferred nanostructure.

Zinc Oxide nanostructures for photocatalysis have been synthesized and researched using wet chemical methods,[92,107,108] mainly hydrothermal synthesis.[2,14,86,94,96,109–115] The low temperature synthesis of hydrothermal growth permits the use of multiple substrates including metals and transparent conductive oxides[2,14,109] like indium tin oxide (ITO) to produce advance electronic and photonic devices, *i.e.*, solar cells.[108,115] The ease of production makes hydrothermal synthesis attractive to research groups that do not posses the more expensive and controllable vapor deposition equipment systems. Additional advantages of hydrothermal synthesis include scalability and morphology control of nanostructure through catalyst or reactants.[110]

Two main approaches to hydrothermal synthesis exist, based on the hydroxide (OH^-) source, hexamethylenetetramine[86,111] (HTMA) or ammonium hydroxide[109,110] (NH_4OH) based approaches. In the first one, a slow release of OH^--ions controls the reaction in a relative weak base environment from HTMA. This slow release is beneficial in controlling the kinetics to tune nanostructure growth. However, the absence of readily available OH^--ions slows the processing to excess of 6 hour. The prolonged dwell time can cause the re-dissolution of $Zn(OH)_2$ and hinder the growth. On the other hand, the NH_4OH approach produces a strong basic environment and provides abundant, instantaneous, and easily accessible OH^- ions. The result is a faster synthesis period of 2+ hours. For this approach however, use of inert or base resistant substrates and the careful tuning of precursors and synthesis time are necessary to ensure the desired final product. This limitation are in response to the accelerated kinetics caused by NH_4OH.

Typical chemical reaction to produce ZnO with NH$_4$OH are as follows[109]:

$$NH_4OH \rightleftharpoons NH_4^+ + OH^-$$

$$NH_4OH \rightleftharpoons NH_3\,(g) + H_2O$$

$$Zn^{2+} + 2OH^- \rightleftharpoons Zn(OH)_2\,(s)$$

$$Zn(OH)_2\,(s) + 4NH_4OH \rightleftharpoons Zn(NH_3)_4^{2+}\,(aq) + 4H_2O + 2OH^-$$

$$Zn(OH)_2\,(s) \rightleftharpoons ZnO\,(s) + H_2O$$
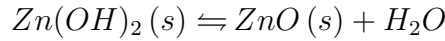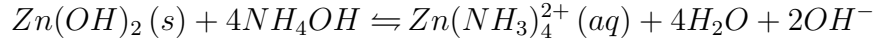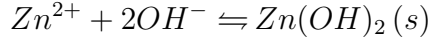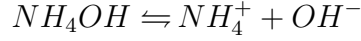
It is natural to expect that a combination of both mechanisms, high surface area and carbon coating, can lead to the synergistic increase in photoactivity. Thus, *I aim to understand the effects of carbon overcoat on ZnO photocatalysis.* In doing so, determining the role of carbon coating in promoting exciton dissociation,[93,116] facilitating electron transport,[92] or as dopant that leads to visible-light absorption for electron-hole generation.[97] In order to accomplish this goal a versatile, conductive, chemically and thermally resistant electrode is required and one from which ZnO nanostructures can be grown and modified — stainless steel (SS) foils satisfied these criteria. The approach developed here can potentially be modified for use by other semiconductors or substrates. The results demonstrate that 3D ZnO nanostructures have enhanced photocatalysis. Also, the carbon coating showed increased performance. This demonstrates that electropolymerization is an effective mechanism for surface modification of ZnO.

3.1 Experimental

3.1.1 ZnO Nanostructures on Stainless Steel

Synthesis of ZnO nanostructures is performed via hydrothermal synthesis. 316 stainless steel is used as substrates while zinc nitrate (Zn(NO$_3$)$_2$) and ammonium

hydroxide (NH_4OH) are the reactants purchased from Sigma-Aldrich and used as received. Stocks solutions of $Zn(NO_3)_2$ and NH_4OH in DI water are prepared and mixed in appropriate amounts 15 mins before the growth. In addition to the cleaning procedures detailed in **Appendix A**, SS strips are cleaned by UV-Ozone at 150 °C for 30 mins. Once cleaned, SS samples are bent and hanged from glass vials with the growth site facing down, subsequently the precursor solution is added. The vials are cover with a Septa cap and vacuumed (15 mins) to remove dissolved gases, using a house vacuum. Nanostructure growth takes place inside a 95 °C (pre-heated) vacuum oven for 3 hours. Once the growth is finished, samples are removed from the oven and rinsed sequentially in 80 °C, 40 °C, and room temperature DI water before drying and storing.

3.1.2   ZnO Carbon Overcoat and Sequential Growth

Procedures to overcoat and grow sequentially are shown in Figure 3.1. Carbon overcoat is achieved through the electropolymerization of acrylamide (AM) onto ZnO nanostructures and the subsequent pyrolysis. Just prior to polymerization, hydrothermally grown ZnO samples are cleaned by UV-Ozone at 150 °C for 20 mins. To polymerize, a solution consisting of acrylamide monomer, methylene-*bis*-acrylamide (MBA) cross-linker, and either zinc chloride ($ZnCl_2$) or nickel nitrate ($Ni(NO_3)_2$) as catalyst and electrolyte is prepared. Electropolymerization takes place in a 3-electrode cell by cycling between -0.2 and -1.8 V (Ag/AgCl) at a scan rate of 150 mV/s for 15 cycles, under constant N_2 purging using a BioLogic SP-200 potentiostat. The electrochemical cell is comprised of ZnO nanostructures on stainless steel as the working electrode, a graphite rod as the counter electrode and Ag/AgCl in saturated KCl as the reference electrode. After polymerization, samples are rinsed in DI water and dried overnight in a desiccator before being pyrolyzed in a temperature controlled furnace at 650 °C for 3 hrs with an argon atmosphere. The acrylamide was purchased form Bio-Rad and purified by

recrystallization in acetone. All other reagents were used as received from Sigma-Aldrich.

In order to form 3D nanostructures on ZnO nanowires, the carbon overcoat is removed by UV-Ozone at 150 °C for 20 mins and then annealing in air at 400 °C for 1 hr. With the carbon removed, sequential ZnO CVD growth takes place for 15 mins following the growth process detailed in the previous chapter.
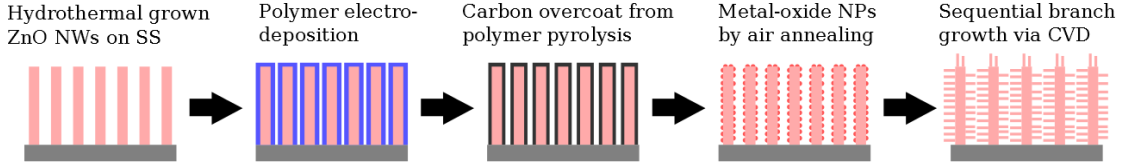
Figure 3.1: ZnO carbon overcoat and 3D growth process representation.

3.1.3 Characterization

ZnO morphology was examined with a FEI XL30 scanning electron microscope at the Imaging and Microscopy Facility (IMF) in UC Merced. Photocatalytic activity was evaluated at different stages of the ZnO processing by measuring the degradation of methylene blue (MB) dye (Tokyo Chemical Industry) to UV light. MB solutions were allowed to stabilize in the dark for 15 mins before using. ZnO nanostructures on stainless steel (1 cm^2) are submerged in 2 ml of 8 mg/L MB solution and exposed to UV light radiation from a mask aligner (Quintel, Q-2001CT) for different lengths of time. UV-Vis spectroscopy (Agilent, 8453 UV-Vis) was used to record MB absorbance peaks after each UV light exposure. To further explore the photoactivity of nanostructures, photoelectrochemical (PEC) measurements were carried in a 3-electrode system with 0.1 M Na_2SO_4 electrolyte using a potentiostat (CH Instruments, Model 600). ZnO nanostructures on stainless steel (1 cm^2) acted as the working electrode, a platinum coil served as the counter electrode, and a Ag/AgCl in saturated KCl was used as the reference electrode, each electrode is separated by a glass frit. The voltage was swept from -0.1 and 1.0 V (Ag/AgCl) at a scan rate of 5 mV/s. Light and dark measurements

were recorded by turning a AM1.5 lamp (100 mW/cm^2) on and off. The dark measurements were subtracted from the light measurements to yield the resultant current gain.

3.2 Results and Discussion

3.2.1 Controlled ZnO Growth on Stainless Steel

Hydrothermal synthesis of ZnO nanostructures on stainless steel was successful by utilizing NH$_4$OH as a source of OH$^-$. The chemical resistant nature of stainless steel allows us to utilize a strong basic (pH >9) environment at elevated temperatures without detrimental effects on stainless steel. To contrast, experiments conducted using copper foil as substrate demonstrated successful growth of ZnO nanostructures but significant copper was lost due to etching. Copper slowly dissolved into the solution, the release of Cu^{2+}-ions was indicated by the blue tinting of the solution. In the 3 hours of growth, multiple pits developed on copper foil, reducing the mechanical stability of the substrate.

Morphology control of the nanostructures is required to optimize the photocatalytic performance. Researchers have exerted control on ZnO nanostructures by hydrothermal synthesis control of the precursors, temperature, concentrations of Zn^{2+} or OH$^-$, growth time, and chemical capping agents.[108–110,117] In our synthesis it was found that the molar ratio of NH$_4$OH to Zn(NO$_3$)$_2$ (NH$_4$/Zn) was critical to the morphology control.

Figure 3.2 are SEM images of different NH$_4$/Zn ratios while maintaining a 15 mM Zn^{2+} concentration. Smaller ratio numbers show more spatial density with short and smaller diameter nanostructures. The low amount of NH$_4^+$ ions in the solution causes the reaction to slow down due to low available OH$^-$-ions. Low NH$_4^+$ also prevents the etching of Zn(OH)$_2$ into Zn(NH$_3$)$_4^{2+}$, which as result increased the density by increasing the nucleation and growth of multiple nanostructures. Bigger

ratio numbers show less density with bigger and larger diameter nanostructures. Opposite to the low NH_4^+ case, high NH_4^+ results in larger nanostructures because the excess of OH^--ions precipitates more ZnO. The low nanostructure density can be attributed to the large diameter of nanostructures and the etching effect of higher NH_4^+. The high concentrations of NH_4^+ dissolves $Zn(OH)_2$ into $Zn(NH_3)_4^{2+}$, especially from smaller nanostructures with greater aspect ratios.
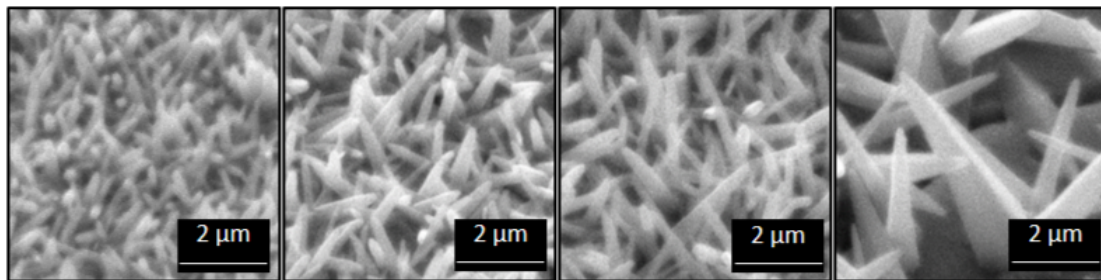
Figure 3.2: Hydrothermal density and morphology control of ZnO by varying the NH_4/Zn ratio. Ratios shown are 23.5, 25, 27, and 30 respectively.

In parallel with the study of NH_4/Zn, we investigated the effects of Zn^{2+} concentration on morphology of nanostructures. It is known that as the concentration of the zinc source increases, the length and diameter of the ZnO nanorods also increases.[118] Figure 3.3 is a set of SEM images depicting different Zn^{2+} concentrations while maintaining a 23.5 NH_4/Zn ratio. It can be seen that low concentrations of Zn^{2+} have very small and sporadic growth of nanostructures that are susceptible to the etching effects of NH_4^+. Higher concentrations of Zn^{2+} show more defined and larger nanostructures which agrees with the results of other groups.[118] We proposed that at higher concentrations of Zn^{2+}, even with NH_4^+ reacting with $Zn(OH)_2$, the large amount of $Zn(OH)_2$ produced can still transform into ZnO.

To summarize, the morphology of ZnO nanostructures can be adjusted in hydrothermal synthesis by means of precursor tuning. The direct growth of ZnO nanostructures on stainless steel substrates makes it ideal for electrochemical processing and testing as well as for high temperature processing. Therefore, this

ZnO electrode can act as a template for energy related applications, especially photoelectrochemical.
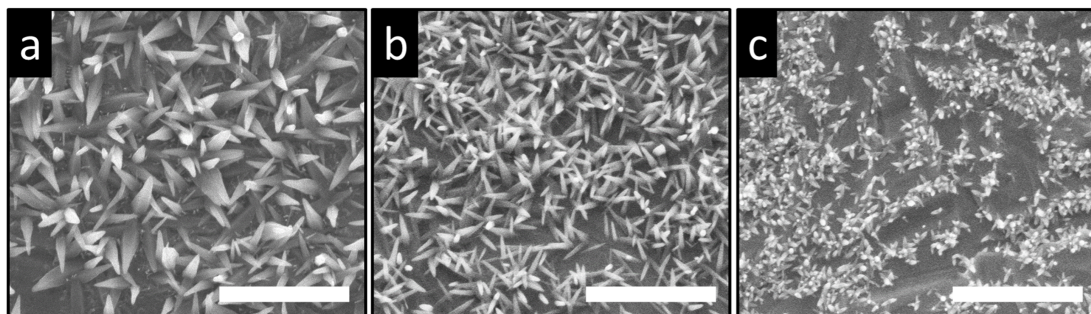
Figure 3.3: Size control of nanostructures by the Zn content. Concentrations are 20, 15, and 10 mM respectively. Scale bars are 10 μm.

3.2.2 Surface Functionalization – Carbon Coat and 3D Nanostructures

To create a carbon overcoat on ZnO requires a polymer layer as the source of carbon. Therefore, I tested the ability to produce polymeric films with different metal catalysts (see **Appendix B**) and discovered that $ZnCl_2$ and $Ni(NO_3)_2$ are successful catalysts to promote polymer films by an electrochemical approach. Figure 3.4(a) is a representative image of a polymer-coated ZnO nanostructures. By pyrolyzing the polymer-coated ZnO NWs in an intern atmosphere, a layer of carbon can be produced on ZnO NW, hereafter called carbon-coated ZnO (C-ZnO). This heterostructure is utilized to study the photoactivity of ZnO vs. C-ZnO.

After the pyrolysis of the polymer layer it was evident that the metals used for polymer electrodeposition will remain complexed with the polymer and could become metal-oxide nanoparticles (NPs) when annealed in air, similarly to the homopolymer template in the previous chapter (Section: **2.2.1**). Since metal nanoparticles are present in the sidewalls of ZnO nanostructures, I performed sequential branch growth of ZnO via chemical vapor deposition. Figure 3.4(b–c) are the resultant 3D nanostructures produced by the sequential growth from ei-

ther Zn or Ni catalyst. Zn catalyzed nanostructure growth is well known and was explained in the previous chapter (Section: **2.2.2**). The zinc growth demonstrates thin ZnO NWs emanating from a nanoparticles base that is attached to the original ZnO NW. Nickel grown branches display short, cylindrical-rod morphology. Interestingly, smaller nanoparticles are attached to the original ZnO NW when Ni is used. It is proposed that the oxidation state of the Ni, during electrodeposition, affects its polymer complexation tendencies and play a role in the formation of smaller nanoparticles. Ni catalyzed (and Co-catalyzed) experiments were also conducted in the previous chapter study with poor growth results and it was therefore stopped and the results not shown. Those experiments followed a similar trend of short cylindrical-rods on SiO_2. However, ZnO nanostructure grown from Ni catalysts has been demonstrated by another group with more well define structures.[119]

My results are a proof-of-concept that 3D nanostructures can be formed on preexisting ZnO nanostructures. While no changes to the original ZnO CVD growth process were made, with the exception of a shorter growth time of 15 mins. As mentioned before, 3D nanostructures are highly desirable in renewable energy applications because of their high surface area, and I provide an approach to form this architecture.

3.2.3   Photoactivity Enhancement

Photonic devices have attracted strong interest due to their ability to transduce accessible and abundant solar energy. Water splitting can become one of the most efficient ways to harvest solar energy, since water is a renewable resource and the product of combusting H_2 and O_2. Three requirements exist for efficiently converting and storing solar energy: (1) Photocatalyst efficiently absorb sunlight to produce exciton pairs, (2) the exciton pairs are effectively separated to avoid recombination, and (3) the exciton must be energetically and kinetically capable
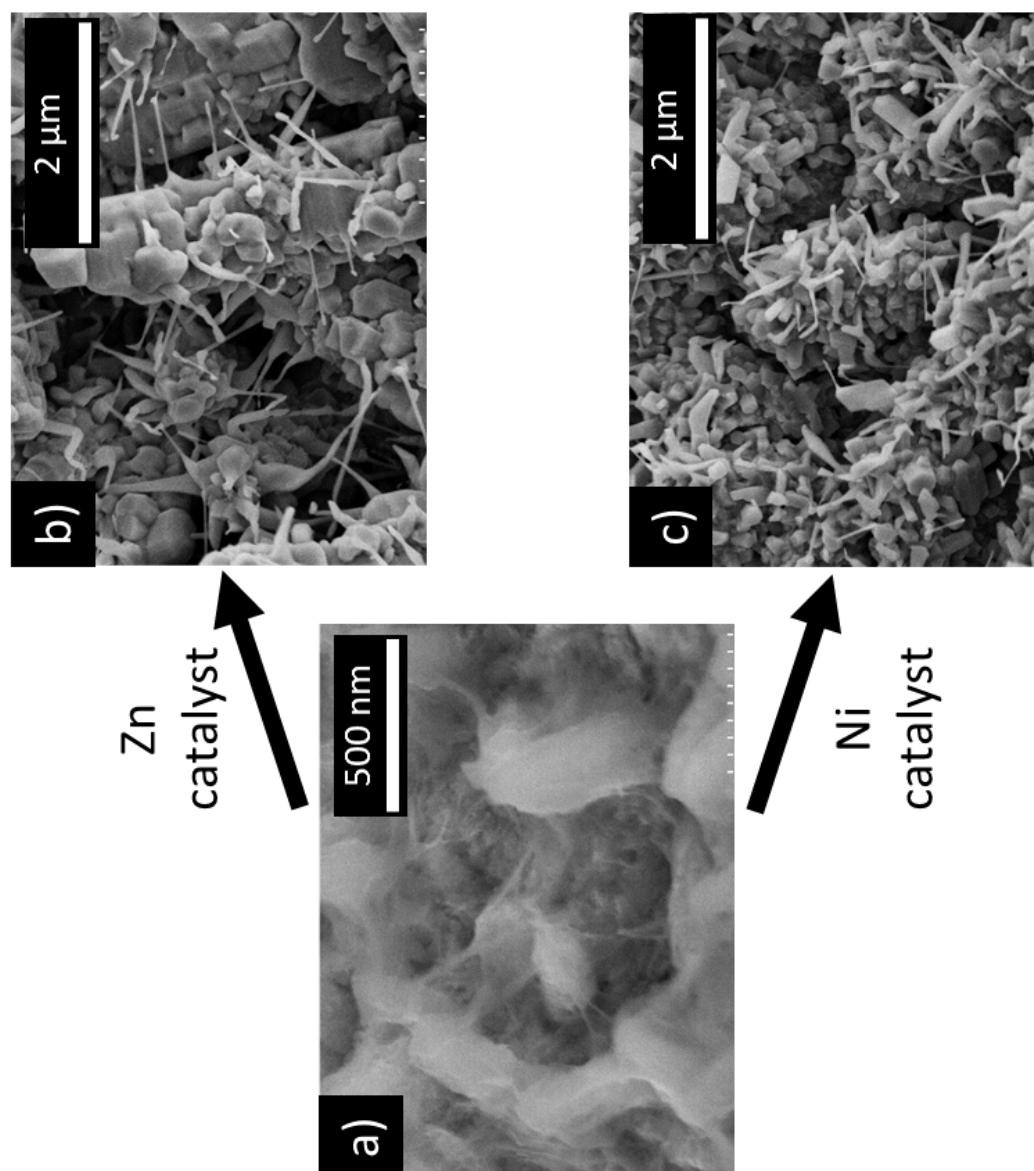
Figure 3.4: 3D nanostructure control through polymer coating and catalysts. Polymer coated ZnO nanostructures (a) and resulting 3D nanostructures by sequential growth when using Zn (b) or Ni (c) catalyst during electropolymerization.

of producing work, *i.e.*, water splitting.[91] Some of the current approaches to meet this criteria include coating photocatalyst with water-splitting co-catalysts or photocorrosion inhibiting layers, the development of new semiconductor materials that combine suitable photoelectrochemical properties (visible band gap, high carrier mobilities, *etc*), and the use of nanotechnology to exploit existing semiconductor photocatalysts.[88]

The photocatalytic activity baseline of synthesized ZnO nanostructures was first characterized by measuring the absorbance peak decrease of MB solution at 665 nm vs. time of UV light exposure. Minimal degradation is observed by exposing MB solution (without ZnO nanostructures) to UV radiation and this is used as a starting reference. When ZnO photocatalyst is introduced, the photocatalytic process is accelerated and dominated by the following reactions[120]:

$$ZnO + h\nu \rightarrow ZnO(e_{CB}^- + h_{VB}^+)$$

$$h_{VB}^+ + OH^- \rightarrow {}^\bullet OH$$

$$h_{VB}^+ + H_2O \rightarrow {}^\bullet OH + H^+$$

$${}^\bullet OH + \text{MB} \rightarrow \text{degradation of MB}$$
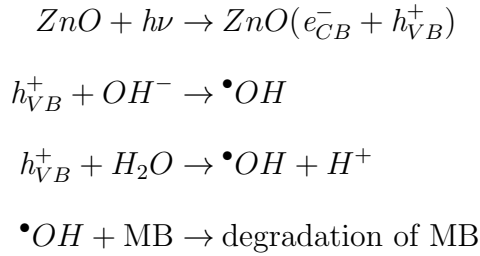
The photoactivity of ZnO is improved by carbon overcoat. The proposed band gap alignment is shown in Figure 3.5(b). Carbon coated ZnO (C-ZnO) shows faster degradation of MB (Figure 3.5(a)) than ZnO alone. This can be attributed to the enhanced photoactivity possibly caused by the more efficient separation of the electron-holes produced. It is also known that carbon can have synergetic effects on semiconductors for increased photoactivity and dye degradation. For instance, carbon can increase the visible-light absorption of ZnO beyond 400 nm.[37,93,113] Carbon overcoat can also increase the efficiency of photodegradation by adsorbing MB molecules via π-π conjugation, which allows the generated holes to easily access and oxidize MB molecules.[94,95]

Additionally, the carbon coating processing method was found to facilitate the synthesis of 3D nanostructures. The resulting 3D nanostructures have shown enhanced photoactivity due to their large and accessible surface area. My results in Figure 3.5(a) agree with this contention. The combination of carbon coating and 3D nanostructures are topics of interest for the visible light improvement of photoactivity. The enhanced MB degradation motivated me to attempt visible-light experiments through PEC experiments.
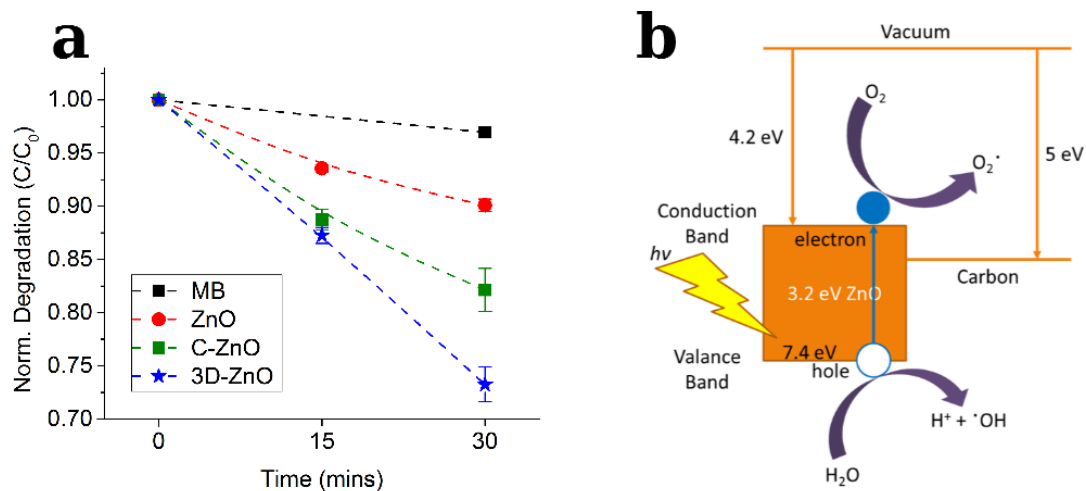
Figure 3.5: (a) Comparison of different MB degradation at select stages of ZnO processing by UV exposure. "As-grown" ZnO nanowires (● red), carbon coated ZnO nanowires (■ green), and 3D ZnO nanostructures (⋆ blue). MB used as starting baseline for comparison (■ black). (b) Schematic representation of carbon overcoat to enhanced photoactivity.

A significant advantage of ZnO on stainless steel substrates, in addition to its 1D geometry, is the excellent electron coupling with substrate due to the direct growth.[121] This gives the electrode the versatility to be electrochemically modified and tested. We tested the ability of ZnO and nanoparticle decorated ZnO nanostructures on SS to split water as seen in Figure 3.6. PEC measurements in Na_2SO_4 shows significant increase in photocurrent gain from the nanoparticle decorated ZnO nanostructures when compared to the ZnO nanostructures or to the stainless steel only. Stainless steel PEC was used as negative control. Similar to the photodegradation reactions, water splitting undergoes the following reac-

tions$^{(122)}$:

Base:

$$4H_2O + 4e^-_{CB} \leftrightharpoons 2H_2 + 4OH^- \qquad E^0_{red} = -0.828 \text{ V vs. NHE}$$

$$4OH^- + 4h^+_{VB} \leftrightharpoons 2H_2O + O_2 \qquad E^0_{ox} = -0.401 \text{ V vs. NHE}$$

Acid:

$$4H^+ + 4e^-_{CB} \leftrightharpoons 2H_2 \qquad E^0_{red} = +0.000 \text{ V vs. NHE}$$

$$4H_2O + 4h^+_{VB} \leftrightharpoons 4H^+ + O_2 \qquad E^0_{ox} = -1.229 \text{ V vs. NHE}$$
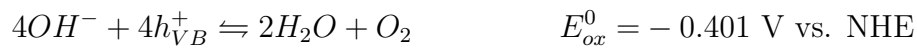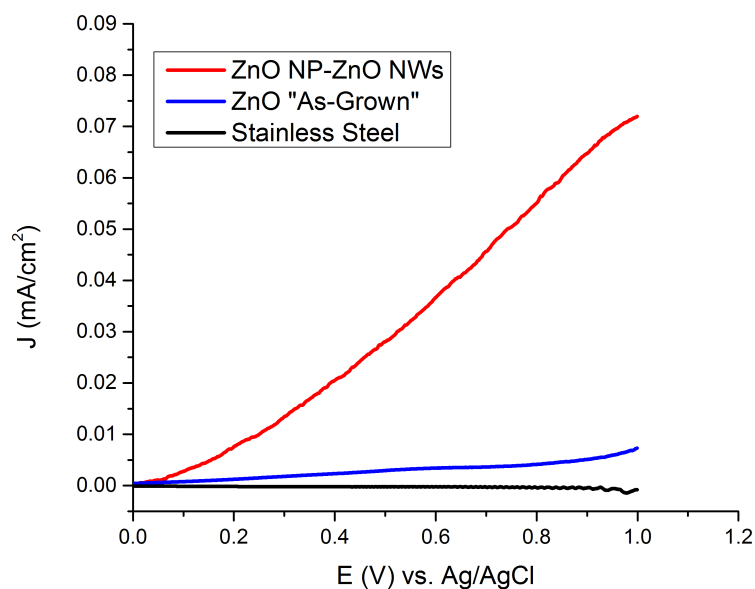
Figure 3.6: Photocurrent potential vs. voltage scans for stainless steel (**black**), "As-Grown" ZnO nanostructures on stainless steel (**blue**), and nanoparticles decorated ZnO on stainless steel (**red**). Scan rate 5 mV/s in 0.1 M Na$_2$SO$_4$ with a AM 1.5 light source. **Note:** Dark scans are subtracted from light scans.

3.3   Future Work

Thus far, exploratory experiments have been conducted to increase photoactivity of ZnO nanostructures on stainless steel. More characterization regarding the optoelectronic properties of carbon coated ZnO nanostructures and 3D ZnO nanostructures is required to truly understand the observed phenomena. Photoluminescence (static and dynamic) in conjunction with x-ray photoelectron spectroscopy tests are required to better understand the source of photo-enhancement. The former technique will elucidate the spectrum of usable visible light as well as give quantitative data on the kinetics of the carrier lifetime (electron-hole recombination time). The latter technique will give elemental composition data to more accurately tune the processing to the composition and the photoactivity observed.

Due to the low aqueous stability of ZnO, carbon coating can increase the chemical resistance which is of great importance for real life applications. Additional, the maximum 3D branching should be investigated, carbon coating then NW growth and repeat. As mention before, increasing 3D surface area is the most effective mechanism for enhancing photocatalysis.

The delivery effectiveness of electrodeposited polymer coatings can be further exploited. Distinct types of coatings are possible, for example: gallium nanoparticles can be delivered using Ga-salts mixed with 4VP (or other nitrogen containing polymer), after coating and polymer removal, GaN particles should be formed. This becomes beneficial when exploring distinct band gap alignments, without the need of exhausting vapor or physical deposition approaches.

3.4   Conclusion

In conclusion, I developed approaches that respond to the challenges to improve photocatalytic activity of ZnO for water splitting. Doing so by implementing a 3-pronged approach, nanostructures, carbon heterostructures, and high surface

area 3D structures; which are recognized as effective ways to enhance photoactivity. Highly photoactive 3D nanostructures were synthesized by the sequential growth from nanoparticles on the surface of pre-synthesized nanostructures. Carbon coated ZnO nanostructures with enhanced photocatalytic activity were also synthesized from the pyrolysis of polymer coatings. 3D nanostructures and carbon coating were made possible by the ability to electrodeposit polymer. The key to the success was to synthesize tunable ZnO nanostructures on stainless steel substrates, which enabled electropolymerization of polyacrylamide onto the surface of ZnO nanostructures.

The materials used, the hydrothermal approach, and electrochemical processing made this method scalable. Future research can utilize the procedures developed in this work with other semiconducting nanostructures. Using the information discovered, we can expect that heterostructured photocatalysts can soon bring forth a future of efficient and effective harvesting of solar energy to satisfy our energy demands.

Part II

Carbon Nanofiber Electrode:

Platform and Applications

Chapter 4

Supercapacitor Carbon Nanofibers

Three dimensional hierarchical nanocarbon electrodes, with great electrical properties, good chemical stability, and ease of synthesis are attractive for the implementation in energy storage and conversion applications.[123–125] These technologies are necessary for the replacement of fossil fuels as our primary sources of energy.[126–128] Common nanocarbon supercapacitor fabrication methods include the post-growth assembly of pre-synthesized carbons[123,125,129–132] and the direct growth of carbon nanostructures.[133–137] The former, generally, utilizes binder materials for structural integrity resulting in detrimental performance such as: poor contact resistance, added dead-weight, non-reproducible morphology, blocking of the active area by binder, and random electron transport due to the indirect contact of some carbons with current collector, to name a few of the drawbacks.[131,134,135,137] Free standing carbon electrodes (fibers, nanotubes, and powders) without binder have also been studied. These improved system still require a metal current collector and suffer from contact resistance problems since most of the individual carbons are not in contact with the collector, unless a large pressure is applied.[125,138,139] Direct growth on the other hand has the advantages of being binder free, with reproducible morphology, and providing direct electron pathway

to current collector. They are hindered only by the selection of the substrate, in terms of thermal and chemical stability during the synthesis and testing.

Recent 3D nanocarbon electrodes that utilize KOH, chemical activation, hard, or soft templates as means to induce a hierarchical porosity, have demonstrated the importance of interconnected hierarchical pores to improve ion transport, increase available surface area for double layer capacitance, and provide continuous and direct electron pathway which minimizes charge loss.[34,35,129,140–142] Therefore, *I present the study of a one-step approach to produce upright 3D hierarchical carbon nanofiber (CNF) electrode, directly grown on stainless steel.* This ready-to-use engineered electrode can be used as a platform for studying nanocarbon heteroatom doping, metal-oxide loading, and a multitude of energy storage/conversion related applications. These carbon nanofibers have the benefit of being robust, having a consistent morphology, and possessing large channels between bundles and small CNF pores to facilitate mass transport and ion diffusion.

4.1 Experimental

4.1.1 Sample Preparation

Synthesis of CNFs was conducted via chemical vapor deposition using NiCu catalyst on stainless steel (SS) substrates. The detail procedures to clean SS are detailed in **Appendix A**. These steps follow SS cleaning:

1) Clean SS strips are chemically etched using either hydrochloric acid or sulfuric acid. For HCl acid, samples are submerged in 37 wt.% HCl acid for 45 mins. When using H_2SO_4, SS strips are etched for 90 sec in a solution of 50 vol.% DI and 50 vol.% H_2SO_4, maintained at 95 °C with a water bath. After etching samples are rinsed for 30 seconds in DI water and subsequently connected to the potentiostat for plating catalyst.

2) Nickel-Copper (NiCu) electroplating is performed by a two step constant

potentiometry recipe. The first step applies a Cu film at -0.1 V (Ag/AgCl), while the second step plates mostly Ni at -0.7 V (Ag/AgCl). The overall thickness of electroplated film is approximately 50 nm; according to the following electroplating equation.

$$Q = \frac{nF\rho A\mathbf{h}}{Mf}$$

$$t = Q/I$$

Where Q is the charge needed to electroplate an area (A) by a certain thickness ($\mathbf{h}$); with n, ρ, and M being the ion charge, density, and molar mass of the transition metal being electroplated, while f is the coulombic efficiency – assumed to be 90%. The time (t) required for electroplating is dependent on the charge and current (I) used.

3) Immediately after electroplating, samples are quickly rinsed with ethanol to avoid uneven deposition from the plating solution attached to substrate and avoid oxidation of the catalyst layer.

At this stage, samples are ready for CNF growth.

4.1.2   Carbon Fiber Growth

Stainless steel strips coated with NiCu catalysts are inserted into a quartz tube that is loaded inside a temperature controlled furnace. Annealing in H_2 at 650 °C for 1 hour prior to growth is performed to form catalyst nanoparticles and to reduce any metal-oxides back to metallic state. The growth temperature is maintained at 650 °C for a duration of 20 mins in an atmosphere of C_2H_4-H_2 gases, supplied at various flows rates. During cool-down, H_2 atmosphere was maintain to prevent oxidation of fibers.

4.1.3 Electrochemical Testing

Electrochemical measurements were conducted using a BioLogic SP-200 potentiostat. Pt mesh electrode and Ag/AgCl (sat. KCl) electrode were used as counter and reference respectively. The synthesized samples were directly used as working electrodes, with their contacts mechanically polished before testing to minimize contact resistance. KOH and $HClO_4$ solutions were used as electrolytes in DI water.

4.2 Results and Discussion

4.2.1 Carbon Fiber Synthesis

When H_2SO_4 is used to etch SS, a black film coating of $Fe(SO_4)_2$ forms, this film is not removed prior to electroplating. After plating NiCu a red rust-like coating is formed as seen in Figure 4.3. HCl etching results in a clean and shiny stainless steel surface, once plated a yellow-blue tint can be observed on the surface, see Figure 4.3.

After growth, a black velvet-like film of CNFs can be observed on the electroplated area, which shows the selectivity of growth to the engineered catalyst layer deposited. The morphology of the carbon nanofibers are shown in Figure 4.1. The SEM images demonstrate the uniform distribution of CNFs on top of stainless steel although some amorphous carbon can be observed. Ni is known as a very active catalyst for CNF formation.[59,137,143–146] Additionally, Cu is known to produce graphene due to the limited solubility of carbon in Cu. The Cu portion of catalyst can be the source of the amorphous flakes observed on the surface of CNFs.[144,145,147,148] Synthesizing CNFs permits a larger lateral processing window and the creation of a hierarchical architecture through the formation of CNF bundles.

Raman spectroscopy gave us a better idea of the degree of graphitic vs. amor-

phous carbon that our fibers posses. Figure 4.2 shows that a large part of our fibers are graphitic in nature; this includes the walls of the fibers, as well as some of flakes that retain graphene-like structure.[149–152] The D-band observed is expected due to two main reasons, primarily, the use of Ni as catalyst is known to produce a mixture of carbon fibers and amorphous carbon,[143,145,147] and secondarily, the samples did not go through any purification process to remove amorphous carbons.[149–152]
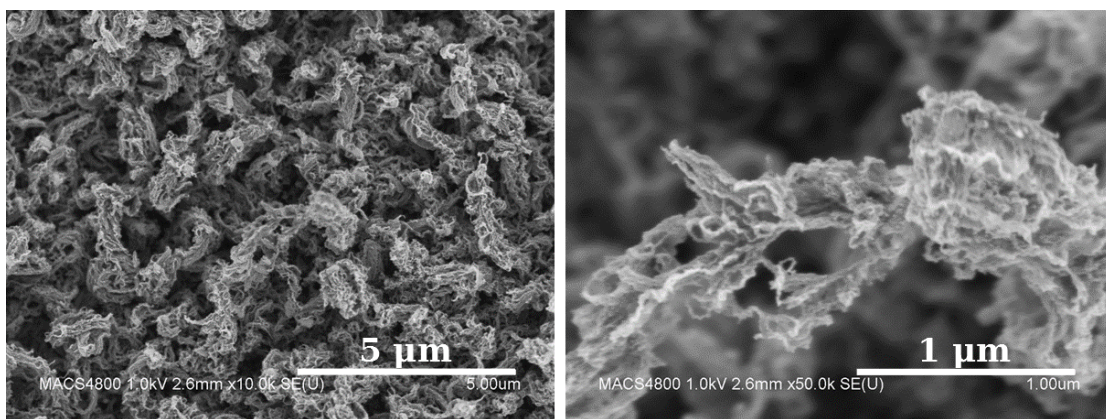
Figure 4.1: Typical SEM images of as-grown CNF sample. Good spatial distribution (Left) is observed and some amorphous carbon flakes are also present on the surface of some CNFs (Right).
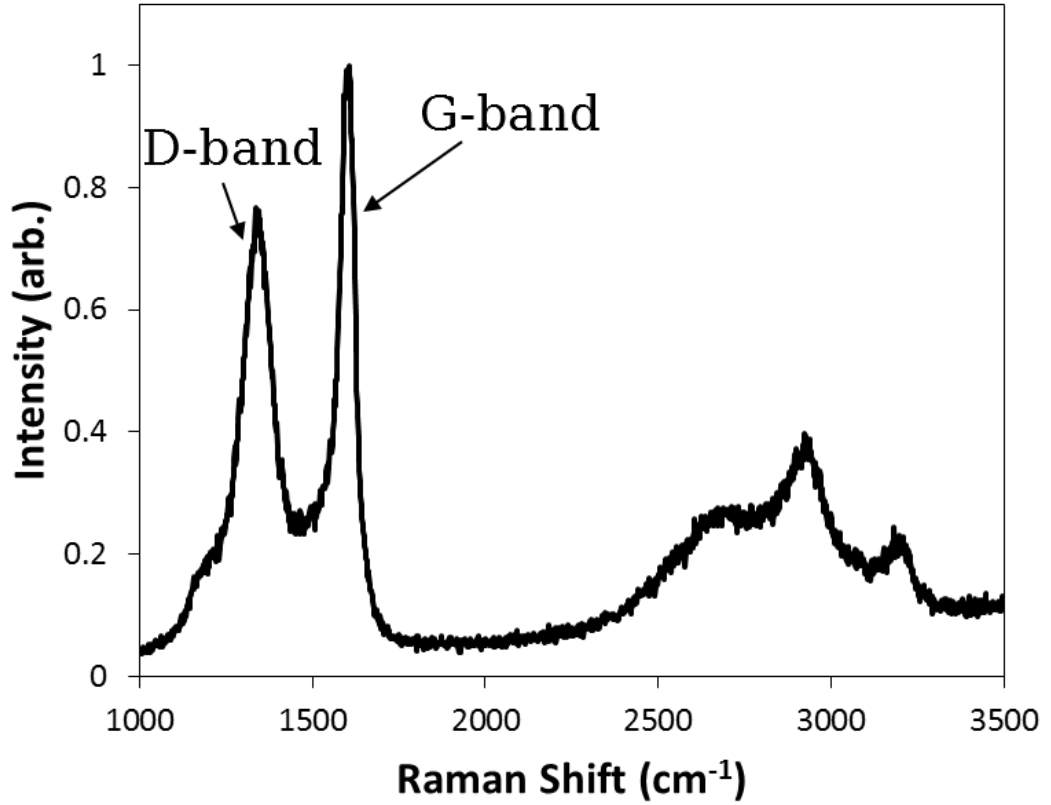
Figure 4.2: Typical Raman spectroscopy of as-grown CNFs. Demonstrating significantly larger graphitic nature (G-band) over the disordered or amorphous carbon (D-band).

4.2.2 Processing Effect on Capacitance

Although not visible, the electrochemical performance difference between the two substrate etching approaches are clear. In Figure 4.3, H_2SO_4 treated samples (solid red line) demonstrate a 4.7-times larger electrochemical capacitance than its HCl counterpart (dashed line), under otherwise identical conditions. We attribute this difference of capacitance to the physical catalyst layer utilized prior to growth. Figure 4.4 shows SEM images at different processing stages of stainless steel that lead up to CNF growth. It is clear that smaller and more uniformly distributed catalyst nanoparticles are produced by the H_2SO_4 treatment than from the HCl treatment. Since the growth of CNF is dictated by the size and location of catalyst particle,[144,146,147] it is expected that more carbon nanofibers will result from a

more spatially dense catalyst loaded sample. The higher spatial density of CNFs results in an enhanced electrochemical double layer capacitance (EDLC). This realization is of great importance to this study because *I am able to correlate EDLC to the catalysts processing instead of growth processes* – which is often the primary variable for carbon fiber growth and capacitor studies.[134,136] To quantitatively compare the capacitive performance, the following equation is used on cyclic voltammetry experimental results:

$$C_{CV} = \frac{\int_{V_a}^{V_c} I_V \ dV}{m \ \nu \ (V_c - V_a)}$$

Where the cyclic voltammetry capacitance (C_{CV}) is calculated from the integration of the current response to the voltage applied (I_V) divided by the potential window ($V_c - V_a$), scan rate (ν), and either mass or geometric area (m) of the sample.

Capacitance changes due to growth conditions were also performed to ensure that the synthesis procedures were optimized. Figure 4.5 summarizes the results of such optimization.
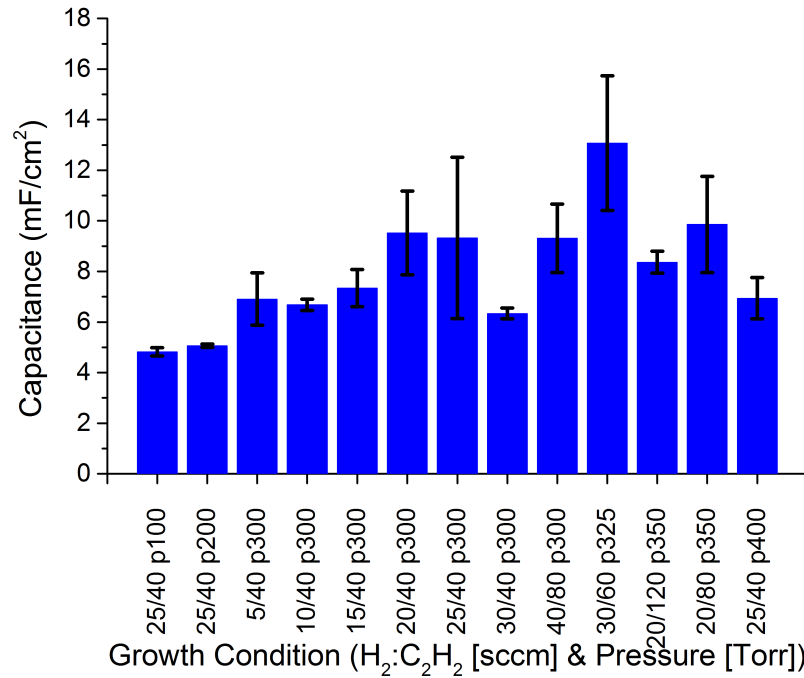
Figure 4.5: Effect of growth conditions on capacitance. All growths occur at 650 °C for 15 mins.
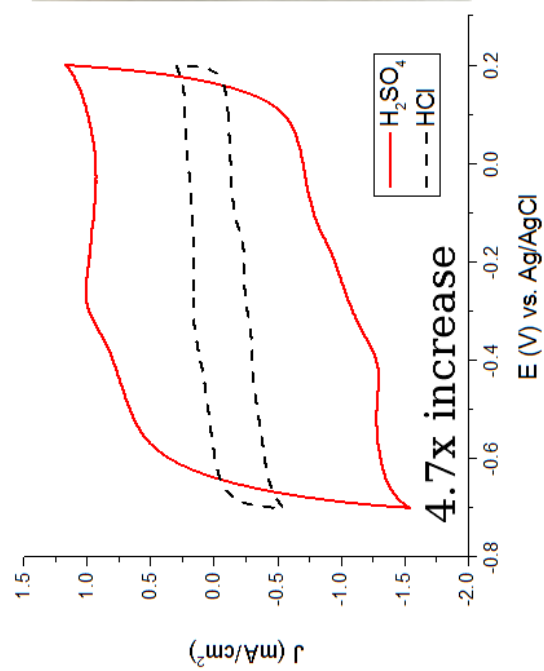
Figure 4.3: Cyclic voltammetry demonstrating the effect of etching on electrochemical capacitance (Left). Digital photographs of HCl and H_2SO_4 etched stainless steel substrates after electroplating NiCu catalyst (Middle) and after growth (Right).
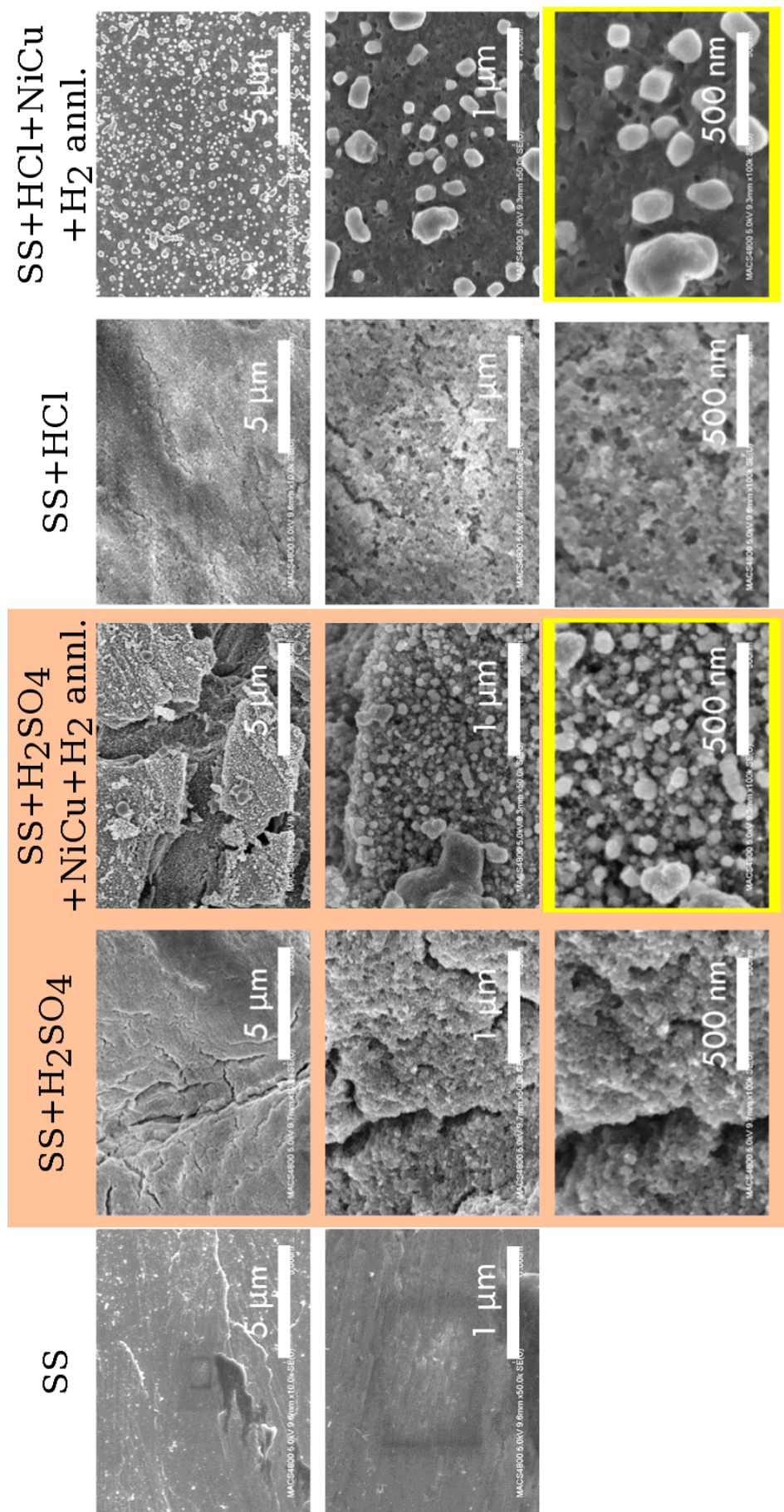
Figure 4.4: SEM images of stainless steel foils at different stages of catalysts preparation. For distinction, sulfuric acid etched samples are surrounded by a box. H_2SO_4 show a nanotextured surface while HCl shows a smoother textured surface. At the final processing stage (yellow box), it is observed that H_2SO_4 samples have smaller more uniform nanocatalyst particles than HCl treated sample.

Direct growth of nanostrucutres on metallic current collectors have shown to improve contact resistance and electron transport.[121,134,137] To this end, 316 stainless steel was selected as substrate electrode due to its chemical and thermal stability when compared to other steels such as 304. Direct growth of carbon nanotubes has been performed on other high performance alloys such as steels, Ni, Al, and Inconel®, but in terms of availability, price, and research, 316 stainless steel is a better candidate.[80,136,137,144]

To demonstrate the benefits of direct growth for CNFs, I conducted experiments where I removed the fibers from the substrate and re-attached them using a conventional method with binder material. The results in Figure 4.6 shows that more than half of the capacitance is lost due to the blocking effects of the binder and the random electron pathway resulting from CNFs laying flat on the substrate, with many of the CNFs not possessing direct contact with current collector.[124,134,153] The ability to have a high EDLC and maintain vertical alignment makes this CNF electrode ideal for use as the platform for other electrochemical applications.
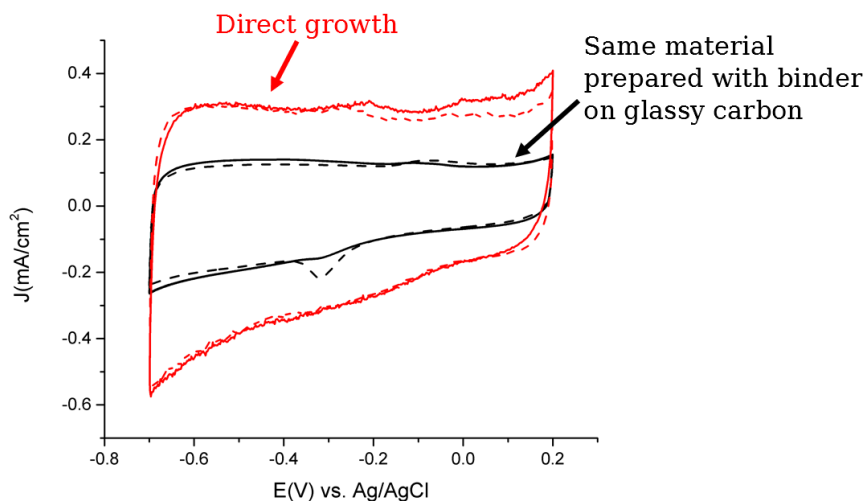
Figure 4.6: Cyclic voltammetry of the same CNFs sample, while attached to stainless steel substrate (**red**) and when prepared by post-assembly with binder material (Nafion®) on glassy carbon (**black**). Charge storage capability is lowered when using binder.

4.3   Future Work

Room to improve the design of this carbon electrode exists. Primarily and for scientific importance is the effect of other strong acids etching on the electrochemical capacitance. Aiming to discover if these acids influence the catalysts preparation, resulting in different nanocarbon morphologies and EDLCs.

Another more involved study would be to investigate the alloy chemistry responsible for the CNF growth, particularly at the interface. Since limited attention was given here when creating the Fe-Cu-Ni interface during electroplating, and the ratio of the two catalysts (NiCu) was not adjusted or enhanced. Primary catalysts to pursue are the carbon nanotube inducing catalysts such as Mo, Co, or Au.[57,59,146] This study would require the extensive use of XPS and XAS to characterize the catalysts, and more detail procedures for electroplating. The possible results of the proposed investigation can result in electrodes with two-fold increased capacitance than the here presented.

In order to have more play room with catalysts and growth conditions while retaining direct growth, a more chemically and thermally stable substrate should be utilized. Stainless steel was selected here for its decent chemical and thermal stability, market availability, and well known properties, but engineered space-age metal-alloys should be considered, looking primarily at nickel-based alloys such as Inconel®.

4.4   Conclusion

To conclude this chapter, a new carbon nanofiber electrode fabrication design was introduced. This approach shows enhanced growth of CNFs with large EDLC due to the effects of H_2SO_4 etching on the catalyst preparation. Systematically, we demonstrated that more spatially dense nanocatalyst are responsible for enhanced fiber growth. The direct growth of CNFs on stainless steel allows for direct

synthesis-to-testing ability of the produced electrode. In doing so, detrimental effects from conventional binders are avoided, such as blocking of the electro-active area and random electron pathways. Therefore, I successfully design a reliable carbon nanofiber electrode platform. This realization is necessary for supercapacitors and electrochemical applications including batteries, chemical sensors, and fuel cell catalysts electrodes.

Chapter 5

Oxygen Functionalities that Induce Pseudocapacitance

Functionalization of carbon materials, specifically graphene and CNTs, has been shown to increase the capacitive performance, primarily from pseudocapacitance. Heteroatoms, as they are often referred to, induce new electronic states, or tend to alter the morphology by increasing the available surface area.[127,154–159] Nitrogen and oxygen heteroatoms have been studied since they are easily synthesizable and are compounds are often found in nature.[87,154,156,157]

Nitrogen doped carbons (NC) for supercapacitors can be synthesized by two main approaches. The first approach is direct synthesis that results in homogeneously doped carbons such as those derived from the pyrolysis of nitrogen containing polymers or biomass.[34,130,148,156,160,161] The second approach is by surface functionalization which relies on destructive means such as hydrothermal treatment, annealing, or plasma-etching in a nitrogen environment.[162–171] At moderate doping levels, nitrogen can increase the conductivity of graphene, which can be understood by assuming that quaternary-nitrogen is formed (N-Q).[36,162] In alkaline media, the NC can undergo faradaic reactions, increasing capacitance.[156] Because doping nitrogen into carbon occurs by the substitution of a carbon atom, NC tend to have textured surfaces that can induce larger capacitances.[36,160]

However due to the destructive nature, it is hard to study the properties of NCs without disturbing the properties of the supporting carbon electrode. Oxygen doped carbons on the other hand are better suited to study the functionalizaton of carbons. Most functionalities between oxygen and carbon are attached to the carbon surface rather than substituted – this retains the properties of the graphitic carbon backbone.[132,172–174]

Redox reactions from functionalizing with oxygen groups are another mechanism to further increase intrinsic capacitance of carbon electrodes.[123,174–184] These groups improve wettability, and facilitate further exotic functionalization such as functional polymers or metal nanoparticles. The most common approach to functionalize carbon is with strong acids, which damages the carbon structure affecting the electrical properties. Since only the surface in contact with the solution can be functionalized, this approach it is considered to be inefficient. Generally, acid treatments utilize HNO_3 or a mixture of H_2SO_4-HNO_3 to break the carbon bonds and form -OH or -OOH groups at the end of carbon.[173,175,176,178,180,181,183] This approach is effective but offers little control over the penetration of functional groups. Air annealing however, is a more efficient way to functionalize surfaces but it is highly sensitive to over-oxidation (burn-off).[175,180,184]

It has been demonstrated that supercapacitors made of 3D carbons, coupled with strong faradaic reactions, are the future of high power and energy density for portable devices and hybrid/electric vehicles.[128,185–187] Therefore, *I investigated the supercapacitor enhancement from controlled air oxidized 3D heirarchical CNFs.* By using a reliable carbon platform, a direct study of the surface functionalization is possible. The robust and consistent morphology of CNFs from the previous chapter allows the fundamental study of carbon properties before and after oxygen functionalization. I demonstrate a 130% (30%) increase capacitance in base (acid) electrolyte, due to the hierarchical CNF structure and the induced surface oxygen groups. The 1D CNF morphology provides high surface area for funcitonalization

and the direct growth provides fast electron transport for expedite redox reactions.

5.1 Experimental

All the parameters for CNF growth remain the same from the previous chapter.

5.1.1 Functionalizing CNFs

The schematics of functionalization are presented in Figure 5.1.

- **Air**. Functionalizing with air was performed in a temperature controlled furnace at distinct times and temperatures while the tube ends were left open to the atmosphere. Temperature was gently increased to the set temperature over the span of one hour. At the end of the process, the furnace was allowed to cool down below 200 °C before opening, to avoid thermal shock.

- **Acid**. To compare with acid functionalized carbons, HNO_3 etching was utilized. Samples were loaded into a glass vial which was then closed with a Septa cap. House vacuum was applied to the vial for 20 mins to remove trapped air between the fibers before inserting 10 ml of 3 M HNO_3, via syringe and subsequently restoration of atmosphere pressure. Different times of etching were studied. After etching, samples were rinsed thoroughly three times in DI water before electrochemical testing.

5.1.2 Characterization

The experiments were carried out at beamline 7.0 at the Advanced Light Source (ALS) at the Lawrence Berkeley National Laboratory (LBNL) by Dr. Yifan Ye. Near-edge X-ray absorption fine structure (NEXAFS) spectra were recorded by measuring the total electron yield with 0.25 eV and 0.40 eV resolution of the beamline monochromator for both the carbon and oxygen edges, respectively.
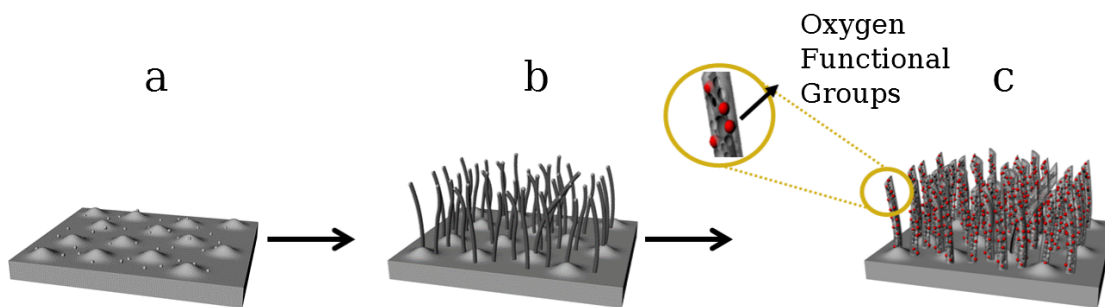
Figure 5.1: Schematic of the process to functionalize CNFs. a) Roughened stainless steel with NiCu catalyst. b) CNFs grown on stainless steel. c) CNF functionalization by either air annealing or acid etching. **Note**: Fiber morphology is not modified by processing.

This undulator beamline includes a spherical-grating monochromator and provides linearly polarized synchrotron radiation of high resolution and high brightness. The NEXAFS spectra were normalized to the incident photon current using a gold mesh inserted in the excitation beam. Total electron yield (TEY) and total fluorescence yield (TFY) were recorded to compare the chemical composition at different penetrations, surface (1-10 nm) and bulk (10-100 nm) respectively.

High resolution scanning electron microscope (SEM) images were personally recorded using a Hitachi S4800 SEM in NASA Ames Research Center. Electrochemical measurements were conducted using a BioLogic SP-200 potentiostat. Pt mesh and Ag/AgCl (sat. KCl) were used as counter electrode and reference electrode respectively. The prepared samples were directly used as working electrodes, with contacts polished to minimize contact resistance. KOH and $HClO_4$ solutions were used as electrolytes in DI water.

5.2 Results and Discussion

5.2.1 Physical Characterization

After growth stainless steel foils have a black, velvet-like coating of carbon fibers. If growth temperature exceeds 650 °C, the foils become brittle, developing a tendency to snap when subsequently handled. SEM images in Figure 5.2 show ran-

domly oriented groups of carbon nanofibers (bundles). Good spatial periodicity is observed, with a predominant bundle width of ~600 nm. Carbon nanofibers are observed parallel to each other and with minimal branching. Bright nanoparticle clusters appear at the middle and tip of nanofibers, demonstrating that the nanoparticle catalyst directs the growth of the fibers.[59,137,143–146]

The bundle to bundle distance provides macroporous spacing, while fiber-to-fiber distance provides mesoporous spacing, creating the hierarchical structure. Small bundles have a diameter ~20-27 nm and are composed of 2-4 fibers. Large bundles can have sizes ranging from 180-570 nm in diameter. The large spread in bundle size is due to the nanoparticle clusters whose sizes are difficult to control due to the rough surface of the stainless steel. The growth mechanism using nickel and copper catalyst is neatly explained by other groups and supported by our results; the explanation is presented in the previous chapter.[137,144]
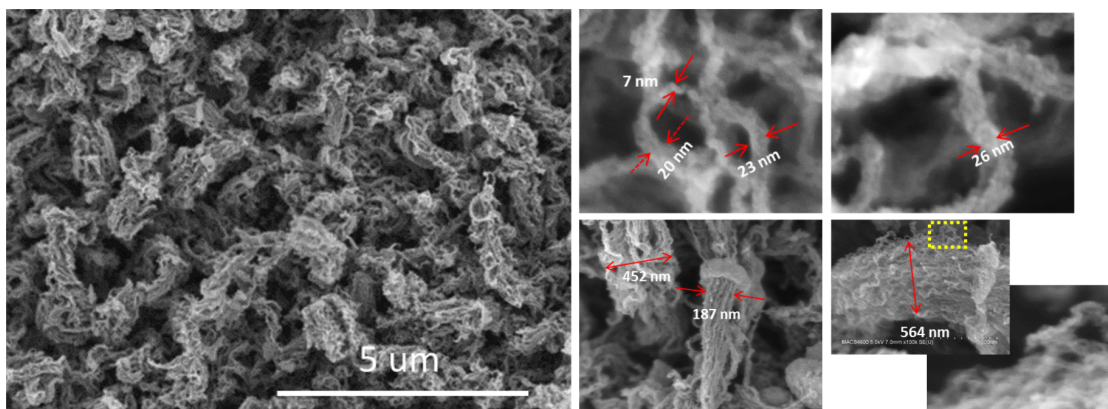
Figure 5.2: SEM images of CNFs demonstrating the hierarchical structure. Large periodic bundles are observed which provide macroporous spacing (Left). More highly magnified images show smaller fiber-to-fiber distances which provide mesoporous spacing (Right).

To study the functional groups present on carbon fibers, NEXAFS measurements were conducted and are shown in Figure 5.3. Typical C K-edge peaks for sp^2-like graphitic carbons are observed and marked as A for π^* (C=C) and B for σ^* (C-C) at 285.5 and 292.5 eV respectively in Figure 5.3(a).[188–190] To compare functionalization results, oxidation by air annealing and with nitric acid

were employed. Oxidation of the CNFs results in a new peak, C, at 288.5 eV which corresponds to the π^* (C=O) sp^3-hybridized states due to oxygenated surface groups such as COOH.[188,189,191] Interestingly, the TFY spectra (bulk) of air anneal sample, in Figure 5.4(a), does not show peak C, but it is present for acid treated samples, Figure 5.4(b). This result validates the selectivity of air oxidation to functionalize CNF surfaces. The O K-edge results between as-grown and air annealed are presented in Figure 5.3(b). Two prominent peaks can be observed, E at 539.7 eV and D at 531.2 eV. Peak E is associated with σ^* (C-O) from hydroxyl groups while peak D is related to the π^* (C=O) originating from COOH.[188,189] By comparing the ratios of E/D we can deduce whether functional groups have been introduced. Although the as-grown sample has different TEY and TFY profiles, the E/D ratios are above 1.85. On the other hand, the air annealed sample show similar TEY and TFY profiles with a E/D ratio of 1.77; this could be evidence that more C=O bonds have been formed. The small peak at 534.6 eV has not been identified; however, due to the proximity to 535.4 eV σ^* (O-H), it could be assigned to this hydroxyl group.[188] Additionally, the region beyond 550 eV does not return to zero for air annealed sample, plausibly due to the resonant carbonyl peak.

Damage to the bulk of the fibers from oxidation can lead to poor performance due to decreased conductivity. Groups have shown that oxidizing and by consequence exfoliation of carbon nanotubes can increase the electrochemical performance, providing high surface area 2D graphene and quinone-type redox centers. Ideally only the surface needs to be functionalized or exfoliated, leaving the inner walls intact to act as electrical conductors.[38,178,180]

The clear difference between the C K-edge TFY spectra of acid treated and air annealed samples in Figure 5.4 shows that the bulk of the acid treated sample has been functionalized, which means that the integrity of the CNFs has been altered. In contrast, the TFY spectra of the air anneal sample are still similar to
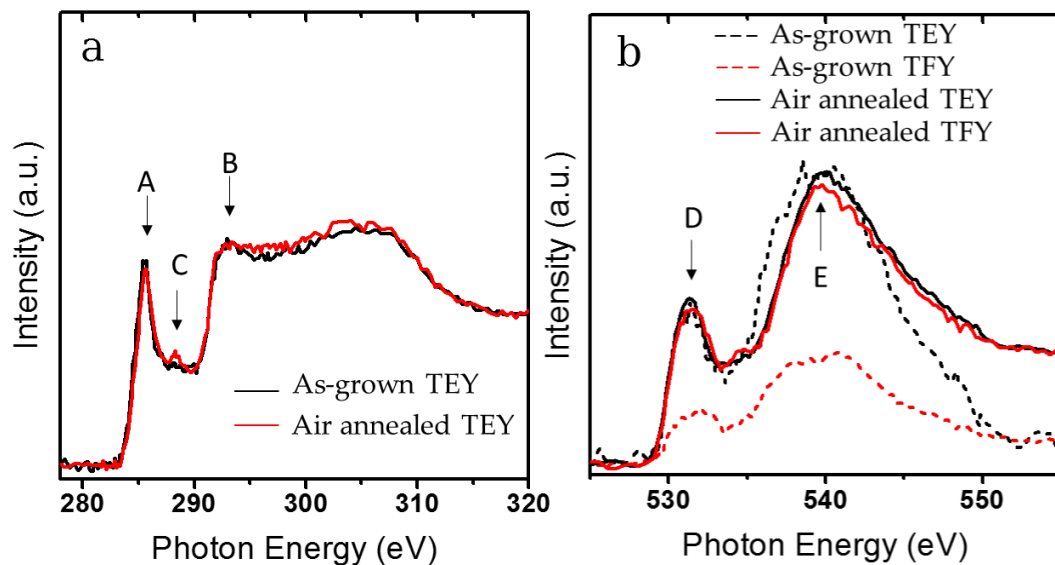
Figure 5.3: NEXAFS before and after oxygen functinalization. a) The C K-edge spectra. b) The O K-edge spectra.

the as-grown sample spectra; thus, inner fiber integrity is maintain. Dai's group and others have shown the importance of retaining the integrity when exfoliating carbon nanotubes.[38,192]

5.2.2 Electrochemical Characterization

Many groups have recently shown increased capacitance from functionalized carbon nanomaterials. The most commonly explored functionalities are nitrogen, oxygen, and boron either alone or combined.[127,154–157,159] Their increased capacitance is a result of morphology change, improved wettability, redox reactions, and disruption of the local electron density.

To enhance the capacitive performance, I elected to introduce oxygen functionalities to the surface of CNFs. The most popular approach to functionalize carbons with oxygen is chemical etching,[172,193,194] which for loose carbons is effective but not for direct growth, since one desires to retain the morphology and integrity of the nanostructures. Therefore, high temperature oxidation in air is a better approach to functionalize carbon nanofibers. The temperature driven process is surface selective and environmentally friendly with no chemicals required
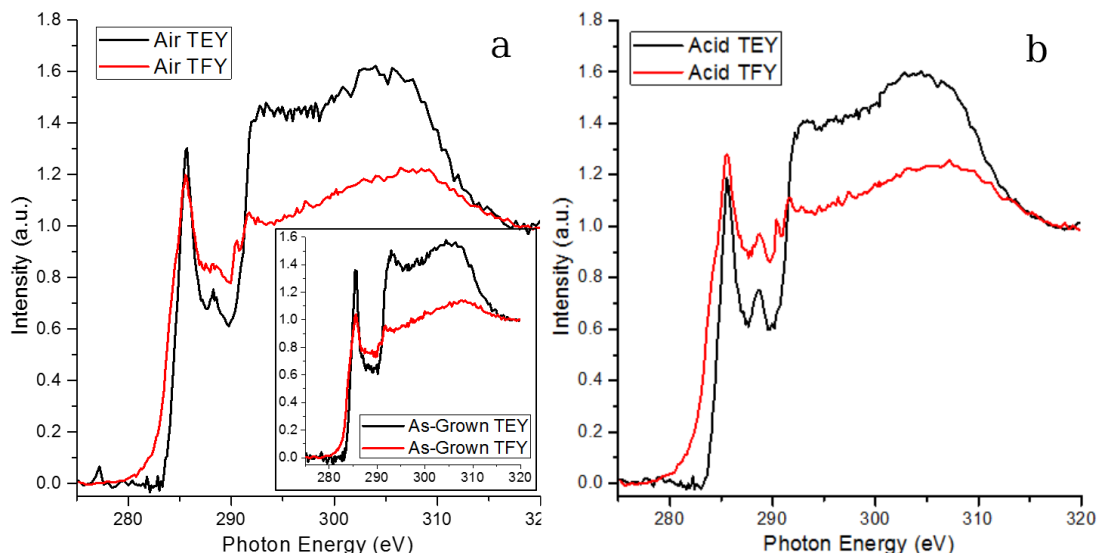
Figure 5.4: NEXAFS comparison of air annealed vs. acid functionalized CNFs. a) C K-edge TEY (**black**) and TFY (**red**) of air annealed sample with an inset of as-grown sample. b) C K-edge of acid treated sample.

or waste produced.

The capacitive behavior of carbon nanofiber electrodes were analyzed in a three-electrode cell using KOH and $HClO_4$ aqueous electrolytes. The cyclic voltammetry (CV) in Figure 5.5 of as-grown electrode (solid line) shows a capacitance of 110 mF/cm². The semi-rectangular shape of the CV curves shows that little internal resistance is present, otherwise skew or slanted trapezoidal cures would be observed. The absence of a redox peaks in both acid and base media demonstrates that CNFs are free of redox centers. A small oxidation hump is observed in acid media only. This small peak has been attributed to the traces of iron from catalysts that undergo oxidation, since this peak disappears after extended cycling in $HClO_4$ or acid cleaning.

Effects of induced pseudocapacitance are distinct in $HClO_4$ than KOH. In $HClO_4$, the new induced redox peaks are centered at 0.3 V (Ag/AgCl) and attributed to the quinone-type functional groups.[123,132,172,175,176,178,182] Interestingly in KOH electrolyte, the electrochemical double later capacitance (EDLC) of air anneal sample can increase 130% from its as-grown form — more than the increase

in HClO$_4$ (30%). Furthermore, a broad faradaic reaction is present in KOH at potentials below -0.3 V (Ag/AgCl); unfortunately potentials lower than -0.7 V (Ag/AgCl) could not be investigated due to H$_2$ evolution.
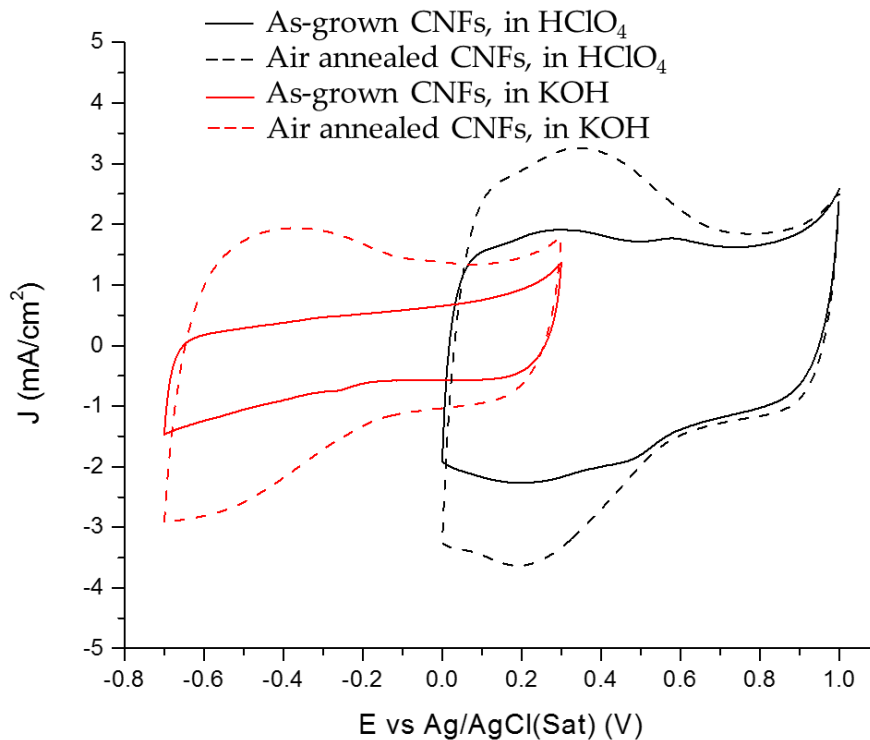
Figure 5.5: Cyclic voltammetry comparison before and after air annealing of CNFs in both KOH and HClO$_4$ electrolytes.

5.2.3 Pseudocapacitive Kinetic Study of Hierarchically Porous CNFs

High surface area 3D nanocarbons are commonly explored for electrochemical systems due to high surface area and stability. Research in these 3D nanocarbons soon revealed that hierarchical pore sizes can improve the performance in electrochemical systems by providing faster ion transfer and ion reservoirs. [125,140,195–198] Not until recently have the combination of all three capacitive improvements been combined: 3D high surface area, hierarchical pores, and redox centers. A bot-

tleneck to these improvements has been the redox kinetics, especially at the high operation rates of supercapacitors. Hierarchical nanocarbons with redox centers have shown to lose $1/3^{rd}$ of their maximum capacitance[125] or even close to half.[34] The electrode design here combats the loss of capacitance by benefiting from the direct growth of CNFs, retaining more than 90% of its maximum capacitance at higher rates.

The hierarchical spacing produced by the bundling of CNFs allows for fast ionic transport, while the 1D nanofibers provide large surface area with plenty of redox centers and a direct electron transport highway for fast redox reactions because they are directly connected to the current collector. The presence of clear redox peaks and a semi-rectangular shape at high scan rates (100 mV/s) affirm our claims of fast kinetic reactions and excellent active material coupling with the current collector.

To further investigate the kinetic performance of hierarchical CNF structures, CVs at scan rates between 5 and 100 mV/s were conducted and the results are shown in Figure 5.6(a). CVs at and below 100 mV/s show no distortion to their semi-rectangular shape and the redox peaks are clearly visible. The capacitance difference between 10 and 100 mV/s is less than 5%. At the slow scan rate of 5 mV/s the difference in capacitance from 100 mV/s is less than 10%. These observations clearly demonstrate the effectiveness of this electrode hierarchical structures to improve the kinetics of pseudocapacitors.

For practical applications, the galvanostatic charge and discharge (GCD) test were conducted and the results are shown in Figure 5.6(b). The GCD discharge curve shape of air annealed shows a shoulder initiating at 0.6 V (Ag/AgCl), assigned to the quinone-type faradaic reaction, agreeing in location with the reduction peak observed during CV testing. The effectiveness to retain its capacitance was tested with different discharge rates, between 0.88 and 17.5 A/g. Agreeing with the CV trend, the capacitance difference between 4.4 and 17.5 A/g is less

than 10%, while the difference increases to <40% for 0.88 and 17.5 A/g. A maximum capacitance of 213 F/g at 0.88 A/g was achieved for the Air anneal samples. A summary of the capacitance at different rates is presented in Table 5.1. The following equation was used for calculating the capacitance with GCD,

$$C_{GCD} = \frac{I \cdot \Delta t}{\Delta V \cdot m}$$

where the I is the applied discharge current, Δt is the total discharge time, ΔV is potential window, and m is the mass of the active material from TGA experiments (~ 1.5 mg/cm^2).
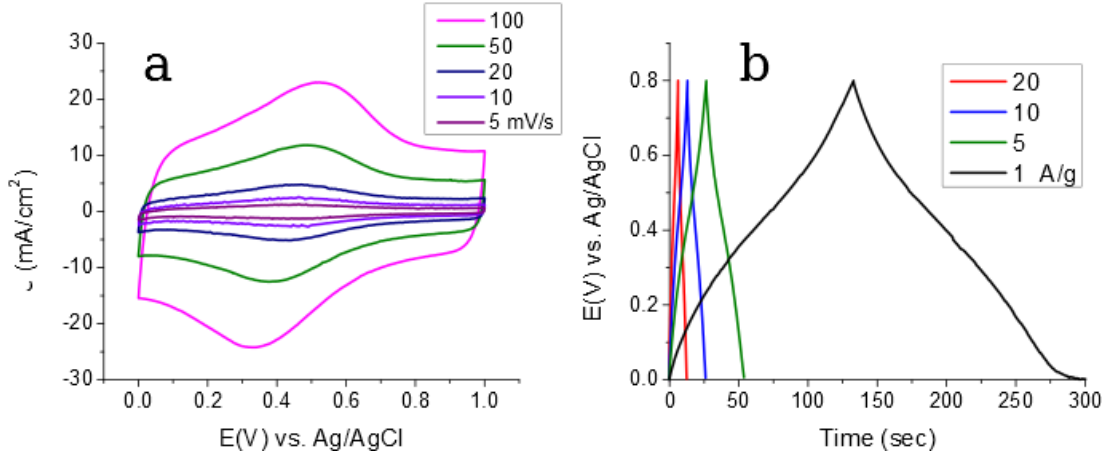
Figure 5.6: Kinetic study of hierarchical air annealed CNFs. a) Cyclic voltammetry at different scan rates. b) Galvanostatic charge and discharge of same sample at different discharge rates. Both test were conducted with HClO$_4$ as electrolyte.

Table 5.1: Kinetic Study of Capacitance

Cyclic Voltammetry		Galvanostatic Charge and Discharge	
Rate [mV/s]	Capacitance [mF/cm^2]	Rate [A/g]	Capacitance [F/g]
5	159.9	0.88	213.1
10	159.0	4.5	170.1
20	157.6	8.8	163.3
50	154.7	17.5	155.0
100	150.8		

In order to calculate the energy density, the carbon mass on stainless steel substrates was calculated by thermogravimetric analysis studies. CNFs were tested

by thermogravimetric analysis (TGA) while still attached to the stainless steel, subsequently a bare piece of stainless steel (from the same sample) is tested by TGA ans used as background, the mass loss difference amounts to the mass per geometric area of the sample. Test are conducted at 5 °C/min with air as the gas source.

5.2.4   Supercapacitor Properties and Stability of CNFs

To analyze the benefits of CNFs direct growth, I conducted electrochemical impedance spectroscopy (EIS) tests, the results are in Figure 5.7(a). A low x-intersect in the EIS is observed which is correspondent to the equivalent system resistance, including the electrolyte resistance, the intrinsic active material (CNF) resistance, and the contact resistance between CNFs and the current collector.[199] This demonstrates the good conductivity of the sample. No charge transfer resistance semi-circle is observed at high frequencies, instead a short 45° angle response at high frequencies is observed due to the fast ion diffusion in the hierarchical porous CNF structure.[35,192,200] At low frequencies a vertical capacitor response of the CNF electrode is observed.[192] For comparison purposes, the impedance of a processed stainless steel (all but CNF growth) was tested. Similar to CNFs, stainless steel shows no charge transfer resistance but unlike CNFs it does not show the vertical response of a capacitor, instead a 45° degree angle at low frequencies is observed due to Warburg behavior.[200,201] To verify of this conclusion, four-point probe measurements of CNFs on stainless steel and processed stainless steel were conducted. The results in Table 5.2 show the near identical sheet resistance between the two samples.

Table 5.2: Comparison of Sheet Resistances

Sample	SS (316) Exp.	SS+CNFs	SS+CNFs+Air annl.	SS (316) Theo.
Sheet Resistance ($\Omega/\square$)	0.016	0.018	0.022	**0.037**

To test the stability of air annealed CNFs sample, extended cycling in 2 M HClO$_4$ at 5 mA/cm^2 ($\sim$5 A/g) was conducted using a potential window between 0 to 0.8 V (Ag/AgCl). After 10,000 cycles, a maximum capacitance loss of 4% from the initial capacitance was observed (Figure 5.7(b)).
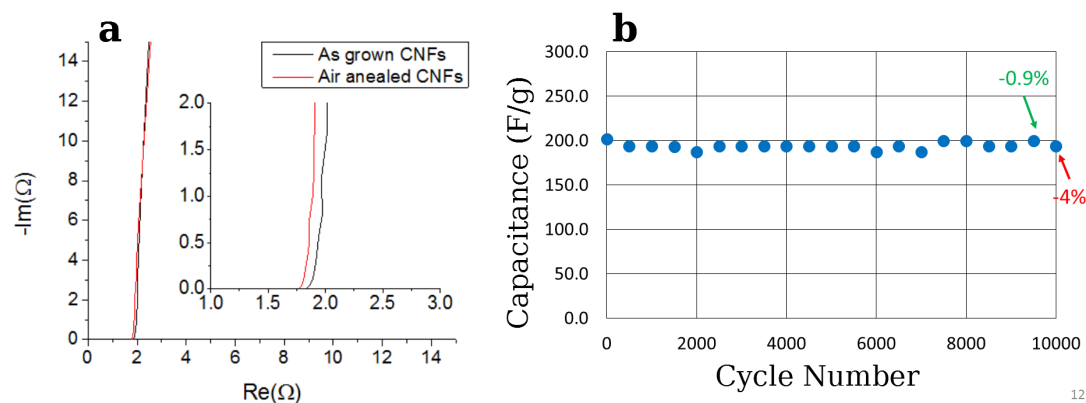
Figure 5.7: a) Impedance spectroscopy comparison of before and after air annealing. b) Stability testing of air annealed CNFs at 5 A/g. Tests were conducted with 2 M HClO$_4$

5.3 Future Work

The study of air oxidation can be applied to many other types of carbon, to see the possible induction of pseudocapacitance in activated carbons, carbon cloth, fullerenes, and graphene. The most interesting prospects would be to synthesize single (SW) or few-walled (FW) CNTs on stainless steel and then functionalize using air annealing. Intensive research can be expected because of the synthesis limitations presented, since the working temperature range of most chemically stable stainless steel are not compatible with SWCNTs processing. A great challenge but it has been demonstrated to be plausible.[202–204] Achieving this can shine more light at our proposed selectivity to functionalize the outer wall of CNTs by air annealing; even with simple electron microscopy characterization techniques.

Additionally, a better study of the properties of oxygen in functionalizing CNFs would be ideal. Here, for engineering purposes, I utilized an open-system with

ambient air as source of oxygen, for more scientifically accurate experiments, a close-system with pure oxygen should be utilized. Lastly, other elemental characterization tools such as FTIR, XPS, and thermogravimetric-mass spectrometry (TG-MS) to name a few, should be employed to investigate the functional groups formed and to tune these groups to enhance faradaic capacitance.

5.4 Conclusion

To conclude, I have demonstrated a novel approach to synthesize robust, stable, and high capacitance hierarchical carbon nanofiber electrode, grown directly on stainless steel current collector. This CNF platform allowed the direct study of the pseudocapacitive effects of oxygen functionalization by means of air annealing, and with NEXAFS, I am able to observe the selectivity of air annealing to functionalize the surface. Key points were the improved charged retention and fast redox kinetics made possible by the hierarchical CNFs structure. When combining with quinone-type functional groups, a significant increase in capacitance was achieved, with a maximum recorded of 213 F/g at 0.88 A/g. This binder free CNF electrode provides the ideal platform for multiple application such as batteries, oxygen reduction reaction catalyst, electrochemical sensing, and heteroatom doping studies.

Chapter 6

Oxygen Reduction Reaction from Nitrogen Coated Carbon Nanofibers

Fuel cells catalysts have improved in the last decade. The technology that once provided the lunar mission with clean water and electricity, has seen an awakening due to the impending need for a clean renewable source of energy.[205,206] The bottleneck of this technology has become the catalysis to reduce oxygen gas into ions, known as the oxygen reduction reaction (ORR).[39] This reaction is about five times slower than hydrogen oxidation reaction and thus requires five times more catalyst. The current state of the art catalysts is a platinum-carbon mixture (20 wt.% Pt/C), vastly used as a benchmark to compare other catalysts systems.[207] Recent research in non-precious metal catalyst (NPMC) has increased to substitute Pt as the active catalyst.[39,207,208]

Nitrogen-doped carbons (NC) are among the best NPMC. Their performance has been demonstrated to even exceed Pt/C, and due to its chemistry, it is environmental friendly and available from organic/biological sources, making it the ideal substitute as ORR catalyst. The substitution of the nitrogen on the carbon matrix plays three major roles; modification of the surface area and lattice spacing, alter-

ation of the electron spin density of nearby carbons, and due to nitrogen-carbon electron configuration, it allows carbon to more easily donate extra electron to an oxygen molecule.[209,210]

Utilizing the multipurpose electrode described in **Chapter 4**. We engineered a process to coat thin polymer coatings onto carbon fibers via electrodeposition. The CNFs acted as a stable and high surface area substrate, while the polymer became the nitrogen source upon its pyrolysis. *I studied the performance of distinct polymer coating approaches and poly(acrylamide) (PAM) based polymer complexes to catalyze ORR.* In addition, I investigated the effect of Fe and Cu metal co-catalysts on NC ORR performance. The results demonstrate that thin coatings of PAM with copper co-catalyst were had the best combined ORR performance.

6.1 Experimental

All the parameters for CNFs growth remain the same from previous chapters.

6.1.1 Nitrogen-doped Carbon Coating

The electropolymerization of PAM or PAM complexes have similar procedures as described in **Appendix B**. The overall procedure is as follows:

- **Monomer solution.** All monomers are purified either by distillation or by recrystallization. After purification, known solutions are prepared in DI water and stored in 4 °C refrigerator until needed.

  Diazonium method. For diazonium use, the monomer solution is acidify with H_2SO_4 until a pH of less than 2 is reached. The diazonium salt is then added to the acidic monomer solution and ultrasonicated until an uniform, translucent solution is obtained. Solution is stored in 4 °C refrigerator until needed. Methylene-*bis*-acrylamide (10 mol.% vs. monomer) crosslinker was used for crosslinked samples.

- **Prior to electrodeposition.** CNFs are loaded into a glass vial which was then closed with a Septa cap. House vacuum was applied to the vial for 10 mins to remove trapped air between the fibers before inserting 10 ml of monomer solution, via syringe and subsequently restoration of atmosphere pressure. Then the CNF sample and monomer solution are transfered to a plating vessel where all the proper electrode connections are made, and the solution is purged with continuous N_2 gas.

- **Electrodeposition**. Polymer coating was performed similarly to that in Section **3.1.2**. Cyclic voltammetry between -1.7 V and 0 V (Ag/AgCl) at a scan rate of 150 mV/s for the cathodic grafting and -1.0 V to 0 V (Ag/AgCl) at 10 mV/s for the diazonium method. Continuous N_2 purging is maintain throughout deposition. After coating, samples are rinsed in copious DI water to remove unreacted monomer and dried to be stored away for pyrolysis. Note: For cathodic grafting, Ammonium persulfate (5 mol.%) was introduced just before applying voltage, while the experiment was performed in an ice bath to slow down the solution kinetics.

- **Pyrolysis**. To form the nitrogen-doped carbon coating on CNFs, polymer coated samples are pyrolyzed in an argon atmosphere. Pyrolysis occurs inside a temperature control furnace and involves a 1 hr hold step at 150 °C to remove water, followed by another 1 hr hold step at 400 °C to assist the cyclization of the polymer, and a final 4 hr hold step at 650 °C to drive graphitization of the nitrogen-doped carbon. Between each of the hold steps, there is a 30 min temperature ramp-up sequence. Once finish, the furnace was allowed to naturally cool-down and it was opened after the temperature was bellow 200 °C.

6.1.2   Characterization

X-ray photoelectron spectroscopy (XPS, PHI-5000C ESCA system from Perkin-Elmer) was used the elemental composition of the nitrogen groups. Monochromatic Mg Kα with photon energy of 1253.6 eV was selected as the X-ray source. High resolution SEM images were recorded using Hitachi S4800 SEM at NASA Ames Research Center. Fourier transform infrared spectra (Nicolet 380 FT-IR) were collected to verify the efficiency of electropolimerization and to test the polymer cyclization at different annealing temperatures. Electrochemical measurements were conducted using BioLogic SP-200 potentiostat. Pt mesh and Ag/AgCl (sat. KCl) were used as counter electrode and reference electrodes respectively. The prepared samples were directly used as working electrodes, with contacts mechanically polished to minimize contact resistance. KOH and HClO$_4$ solutions were used as electrolytes in DI water.

- **Cyclic Voltametry**. Solutions of KOH and HClO$_4$ were purged with ultra-pure nitrogen or oxygen for 30 mins before testing. Cyclic voltammetry between -0.7 V and 0.2 V (Ag/AgCl) for KOH and between -0.2 V to 0.7 V (Ag/AgCl) for HClO$_4$ were used at a scan rate of 20 mV/s.

- **Rotating Disk Electrode**. To test the diffusion limited reaction, the samples prepared were pasted onto glassy carbon and tested by rotating disk electrode (RDE) technique. The ink was prepared by scraping the nitrogen-doped CNFs from the stainless steel substrate onto a solution of ethanol with Nafion® as binder material. Mass loading was controlled by the concentration of CNFs in the ink solution and the amount dispensed. Testing was performed using the Autolab software, with the same potential windows as the CV tests, for easy comparison. Similarly to CV measurements, solutions were purged in nitrogen or oxygen 30 mins before testing.

- **Rotating Ring Disk Electrode**. In order to test for the electron transfer

number and the catalysts efficiency to produce water, rotating ring disk electrode (RRDE) technique was implemented. Similarly to the RDE technique, CNF ink was pasted onto a glassy carbon electrode with a platinum ring as secondary electrode. Testing took place with the Autolab software, using the same potential windows for comparison. Similar to CV measurements, solutions were purged in nitrogen or oxygen 30 mins before testing.

6.2 Results and Discussion

6.2.1 Physical Characterization

Utilizing the electrode platform developed in **Chapter 4**, we are able to study the catalysis of nitrogen-doped carbon coatings for the oxygen reduction reaction. The schematic in Figure 6.1 depicts the processing stages to produce nitrogen-doped CNFs (N-CNFs), beginning with the growth of CNFs on stainless steel, followed by the electro-deposition of nitrogen containing polymers, and finally pryrolyzing to yield nitrogen-doped carbon film (with or without metal loading) on CNFs.

To demonstrate the ability to electropolymerize uniform coats on CNFs, Figure 6.2 shows SEM images of CNFs before and after polymer electrodeposition. It can be observed that the polymer deposits mainly on the outermost fibers but most inner fibers still shows signs of polymer coating. Important to notice is that the morphology of the original CNFs is not altered by this coating process.
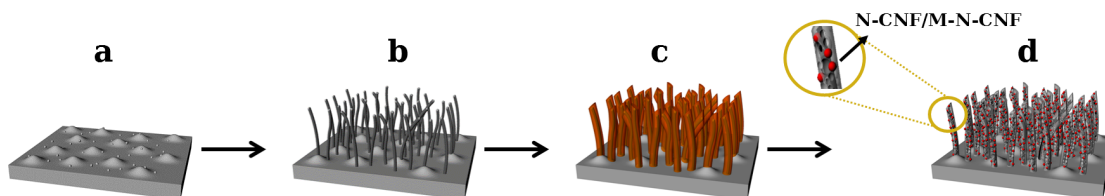
Figure 6.1: Schematics to produce nitrogen-doped CNFs. a) Roughen stainless steel with NiCu catalysts. b) CNFs grown on stainless steel. c) Polymer coated CNFs via electrodeposition. d) Pyrolyzed CNFs with coated nitrogen-doped carbon (with or without metal loading). **Note**: Fiber morphology is not altered by processing.
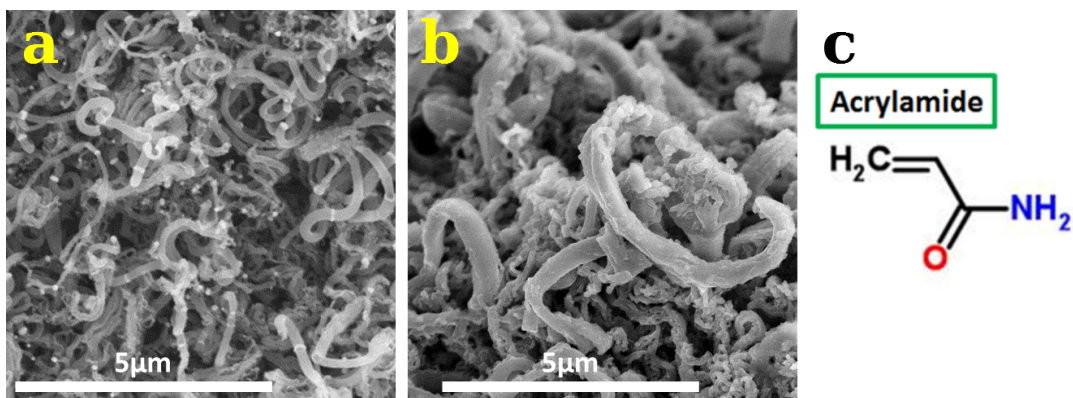
Figure 6.2: SEM images of Carbon Nanofibers: (a) as-grown and (b) after poly(acrylamide) coating. c) Acrylamide chemical structure provided for reference.

To achieve uniform polymer deposition, two approaches were investigated: conventional cathodic grafting and diazonium assisted electrodeposition. The schematics describing this electrografting techniques can be seen in Figure 6.3. For both electrodeposition methods, N_2 purging is needed to maintains the solution free of oxygen, which is an oxidizer and will terminate the radical polymerization. Purging also induces convection in the solution and dissipates H_2 or N_2 gas bubbles formed at the surface, thus providing fresh monomer solution and maintaining the surface free of obstructions for uniform coating.

In cathodic grafting a radical species (hydrogen-, metal-, or sulfate-ions) must be formed, which then radicalizes a monomer molecule in the solution. The polymer chain then propagates by means of radical polymerization, being preferentially attached to the substrate by electrostatic forces and by the terminal groups of the functional polymer used, amide in this case.[211–214] The potential for ideal cathodic electropolymerization was experimentally determined through electropolymerization at various cathodic potentials and comparison of resulting FTIR spectrum.

Diazonium assisted electropolymerization is another studied approach that is very effective at polymerizing on various substrates, particularly metals and carbon substrates. In my approach, the nitrobenzenediazonium (NBD) compound is

radicalized to a radical nitrobenzene groups which can easily bond to the carbon or metallic surface and act as an anchor functional group for chain propagation. Alternatively, the radical nitrobenzene can initiate chain propagation in solution and eventually graft-to the sample surface.[215–217]

To investigate the cyclization of nitrogen-containing polymer into nitrogen-doped carbon, FTIR technique was utilized. Poly(acrylamide) and poly(acrylamide)-co-poly(acrylonitrile) coatings were generated by cathodic grafting on bare stainless steel. Figure 6.4 shows the FTIR spectrum of such polymer coatings. After drying (RT, black line) we can clearly observe carbonyl peaks at 1650 cm^{-1} from acrylamide and a nitrile peak at 2245 cm^{-1} form acrylonitrile samples. After pyrolysis at 400 °C (red line) we observe a red shift in carbonyl peak to lower wavenumber and the disappearance of the nitrile peak. After 500 °C pyrolysis (green linec) we can only see two broad peaks (1600 cm^{-1} & 1325 cm^{-1}) which correspond to the C=C (aromatic), and C-N (aromatic amines) and C-O (carboxylic). Therefore by pyrolyzing polymer coatings we are capable to produce nitrogen-doped carbons; our results agree with previous pyrolysis reports.[212,214]

X-ray photoelectron spectroscopy was utilized to characterize the nitrogen groups created by the pyrolysis of polymer coatings. Using both electropolymerization methods I discovered that the diazonium approach produced less nitrogen functionalities than the cathodic grafting. Presented in Table 6.1, we observe that diazonium method (NBD-PAM) contains less than 1% of N species, while cathodic grafting (PAM) contains over 5% N species. Surprising as it may be, Figure 6.5 shows that the diazonium approach does have the benefit of producing largely graphitic-nitrogen, almost exclusively, with some pyridinic-nitrogen functionalities. These are assumed to be the functional groups responsible for ORR activity in nitrogen-doped carbons.[39,153,218]
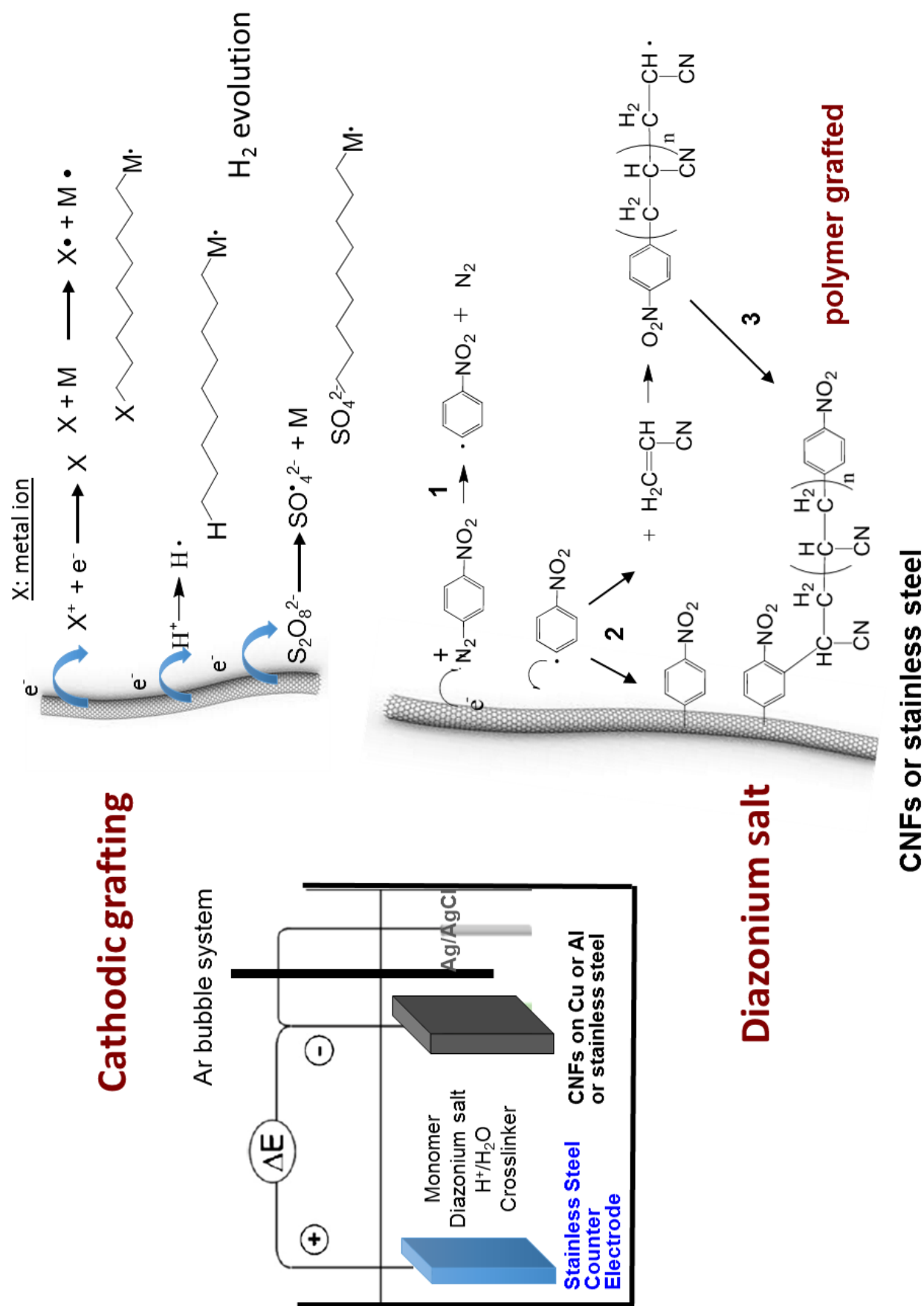
Figure 6.3: Schematic demonstrating electrodeposition by regular cathodic grafting or by diazonium assisted method.
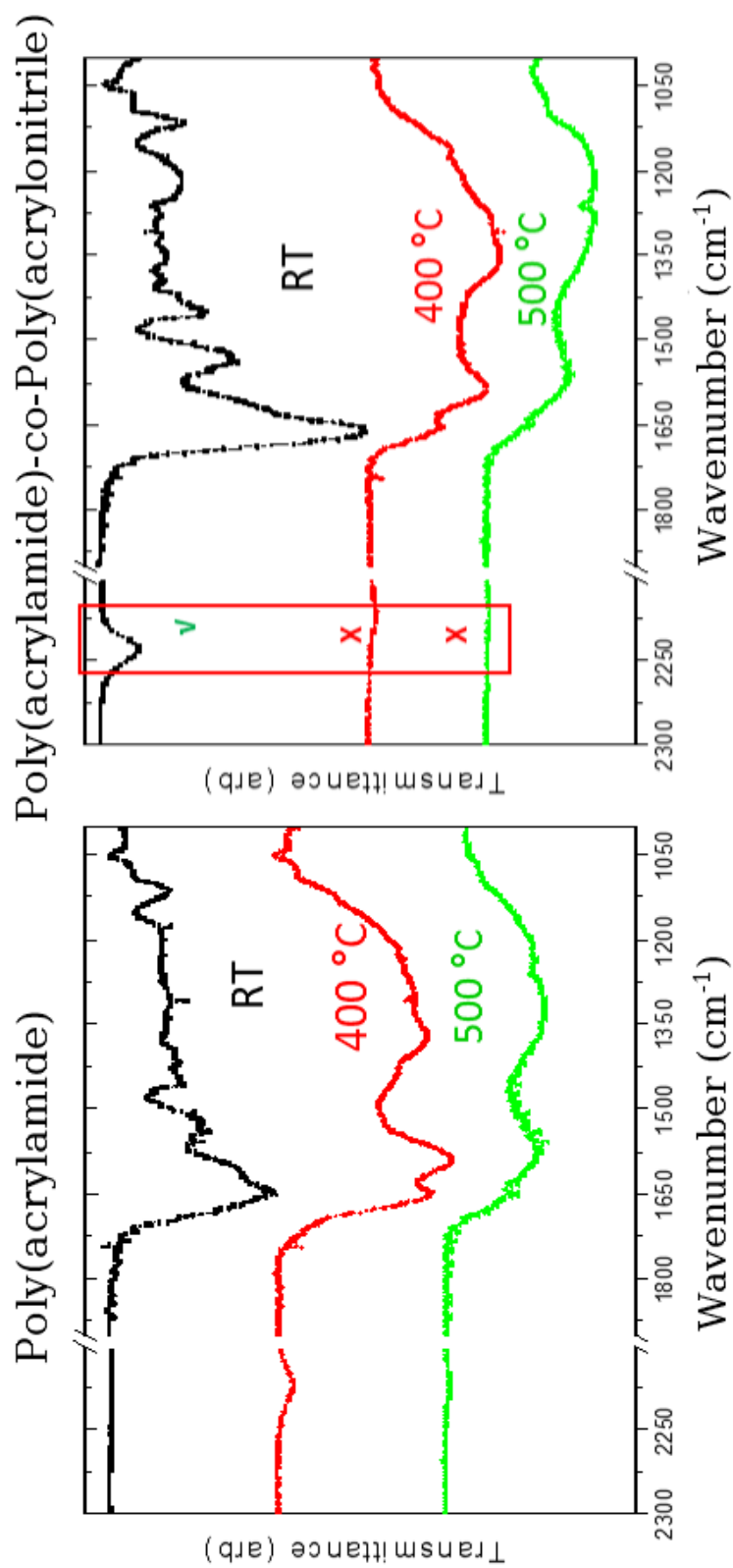
Figure 6.4: FTIR of PAM and PAM-co-PAN at different annealing temperatures. Shift of the carbonyl peak, and broadening of the C=C and C-N peak are observable with increasing of temperature. For PAM-co-PAN the disappearance of the nitrile peak is observed at higher temperatures (red box).

Table 6.1: Elemental Composition of Distinct Polymer Coatings Approaches

Method	C	N	O
NBD-PAM	89.78	0.98	9.24
PAM	84.98	5.17	9.87
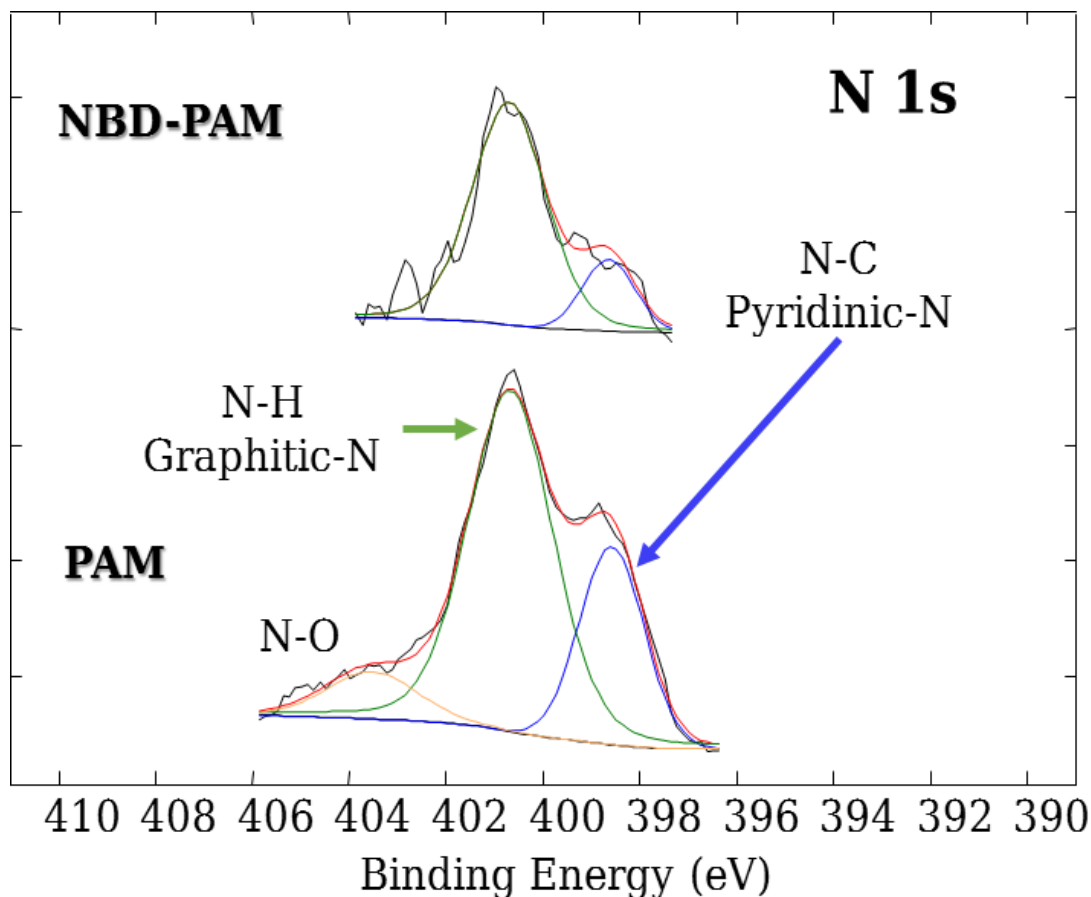
Figure 6.5: N 1s XPS of different electrodepositions methods with deconvoluted peaks to distinguish the nitrogen groups. (Top) Diazonium method and (Bottom) regular cathodic method.

6.2.2 ORR Performance of N-CNFs

The electrochemical performance of nitrogen-doped carbons were first tested by cyclic voltammetry experiments in oxygen saturated solutions and using nitrogen purged solutions as background. From Figure 6.6 we can observe that the as-grown fibers (CNFs) (blue line) exhibit moderate ORR performance, characterized mainly by a 2-electron transfer process which is observed visually by the

deviation around -0.4 V (Ag/AgCl). Nitrogen-doped CNFs (red line) show a far more positive onset potential and a more steady limited reaction profile. Some deviation by the N-CNFs in current gain is observed at lower potentials which is attributed to the pseudocapacitive behavior of nitrogen-doped carbons in KOH medium.[156,219] Because the current gain at high potentials (0.2 V (Ag/AgCl)) of N-CNFs and CNFs are near identical to each other, they correspond to the EDLC from the surface area of the electrode, therefore the ORR performance comparison is fair. To better investigate the ORR performance of these doped carbons, the diffusion limited reactions are needed.

Two Step	Direct
Two electrons	Four electrons
(1) $O_2 + 2H^+ + 2e^- \rightarrow H_2O_2$ (2) $H_2O_2 + 2H^+ + 2e^- \rightarrow 2H_2O$	$O_2 + 4H^+ + 4e^- \rightarrow 2H_2O$
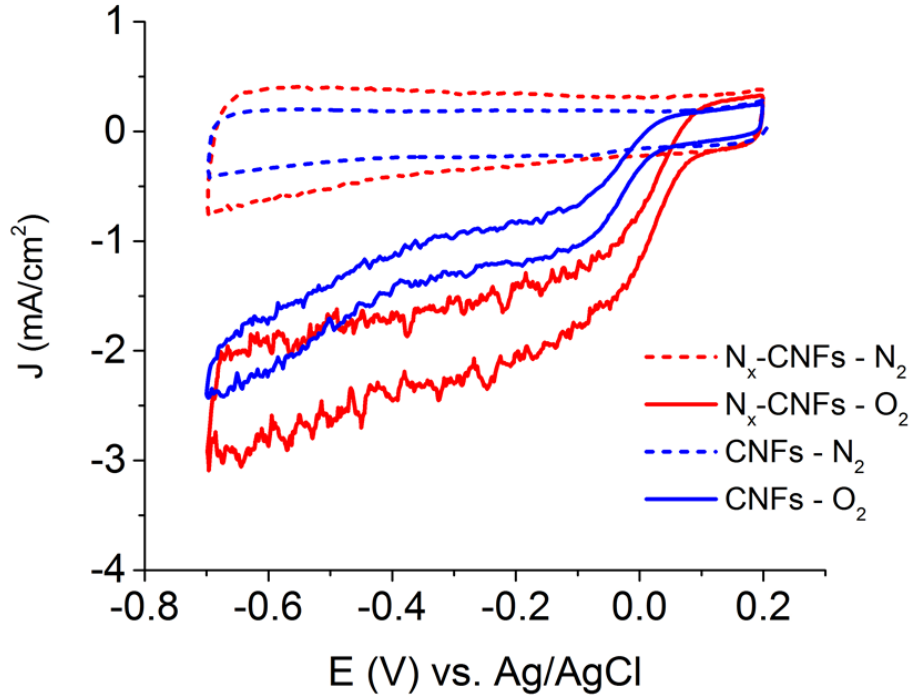
Figure 6.6: Cyclic voltammetry of N-CNFs (red) made of PAM by the diazonium method and as-grown CNFs (blue). N-CNFs show a more positive onset potential and a greater current density than CNFs only. Tested in 0.1 M KOH at 20 mV/s.

6.2.3 ORR Performance of Metal-N-CNFs

Rotating ring disk electrode experiments allows the fair comparison of distinct N-CNFs. Figure 6.2 shows the performance of N-CNFs and metal containing N-CNFs. Metal loading was accomplished due to the ability of the amide group to complex with metal-ions, by soaking polymer coated samples prior to pyrolysis. Comparing the performances we can observe that N-CNFs (red line) has the most negative onset potential and the largest H_2O_2 production of the set. Cu containing N-CNFs (black line) shows the largest current gain from all the samples tested, while Fe-N-CNFs (green line) showed the worst performance for metal-loaded samples in both onset and current gain, while still being better than non-metal N-CNFs. As expected, sample with both Fe and Cu (blue line) falls in between the Fe- and Cu-only samples for current gain, but exceed the performance of Cu for onset potential.
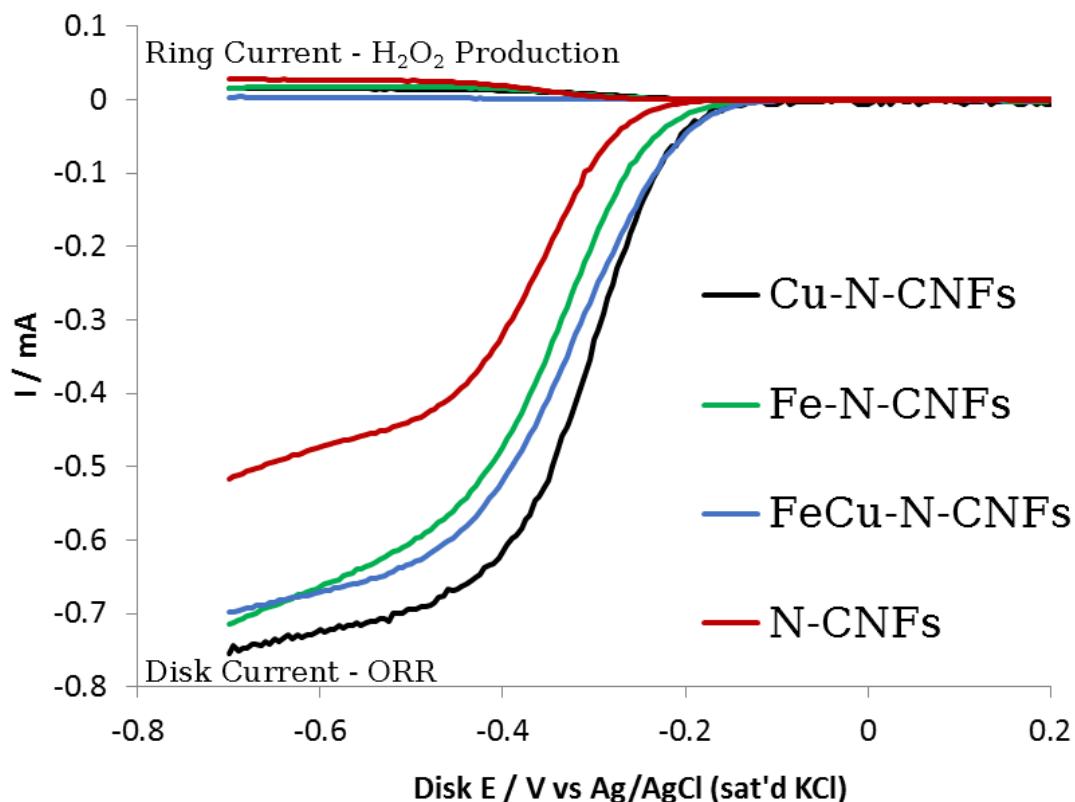
Figure 6.7: Rotating ring disk electrode plot comparison of distinct metals at 1,900 RPM. **Note**: Nitrogen contributions subtracted.

In order to quantify the performance among the distinct samples, we compare the amount of peroxide formation and electron transfer number. Both of these values are indicative of the effectiveness of the catalysts system to drive the direct oxygen reduction reaction. The equations are as follows.

$$\%H_2O_2 = \frac{I_R}{N \cdot |I_D| + I_R} \cdot 100\%$$

$$\mathbf{n} = 4 - 2 \left(\frac{\%H_2O_2}{100\%} \right)$$

Where $\%H_2O_2$ is the percent peroxide formation, I_R and I_D are the current gain at the platinum ring and disk electrode respectively, and N is the collection efficiency of the ring which is calculated from experiments with $Fe(CN)_6^{3-}$ [220] — a known redox reaction. The electron transfer number ($\mathbf{n}$) is calculated by the deviation from the direct (4 electrons) reaction depending on the amount peroxide produced. The results from Figure 6.7 are summarized in Table 6.2.

Table 6.2: Different Metals Rotating Ring Disk Electrode Performance Comparison using NBD Method

	Onset Ag/AgCl (sat'd KCl)	$\%H_2O_2$ ($\mathbf{n}$)
Cu-N-CNFs	-0.15	27.8 (**3.6**)
Fe-N-CNFs	-0.16	30.5 (**3.5**)
FeCu-N-CNFs	-0.16	3.40 (**3.9**)
N-CNFs	-0.20	46.7 (**3.1**)

Reports indicate that the presence of a metal species, here refereed to as co-catalyst, influence the production of ORR active nitrogen-doped carbons, mainly through the formation of porphyrins. Porphyrins are some of the earliest non-precious metal catalyst for ORR, although early reports utilized them while in molecular form and not as nitrogen-doped carbons.[126,207,221,222] The role of the metal co-catalyst is still debated.[38,209,223–225] We proposed that the metal co-catalyst plays a major role in the formation of the nitrogen-carbon active site,

and that after removal of the metal co-catalyst, the ORR performance would be retained. Utilizing our most active ORR catalysts, we tested its performance before and after removal of the metal co-catalyst by acid leeching. Figure 6.8 is the rotating disk electrode results of such experiment. The Cu containing sample (Figure 6.8(a)) shows the most positive onset potential and largest current gain. After the removal of the Cu by acid (Figure 6.8(b)) we observe a decrease in performance which is still higher than the performance of non-metal N-CNFs (Figure 6.8(c)). This results demonstrate that Cu co-catalyst plays an electro-active role in ORR performance on top of the porphyrin formation. Recent groups have demonstrated similar behavior with other metal and metal-oxide ORR catalyst.[38,224] The difference in performance between acid soaked Cu-N-CNFs and N-CNFs is therefore assigned to the role of Cu in forming distinct nitrogen-carbon functionalities, including porphyrins, that are more electro-active than the nitrogen groups formed by N-CNFs. The electrochemical results are summarized in Table 6.3, there we can observe that the efficiency order in terms of the electron transfer number ($\mathbf{n}$) is (Cu > Cu after acid > No metal). Values were calculated using the Koutecky-Levich equation.

"Koutecky-Levich" Equation:

$$\frac{1}{i} = \frac{1}{i_K} + \left(\frac{1}{0.620 \ \mathbf{n} \ FAD^{2/3}\nu^{-1/6}C} \right) \omega^{-1/2}$$

Where i and i_K are the measured current and kinetic current; while F is Faraday's constant, A is the area of electrode, and ω is the angular rotation rate. D, ν, and C are the diffusion coefficient, kinematic viscosity, and concentration of the oxygen species in the respective electrolyte.
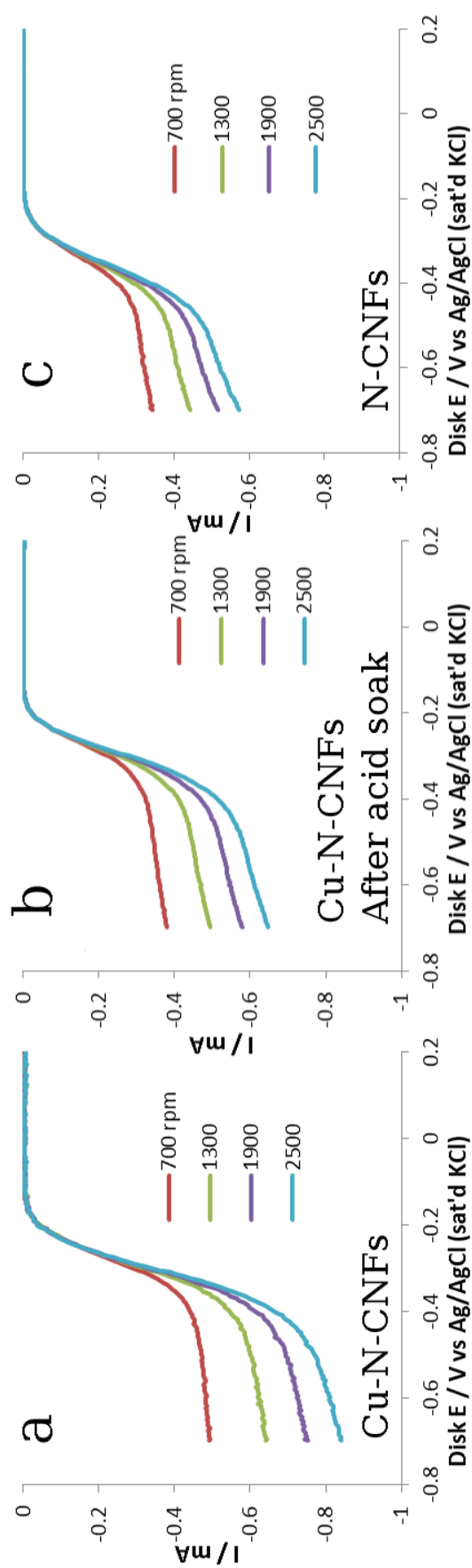
Figure 6.8: RDE plots showing the effect of Cu on ORR. a) ORR performance of Cu-N-CNFs. b) Performance Cu-N-CNFs after 1 hr acid soaking. c) ORR performance of N-CNFs without metal loaded. **Note:** Nitrogen contributions subtracted.

Table 6.3: Metal Effect Performance Comparison using NBD Method

	Cu-N-CNF	Cu-N-CNF After acid soak	N-CNF
E_{onset}(V) vs. Ag/AgCl	-0.150	-0.180	-0.175
E_{onset}(V) vs. RHE	+0.815	+0.785	+0.765
J(0.6 V) (mA)	-0.723	-0.549	-0.478
n	**3.7**	**3.3**	**3.2**

6.2.4 Benefit of Direct Growth for ORR

As mentioned in **Chapter 4**, the electrode platform benefits from the direct growth of CNFs. This effect was once again observed in ORR experiments. Comparing the exact same N-CNFs while still attached to stainless steel, and after removal and re-attachment by conventional approaches, I noticed a change in onset potential which is shown in Figure 6.9. The enhancement of redox kinetics is assigned to the excellent electron coupling between the N-CNFs and stainless steel, and to the 1D architecture of CNFs that results in large surface area with plenty of redox centers along the length of the CNF. Whereas, the pasted N-CNFs does not benefit from the upright architecture and many of its redox centers are not available due to being covered by the binder. To make things worst, the direct electron pathway is replaced by random electron pathways, which may involve the electron transfer between two or more CNFs in order to reach the current collector, reducing the performance. It is worth to note that the larger current gain attained with the pasted ink is due to the RRDE experiment inducing a diffusion limited reaction and not the result of better ORR performance.
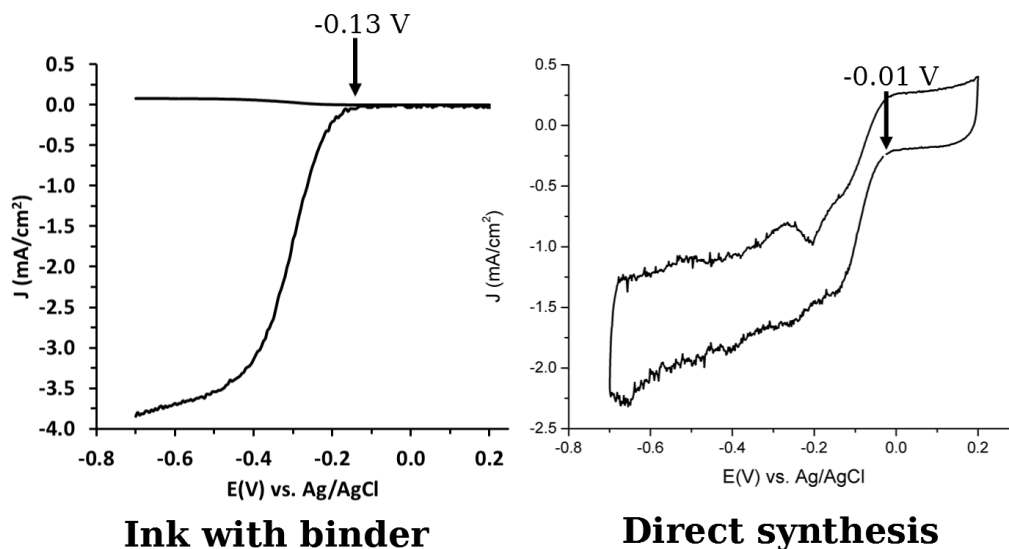
Figure 6.9: Comparison of ORR performance by preparing conventional ink preparation (Left) vs. direct growth and synthesis on stainless steel (Right). Test conducted with the same Cu-N-CNFs sample.

6.3 Future Work

The possibilities of distinct ORR studies with this stable CNF electrode are vast and only a select few studies were conducted here. In the future, it is of great interest to further dive into the phenomena responsible for the enhanced performance due to the metal co-catalyst. This can be approached by employing surface techniques such as scanning tunneling spectroscopy, which can probe the individual redox center for electrochemical information, or using NEXAFS to understand the surface chemistry. These co-catalysts studies can be enhanced with some density functional theory (DFT) simulations, looking at the electronic properties of the catalyst system synthesized and as means to optimize co-catalysts designs. Usage of more transition metals can be interesting. Here I have shown an averaging effect when combining Cu and Fe, but the possibility of synergetic effects occurring from the blend of two different metals is easy to imagine. Serov *et. al.* have demonstrated that the bi-metallic catalysts do not always result in an averaging effect, represented in their Fe-Ni and Fe-Mn catalysts system results.[226]

Another section to focus in the future is to utilize other polymer sources to dope nitrogen, boron, silicon, or phosphorous onto CNFs. The study of different heteroatoms on ORR can be beneficial in building a library of ORR catalysts, and with the reproducibility and stability of this CNF electrode, it is possible to accomplish such goal. Lastly, to make all these catalysts system applicable, we need to be able to integrate them it into a functional fuel cell stack. In order to do this, we will need to explore different porous substrates that permit the flow of ions while still allowing the direct growth of CNFs. Stainless steel TEM grids can be a stating candidate. Alternatively, a redesigning the fuel cell stack assembly may allow the catalyst system to be used as-is or free-standing. When accomplished, the system can undergo polarization curve testing to elucidate the expected real-life performance, and lead to the commercialization of NPMC fuel cells.

6.4   Conclusion

To conclude, I developed an approach to coat CNFs with nitrogen-doped carbons for the efficient reduction of oxygen. I showed that the diazonium method to electrodeposit polyacrylamide results in better control of produced nitrogen species once pyrolyzed. The benefit of Cu as co-catalysts for ORR performance was demonstrated. Due to the stable morphology of the CNF system we showed that Cu co-catalysts is electrochemically active in ORR. As a finishing remark I demonstrated the benefits of utilizing direct growth for ORR.

It is with confidence that we have engineered a reliable electrode useful in many renewable energy applications. It is my hope that this investigation and efforts can serve as the springboard to a plethora of studies and applications for the advancement of science and the restoration of our environment.

⌣ Fin ∼

Bibliography

[1] Rupesh S. Devan, Ranjit A. Patil, Jin-Han Lin, and Yuan-Ron Ma. One-Dimensional Metal-Oxide Nanostructures: Recent Developments in Synthesis, Characterization, and Applications. *Advanced Functional Materials*, 22(16):3326–3370, August 2012.

[2] X. Yang, A. Wolcott, G. Wang, A. Sobo, R.C. Fitzmorris, F. Qian, J.Z. Zhang, and Y. Li. Nitrogen-doped ZnO nanowire arrays for photoelectrochemical water splitting. *Nano Letters*, 9(6):2331–2336, 2009.

[3] Zhong Lin Wang. Piezopotential gated nanowire devices: Piezotronics and piezo-phototronics. *Nano Today*, 5(6):540–552, December 2010.

[4] Allon I. Hochbaum and Peidong Yang. Semiconductor nanowires for energy conversion. *Chemical reviews*, 110(1):527–46, January 2010.

[5] Y. Xia, P. Yang, Y. Sun, Y. Wu, B. Mayers, B. Gates, Y. Yin, F. Kim, and H. Yan. One-Dimensional Nanostructures: Synthesis, Characterization, and Applications. *Advanced Materials*, 15(5):353–389, March 2003.

[6] Candace K. Chan, Hailin Peng, Gao Liu, Kevin McIlwrath, Xiao Feng Zhang, Robert A. Huggins, and Yi Cui. High-performance lithium battery anodes using silicon nanowires. *Nature Nanotechnology*, 3(1):31–5, January 2008.

[7] H. T. Wang, B. S. Kang, F. Ren, L. C. Tien, P. W. Sadik, D. P. Norton, S. J. Pearton, and Jenshan Lin. Hydrogen-selective sensing at room temperature with ZnO nanorods. *Applied Physics Letters*, 86(24):243503, 2005.

[8] L. Liao, H.B. Lu, J.C. Li, H. He, D.F. Wang, D.J. Fu, C. Liu, and W.F. Zhang. Size Dependence of Gas Sensitivity of ZnO Nanorods. *Journal of Physical Chemistry C*, 111(5):1900–1903, February 2007.

[9] M.H. Huang, S. Mao, H. Feick, H .and Yan, Y. Wu, H. Kind, E. Weber, R. Russo, and P. Yang. Room-temperature ultraviolet nanowire nanolasers. *Science (New York, N.Y.)*, 292(5523):1897–9, June 2001.

[10] Sheng Chu, Guoping Wang, Weihang Zhou, Yuqing Lin, Leonid Chernyak, Jianze Zhao, Jieying Kong, Lin Li, Jingjian Ren, and Jianlin Liu. Electrically pumped waveguide lasing from ZnO nanowires. *Nature nanotechnology*, 6(8):506–510, August 2011.

[11] Hao Yan, Hwan Sung Choe, Sung Woo Nam, Yongjie Hu, Shamik Das, James F. Klemic, James C. Ellenbogen, and Charles M. Lieber. Programmable nanowire circuits for nanoprocessors. *Nature*, 470(7333):240–4, February 2011.

[12] Sumio Iijima. Helical microtubules of graphitic carbon. *Nature*, 354(6348):56–58, November 1991.

[13] M. H. MH Huang, Y. Wu, H. Feick, N. Tran, E. Weber, and P. Yang. Catalytic Growth of Zinc Oxide Nanowires by Vapor Transport. *Advanced Materials*, 13(2):113–116, January 2001.

[14] Lori E. Greene, Matt Law, Dawud H. Tan, Max Montano, Josh Goldberger, Gabor Somorjai, and Peidong Yang. General route to vertical ZnO nanowire arrays using textured ZnO seeds. *Nano Letters*, 5(7):1231–6, July 2005.

[15] Yi Cui, Lincoln J. Lauhon, Mark S. Gudiksen, Jianfang Wang, and Charles M. Lieber. Diameter-controlled synthesis of single-crystal silicon nanowires. *Applied Physics Letters*, 78(15):2214, 2001.

[16] Alan M. Cassell, Jeffrey a. Raymakers, Jing Kong, and Hongjie Dai. Large Scale CVD Synthesis of Single-Walled Carbon Nanotubes. *The Journal of Physical Chemistry B*, 103(31):6484–6492, August 1999.

[17] Z.F. Ren. Synthesis of Large Arrays of Well-Aligned Carbon Nanotubes on Glass. *Science*, 282(5391):1105–1107, November 1998.

[18] A.Z. Moshfegh. Nanoparticle catalysts. *Journal of Physics D: Applied Physics*, 42(23):233001, December 2009.

[19] Jennifer Q. Lu, David a Rider, Emanuel Onyegam, Hai Wang, Mitchell a Winnik, Ian Manners, Qian Cheng, Qiang Fu, and Jie Liu. Carbon nanotubes with small and tunable diameters from poly(ferrocenylsilane)-block-polysiloxane diblock copolymers. *Langmuir : the ACS journal of surfaces and colloids*, 22(11):5174–9, May 2006.

[20] Guofang Zhong, Jamie H Warner, Martin Fouquet, Alex W Robertson, Bingan Chen, and John Robertson. Growth of ultrahigh density single-walled carbon nanotube forests by improved catalyst design. *ACS nano*, 6(4):2893–903, April 2012.

[21] S.Y. Li, C.Y. Lee, and T.Y. Tseng. Copper-catalyzed ZnO nanowires on silicon (100) grown by vapor-liquid-solid process. *Journal of Crystal Growth*, 247(3-4):357–362, January 2003.

[22] Yewu Wang, Volker Schmidt, Stephan Senz, and Ulrich Gösele. Epitaxial growth of silicon nanowires using an aluminium catalyst. *Nature nanotechnology*, 1(3):186–9, December 2006.

[23] Jiangtao Hu, Teri Wang Odom, and Charles M. Lieber. Chemistry and Physics in One Dimension: Synthesis and Properties of Nanowires and Nanotubes. *Accounts of Chemical Research*, 32(5):435–445, May 1999.

[24] N. Wang, Y. Cai, and R.Q. Zhang. Growth of nanowires. *Materials Science and Engineering: R: Reports*, 60(1):1–51, 2008.

[25] Hyun D. Park, Anne-Claire Gaillot, S.M. Prokes, and Robert C. Cammarata. Observation of size dependent liquidus depression in the growth of InAs nanowires. *Journal of Crystal Growth*, 296(2):159–164, November 2006.

[26] Brent A. Wacaser, Kimberly A. Dick, Jonas Johansson, Magnus T. Borgström, Knut Deppert, and Lars Samuelson. Preferential Interface Nucleation: An Expansion of the VLS Growth Mechanism for Nanowires. *Advanced Materials*, 21(2):153–165, January 2009.

[27] Yiying Wu and Peidong Yang. Direct Observation of Vapor-Liquid-Solid Nanowire Growth. *Journal of the American Chemical Society*, 123(22):3165–3166, 2001.

[28] C. Klingshirn. ZnO: material, physics and applications. *Chemphyschem : a European journal of chemical physics and physical chemistry*, 8(6):782–803, April 2007.

[29] Zhong Lin Wang. Zinc oxide nanostructures: growth, properties and applications. *Journal of Physics: Condensed Matter*, 16(25):R829–R858, June 2004.

[30] L. Schmidt-Mende. ZnO - nanostructures, defects, and devices. *Materials Today*, 10(5):40–48, 2007.

[31] U. Ozgur, Daniel Hofstetter, and H. Morkoc. ZnO devices and applications: a review of current status and future prospects. *Proceedings of the IEEE*, 2010.

[32] Hao Jiang, Pooi See Lee, and Chunzhong Li. 3D carbon based nanostructures for advanced supercapacitors. *Energy Environ. Sci.*, 6(1):41, December 2013.

[33] Shun Mao, Ganhua Lu, and Junhong Chen. Three-dimensional graphene-based composites for energy applications. *Nanoscale*, 7(16):6924–6943, December 2015.

[34] Zhi Li, Zhanwei Xu, Huanlei Wang, Jia Ding, Beniamin Zahiri, Chris M. B. Holt, Xuehai Tan, and David Mitlin. Colossal pseudocapacitance in a high functionality–high surface area carbon anode doubles the energy of an asymmetric supercapacitor. *Energy Environ. Sci.*, 7(5):1708, April 2014.

[35] Yunyong Li, Zesheng Li, and Pei Kang Shen. Simultaneous formation of ultrahigh surface area and three-dimensional hierarchical porous graphene-like networks for fast and highly stable supercapacitors. *Adv. Mater.*, 25(17):2474–80, May 2013.

[36] Xi Wang, Qunhong Weng, Xizheng Liu, Xuebin Wang, Dai Ming Tang, Wei Tian, Chao Zhang, Wei Yi, Dequan Liu, Yoshio Bando, and Dmitri Golberg. Atomistic origins of high rate capability and capacity of N-doped graphene for lithium storage. *Nano Lett.*, 14(3):1164–1171, January 2014.

[37] Wei Liu, Mingliang Wang, Chunxiang Xu, Shifu Chen, and Xianliang Fu. Significantly enhanced visible-light photocatalytic activity of g-C3N4 via ZnO modification and the mechanism study. *Journal of Molecular Catalysis A: Chemical*, 368-369:9–15, March 2013.

[38] Yanguang Li, Wu Zhou, Hailiang Wang, Liming Xie, Yongye Liang, Fei Wei, Juan-Carlos Idrobo, Stephen J. Pennycook, and Hongjie Dai. An oxygen reduction electrocatalyst based on carbon nanotube-graphene complexes. *Nat. Nanotechnol.*, 7(6):394–400, June 2012.

[39] Zhi Yang, Huagui Nie, Xi'an Chen, Xiaohua Chen, and Shaoming Huang. Recent progress in doped carbon nanomaterials as effective cathode catalysts for fuel cell oxygen reduction reaction. *J. Power Sources*, 236:238–249, August 2013.

[40] Hyeon Suk Shin, Jung Inn Sohn, Dong Chung Kim, Wilhelm T.S. Huck, Mark E. Welland, Hee Cheul Choi, and Dae Joon Kang. Density control of ZnO nanowires grown using Au-PMMA nanoparticles and their growth behavior. *Nanotechnology*, 20(8):085601, February 2009.

[41] Guang Zhu, Yusheng Zhou, Sihong Wang, Rusen Yang, Yong Ding, Xue Wang, Yoshio Bando, and Zhong Lin Wang. Synthesis of vertically aligned ultra-long ZnO nanowires on heterogeneous substrates with catalyst at the root. *Nanotechnology*, 23(5):055604, February 2012.

[42] Tam Ngo-Duc, Karandeep Singh, M. Meyyappan, and Michael M. Oye. Vertical ZnO nanowire growth on metal substrates. *Nanotechnology*, 23(19):194015, May 2012.

[43] Dong-Hau Kuo, Jian-Fong Fang, R.S. Chen, C.A. Chen, and Y.S. Huang. ZnO Nanomaterials Grown with Fe-Based Catalysts. *The Journal of Physical Chemistry C*, 115(25):12260–12268, 2011.

[44] G.Z. Xing, X.S. Fang, Z. Zhang, D.D. Wang, X. Huang, J. Guo, L. Liao, Z. Zheng, H.R. Xu, T. Yu, Z.X. Shen, C.H.A Huan, T.C. Sum, H. Zhang, and T. Wu. Ultrathin single-crystal ZnO nanobelts: Ag-catalyzed growth and field emission property. *Nanotechnology*, 21(25):255701, June 2010.

[45] Franklin Feng Tao. Synthesis, catalysis, surface chemistry and structure of bimetallic nanocatalysts. *Chemical Society reviews*, 41(24):7977–9, December 2012.

[46] Yiming Li, Woong Kim, Yuegang Zhang, Marco Rolandi, Dunwei Wang, and Hongjie Dai. Growth of Single-Walled Carbon Nanotubes from Discrete Catalytic Nanoparticles of Various Sizes. *The Journal of Physical Chemistry B*, 105(46):11424–11431, November 2001.

[47] A.M. Morales. A Laser Ablation Method for the Synthesis of Crystalline Semiconductor Nanowires. *Science*, 279(5348):208–211, January 1998.

[48] Jianye Li, Qi Zhang, Hongying Peng, Henry O. Everitt, Luchang Qin, Jie Liu, and North Carolina. Diameter-Controlled Vapor-Solid Epitaxial Growth and Properties of Aligned ZnO Nanowire Arrays. *The Journal of Physical Chemistry C*, 113(10):3950–3954, 2009.

[49] Lance Delzeit, Bin Chen, Alan Cassell, and Ramsey Stevens. Multilayered metal catalysts for controlling the density of single-walled carbon nanotube growth. *Chemical Physics Letters*, 348(November):368–374, 2001.

[50] Yiying Wu, Rong Fan, and Peidong Yang. Block-by-Block Growth of Single-Crystalline Si/SiGe Superlattice Nanowires. *Nano Letters*, 2(2):83–86, February 2002.

[51] Xianying Wang, Shufang Xie, Jian Liu, Sergei O. Kucheyev, and Y. Morris Wang. Focused-ion-beam Assisted Growth, Patterning, and Narrowing the Size Distributions of ZnO Nanowires for Variable Optical Properties and Enhanced Nonmechanical Energy Conversion. *Chemistry of Materials*, 25(14):2819–2827, July 2013.

[52] C. Li, G. Fang, J. Li, L. Ai, B. Dong, and X. Zhao. Effect of Seed Layer on Structural Properties of ZnO Nanorod Arrays Grown by Vapor-Phase Transport. *Journal of Physical Chemistry C*, 112(4):990–995, January 2008.

[53] Jaejin Song and Sangwoo Lim. Effect of Seed Layer on the Growth of ZnO Nanorods. *The Journal of Physical Chemistry C*, 111(2):596–600, January 2007.

[54] Wonseok Hwang, Ji-Hyuk Choi, Tae Hee Kim, Jinwoo Sung, Jae-Min Myoung, Dae-Geun Choi, Byeong-Hyeok Sohn, Sang Soo Lee, Dong Ha Kim, and Cheolmin Park. Control of the Area Density of Vertically Grown ZnO Nanowires by Blending PS- b -P4VP and PS- b -PAA Copolymer Micelles. *Chemistry of Materials*, 20(19):6041–6047, October 2008.

[55] R.D. Bennett, A.J. Hart, and R.E. Cohen. Controlling the Morphology of Carbon Nanotube Films by Varying the Areal Density of Catalyst Nanoclusters Using Block-Copolymer Micellar Thin Films. *Advanced Materials*, 18(17):2274–2279, September 2006.

[56] By Gerd Kästle, Hans-gerd Boyen, Frank Weigl, Gunther Lengl, Thomas Herzog, Paul Ziemann, Silke Riethmüller, Oliver Mayer, Christoph Hartmann, Joachim P. Spatz, Martin Möller, Masaki Ozawa, Florian Banhart, Michael G. Garnier, and Peter Oelhafen. Micellar Nanoreactors-Preparation and Characterization of Hexagonally Ordered Arrays of Metallic Nanodots. *Advanced Functional Materials*, 11(11):853–861, November 2003.

[57] Jennifer Q. Lu and Sung Soo Yi. Uniformly sized gold nanoparticles derived from PS-b-P2VP block copolymer templates for the controllable synthesis of Si nanowires. *Langmuir : the ACS journal of surfaces and colloids*, 22(9):3951–4, April 2006.

[58] Yang Liu, Chai Lor, Qiang Fu, David Pan, Lei Ding, Jie Liu, and Jennifer Lu. Synthesis of Copper Nanocatalysts with Tunable Size Using Diblock Copolymer Solution Micelles. *The Journal of Physical Chemistry C*, 114(13):5767–5772, April 2010.

[59] Jennifer Q. Lu. Nanocatalysts with Tunable Properties Derived from Polystyrene-b-poly(vinyl pyridine) Block Copolymer Templates for Achieving Controllable Carbon Nanotube Synthesis. *Journal of Physical Chemistry C*, 112(28):10344–10351, July 2008.

[60] Jennifer Lu, Dongning Yuan, Jie Liu, Weinan Leng, and Thomas E. Kopley. Three dimensional single-walled carbon nanotubes. *Nano letters*, 8(10):3325–9, October 2008.

[61] Daniel Kälblein, R. Thomas Weitz, H. Jens Böttcher, Frederik Ante, Ute Zschieschang, Klaus Kern, and Hagen Klauk. Top-gate ZnO nanowire transistors and integrated circuits with ultrathin self-assembled monolayer gate dielectric. *Nano Letters*, 11(12):5309–15, December 2011.

[62] Guang Zhu, Rusen Yang, Sihong Wang, and Zhong Lin Wang. Flexible high-output nanogenerator based on lateral ZnO nanowire array. *Nano letters*, 10(8):3151–5, August 2010.

[63] Chandra Sekhar Rout, S. Hari Krishna, S.R.C. Vivekchand, a. Govindaraj, and C.N.R. Rao. Hydrogen and ethanol sensors based on ZnO nanorods, nanowires and nanotubes. *Chemical Physics Letters*, 418(4-6):586–590, February 2006.

[64] C. H. Xu, Z. B. Zhu, G. L. Li, W. R. Xu, and H. X. Huang. Growth of ZnO nanostructure on Cu0.62Zn0.38 brass foils by thermal oxidation. *Materials Chemistry and Physics*, 124(1):252–256, November 2010.

[65] Matt Law, Lori E. Greene, Justin C. Johnson, Richard Saykally, and Peidong Yang. Nanowire dye-sensitized solar cells. *Nature Materials*, 4(6):455–9, June 2005.

[66] Alejandro L. Briseno, Thomas W. Holcombe, Akram I. Boukai, Erik C. Garnett, Steve W. Shelton, Jean J.M. Fréchet, and Peidong Yang. Oligo- and polythiophene/ZnO hybrid nanowire solar cells. *Nano letters*, 10(1):334–340, January 2010.

[67] Jiming Bao, Mariano A. Zimmler, Federico Capasso, Xiaowei Wang, and Z.F. Ren. Broadband ZnO single-nanowire light-emitting diode. *Nano Letters*, 6(8):1719–1722, 2006.

[68] A.B. Djurišić, A.M.C. Ng, and X.Y. Chen. ZnO nanostructures for optoelectronics: Material properties and device applications. *Progress in Quantum Electronics*, 34(4):191–259, July 2010.

[69] C.J. Lee, T.J. Lee, S.C. Lyu, Y. Zhang, H. Ruh, and H.J. Lee. Field emission from well-aligned zinc oxide nanowires grown at low temperature. *Applied Physics Letters*, 81(19):3648, 2002.

[70] N. Pan, H. Xue, M. Yu, X. Cui, and X. Wang. Tip-morphology-dependent field emission from ZnO nanorod arrays. *Nanotechnology*, 21(22):225707, June 2010.

[71] R.S. Wagner and W.C. Ellis. Vapor-liquid-solid mechanism of single crystal growth. *Applied Physics Letters*, 4(5):89–90, 1964.

[72] David A. Evans, David W. C. MacMillan, and Kevin R. Campos. C2-Symmetric Tin(II) Complexes as Chiral Lewis Acids. Catalytic Enantioselective Anti Aldol Additions of Enolsilanes to Glyoxylate and Pyruvate Esters. *Journal of the American Chemical Society*, 119(44):10859–10860, November 1997.

[73] D. Briggs. *Handbook of X-ray and Ultraviolet Photoelectron Spectroscopy*. Heyden & Son, London, 1977.

[74] Wei-Qiao Deng, Xin Xu, and William a. Goddard. A Two-Stage Mechanism of Bimetallic Catalyzed Growth of Single-Walled Carbon Nanotubes. *Nano Letters*, 4(12):2331–2335, December 2004.

[75] Christopher A. Crouse, Benji Maruyama, Ramon Colorado, Tyson Back, and Andrew R. Barron. Growth, new growth, and amplification of carbon nanotubes as a function of catalyst composition. *Journal of the American Chemical Society*, 130(25):7946–54, June 2008.

[76] Stefano Curtarolo, Neha Awasthi, Wahyu Setyawan, Aiqin Jiang, Kim Bolton, Toshio Tokune, and Avetik Harutyunyan. Influence of Mo on the Fe:Mo:C nanocatalyst thermodynamics for single-walled carbon nanotube growth. *Physical Review B*, 78(5):054105, August 2008.

[77] S. Tang, Z. Zhong, Z. Xiong, L. Sun, L. Liu, J. Lin, Z.X. Shen, and K.L. Tan. Controlled growth of single-walled carbon nanotubes by catalytic decomposition of CH4 over Mo/Co/MgO catalysts. *Chemical Physics Letters*, 350(December):19–26, 2001.

[78] B. Kitiyanan, W.E. Alvarez, J.H. Harwell, and D.E. Resasco. Controlled production of single-wall carbon nanotubes by catalytic decomposition of CO on bimetallic Co–Mo catalysts, 2000.

[79] Avetik R. Harutyunyan, Elena Mora, Toshio Tokune, Kim Bolton, Arne Rosén, Aiqin Jiang, Neha Awasthi, and Stefano Curtarolo. Hidden features of the catalyst nanoparticles favorable for single-walled carbon nanotube growth. *Applied Physics Letters*, 90(16):163120, 2007.

[80] Prahalad M. Parthangal, Richard E. Cavicchi, and Michael R. Zachariah. A generic process of growing aligned carbon nanotube arrays on metals and metal alloys. *Nanotechnology*, 18(18):185605, May 2007.

[81] P. Tomasik, Z. Ratajewicz, G.R. Newkome, and L. Strekowski. *The Chemistry of Heterocyclic Compounds, Pyridine Metal Complexes*, volume 14 of *Chemistry of Heterocyclic Compounds: A Series Of Monographs*. John Wiley & Sons, Inc., Hoboken, NJ, USA, January 1985.

[82] Jong Seok Jeong and Jeong Yong Lee. Investigation of initial growth of ZnO nanowires and their growth mechanism. *Nanotechnology*, 21(47):475603, November 2010.

[83] Lena Mazeina, Yoosuf N. Picard, and Sharka M. Prokes. Controlled Growth of Parallel Oriented ZnO Nanostructural Arrays on Ga2O3 Nanowires. *Cryst. Growth Des.*, 9(2):1164–1169, 2009.

[84] F. Fang, D.X. Zhao, J.Y. Zhang, D.Z. Shen, Y.M. Lu, X.W. Fan, B.H. Li, and X.H. Wang. Growth of well-aligned ZnO nanowire arrays on Si substrate. *Nanotechnology*, 18(23):235604, June 2007.

[85] ASM Handbook. Alloy Phase Diagrams, vol. 3. *ASM, Met. Park. OH*, 1992.

[86] Yang Liu, Jose Fernando Flores, and Jennifer Lu. Tailoring 1D ZnO Nanostructure Using Engineered Catalyst Enabled by Poly(4-vinylpyridine). *The Journal of Physical Chemistry C*, 118:19387–19395, July 2014.

[87] Jinhui Yang, Donge Wang, Hongxian Han, and Can Li. Roles of cocatalysts in photocatalysis and photoelectrocatalysis. *Accounts of chemical research*, 46(8):1900–9, August 2013.

[88] Frank E. Osterloh. Inorganic nanostructures for photoelectrochemical and photocatalytic water splitting. *Chemical Society Reviews*, 42(6):2294–320, March 2013.

[89] Xiaobo Chen, Lei Liu, Peter Y. Yu, and Samuel S. Mao. Increasing solar absorption for photocatalysis with black hydrogenated titanium dioxide nanocrystals. *Science (New York, N.Y.)*, 331(6018):746–50, February 2011.

[90] In Sun Cho, Chi Hwan Lee, Yunzhe Feng, Manca Logar, Pratap M. Rao, Lili Cai, Dong Rip Kim, Robert Sinclair, and Xiaolin Zheng. Codoping titanium dioxide nanowires with tungsten and carbon for enhanced photoelectrochemical performance. *Nature communications*, 4:1723, January 2013.

[91] N.S. Lewis. Light work with water. *Nature*, 414(6864):589–90, December 2001.

[92] F. Vietmeyer, B. Seger, and P. V. Kamat. Anchoring ZnO Particles on Functionalized Single Wall Carbon Nanotubes. Excited State Interactions and Charge Collection. *Advanced Materials*, 19(19):2935–2940, October 2007.

[93] Saji Thomas Kochuveedu, Yoon Hee Jang, Yu Jin Jang, and Dong Ha Kim. Visible light active photocatalysis on block copolymer induced strings of ZnO nanoparticles doped with carbon. *Journal of Materials Chemistry A*, 1(3):898–905, 2013.

[94] Xue-wen Wang, Li Zhou, and Feng Li. ZnO disks loaded with reduced graphene oxide for the photodegradation of methylene blue. *New Carbon Materials*, 28(6):408–413, 2013.

[95] Zhang Chen, Nan Zhang, and Yi-Jun Xu. Synthesis of graphene–ZnO nanorod nanocomposites with improved photoactivity and anti-photocorrosion. *CrystEngComm*, 15(15):3022, March 2013.

[96] Yuyu Bu, Zhuoyuan Chen, Weibing Li, and Baorong Hou. Highly efficient photocatalytic performance of graphene-ZnO quasi-shell-core composite material. *ACS applied materials & interfaces*, 5(23):12361–8, December 2013.

[97] Shahed U.M. Khan, Mofareh Al-Shahry, and William B. Ingler. Efficient photochemical water splitting by a chemically modified n-TiO2. *Science (New York, N.Y.)*, 297(5590):2243–5, September 2002.

[98] Xina Wang, Haojun Zhu, Yeming Xu, Hao Wang, Yin Tao, Suikong Hark, Xudong Xiao, and Quan Li. Aligned ZnO/CdTe core-shell nanocable arrays on indium tin oxide: synthesis and photoelectrochemical properties. *ACS nano*, 4(6):3302–8, June 2010.

[99] Miao Zhong, Yanhang Ma, Peter Oleynikov, Kazunari Domen, and Jean-Jacques Delaunay. A conductive ZnO–ZnGaON nanowire-array-on-a-film photoanode for stable and efficient sunlight water splitting. *Energy Environ. Sci.*, 7(5):1693, March 2014.

[100] José Ramón Durán Retamal, Cheng-Ying Chen, Der-Hsien Lien, Michael R.S. Huang, Chin-An Lin, Chuan-Pu Liu, and Jr-Hau He. Concurrent Improvement in Photogain and Speed of a Metal Oxide Nanowire Photodetector through Enhancing Surface Band Bending via Incorporating a Nanoscale Heterojunction. *ACS Photonics*, 1(4):354–359, March 2014.

[101] Mahmud Diab and Taleb Mokari. Thermal decomposition approach for the formation of α-Fe2O3 mesoporous photoanodes and an α-Fe2O3/CoO hybrid structure for enhanced water oxidation. *Inorg. Chem.*, 53(4):2304–9, January 2014.

[102] Chengquan Zhu, Bingan Lu, Qing Su, Erqing Xie, and Wei Lan. A simple method for the preparation of hollow ZnO nanospheres for use as a high performance photocatalyst. *Nanoscale*, 4(10):3060–4, May 2012.

[103] Ke Sun, Yi Jing, Chun Li, Xiaofeng Zhang, Ryan Aguinaldo, Alireza Kargar, Kristian Madsen, Khaleda Banu, Yuchun Zhou, Yoshio Bando, Zhaowei Liu, and Deli Wang. 3D branched nanowire heterojunction photoelectrodes for high-efficiency solar water splitting and H2 generation. *Nanoscale*, 4(5):1515–21, March 2012.

[104] Chenzhong Yao, Bohui Wei, Huixuan Ma, Hui Li, Lixin Meng, Xisheng Zhang, and Qiaojuan Gong. Enhanced photoelectrochemical performance of hydrogenated ZnO hierarchical nanorod arrays. *Journal of Power Sources*, 237:295–299, September 2013.

[105] Alireza Kargar, Yi Jing, Sung Joo Kim, Conor T. Riley, Xiaoqing Pan, and Deli Wang. ZnO/CuO heterojunction branched nanowires for photoelectrochemical hydrogen generation. *ACS nano*, 7(12):11112–20, December 2013.

[106] Yongcai Qiu, Keyou Yan, Hong Deng, and Shihe Yang. Secondary branching and nitrogen doping of ZnO nanotetrapods: building a highly active network for photoelectrochemical water splitting. *Nano letters*, 12(1):407–13, January 2012.

[107] Yantao Shi, Kai Wang, Yi Du, Hong Zhang, Junfu Gu, Chao Zhu, Lin Wang, Wei Guo, Anders Hagfeldt, Ning Wang, and Tingli Ma. Solid-state synthesis of ZnO nanostructures for quasi-solid dye-sensitized solar cells with high efficiencies up to 6.46%. *Advanced materials (Deerfield Beach, Fla.)*, 25(32):4413–9, August 2013.

[108] Feng Xu and Litao Sun. Solution-derived ZnO nanostructures for photoanodes of dye-sensitized solar cells. *Energy & Environmental Science*, 4(3):818, March 2011.

[109] Xiaonan Wen, Wenzhuo Wu, Yong Ding, and Zhong Lin Wang. Seedless synthesis of patterned ZnO nanowire arrays on metal thin films (Au, Ag, Cu, Sn) and their application for flexible electromechanical sensing. *Journal of Materials Chemistry*, 22(19):9469, 2012.

[110] Zhuo Wang, Xue-feng Qian, Jie Yin, and Zi-kang Zhu. Large-Scale Fabrication of Tower-like, Flower-like, and Tube-like ZnO Arrays by a Simple Chemical Solution Route. *Langmuir*, 20(8):3441–3448, April 2004.

[111] Lori E. Greene, Benjamin D. Yuhas, Matt Law, David Zitoun, and Peidong Yang. Solution-grown zinc oxide nanowires. *Inorganic Chemistry*, 45(19):7535–43, September 2006.

[112] Hongchao Ma, Lixia Yue, Chunling Yu, Xiaoli Dong, Xiufang Xinxin Zhang, Mang Xue, and Yinghuan Fu. Synthesis, characterization and photocatalytic activity of Cu-doped Zn/ZnO photocatalyst with carbon modification. *Journal of Materials Chemistry*, 22(45):23780, October 2012.

[113] M. Ahmad, E. Ahmed, Z.L. Hong, J.F. Xu, N.R. Khalid, A. Elhissi, and W. Ahmed. A facile one-step approach to synthesizing ZnO/graphene composites for enhanced degradation of methylene blue under visible light. *Applied Surface Science*, 274:273–281, 2013.

[114] M. Willander, O. Nur, Q.X. Zhao, L.L. Yang, M. Lorenz, B.Q. Cao, J. Zúñiga Pérez, C. Czekalla, G. Zimmermann, M. Grundmann, A. Bakin, A. Behrends, M. Al-Suleiman, A. El-Shaer, A. Che Mofor, B. Postels,

A. Waag, N. Boukos, A. Travlos, H.S. Kwack, J. Guinard, and D. Le Si Dang. Zinc oxide nanorod based photonic devices: recent progress in growth, light emitting diodes and lasers. *Nanotechnology*, 20(33):332001, August 2009.

[115] Seung Hwan Ko, Daeho Lee, Hyun Wook Kang, Koo Hyun Nam, Joon Yeob Yeo, Suk Joon Hong, Costas P. Grigoropoulos, and Hyung Jin Sung. Nanoforest of hydrothermally grown hierarchical ZnO nanowires for a high efficiency dye-sensitized solar cell. *Nano Letters*, 11(2):666–671, 2011.

[116] Jong G. Ok, Sameh H. Tawfick, K. Anne Juggernauth, Kai Sun, Yongyi Zhang, and A. John Hart. Electrically Addressable Hybrid Architectures of Zinc Oxide Nanowires Grown on Aligned Carbon Nanotubes. *Advanced Functional Materials*, 20(15):2470–2480, June 2010.

[117] Manoj Raula, Md. Harunar Rashid, Tapas K. Paira, Enakshi Dinda, and Tarun K. Mandal. Ascorbate-assisted growth of hierarchical ZnO nanostructures: sphere, spindle, and flower and their catalytic properties. *Langmuir : the ACS journal of surfaces and colloids*, 26(11):8769–82, June 2010.

[118] Shingo Hirano, Nobuo Takeuchi, Shu Shimada, Kyosuke Masuya, Katsuhiko Ibe, Hideo Tsunakawa, and Makoto Kuwabara. Room-temperature nanowire ultraviolet lasers: An aqueous pathway for zinc oxide nanowires with low defect density. *Journal of Applied Physics*, 98(9):094305, November 2005.

[119] T.Y. Kim, S.H. Lee, K.S. Nahm, J.Y. Kim, H.W. Shim, and E.K. Suh. Catalytic growth and characterization of ZnO nano-needles. In *2003 Third IEEE Conference on Nanotechnology, 2003. IEEE-NANO 2003.*, volume 2, pages 823–827. IEEE, 2003.

[120] Fu-Hsuan Chu, Chun-Wei Huang, Cheng-Lun Hsin, Chun-Wen Wang, Shih-Ying Yu, Ping-Hung Yeh, and Wen-Wei Wu. Well-aligned ZnO nanowires with excellent field emission and photocatalytic properties. *Nanoscale*, 4(5):1471, 2012.

[121] Yongye Liang, Yanguang Li, Hailiang Wang, and Hongjie Dai. Strongly coupled inorganic/nanocarbon hybrid materials for advanced electrocatalysis. *Journal of the American Chemical Society*, 135(6):2013–36, February 2013.

[122] Roel van de Krol and Michael Grätzel, editors. *Photoelectrochemical Hydrogen Production*, volume 102 of *Electronic Materials: Science & Technology*. Springer US, Boston, MA, 2012.

[123] Toshiyuki Momma, Xingjiang Liu, Tetsuya Osaka, Yousuke Ushio, and Yoshimitsu Sawada. Electrochemical modification of active carbon fiber electrode and its application to double-layer capacitor. *J. Power Sources*, 60(2):249–253, June 1996.

[124] E. Frackowiak, K. Metenier, V. Bertagna, and F. Beguin. Supercapacitor electrodes from multiwalled carbon nanotubes. *Appl. Phys. Lett.*, 77(15):2421, October 2000.

[125] Dingshan Yu, Kunli Goh, Hong Wang, Li Wei, Wenchao Jiang, Qiang Zhang, Liming Dai, and Yuan Chen. Scalable synthesis of hierarchically structured carbon nanotube-graphene fibres for capacitive energy storage. *Nat. Nanotechnol.*, 9(7):555–62, July 2014.

[126] Martin Winter and Ralph J. Brodd. What are batteries, fuel cells, and supercapacitors? *Chem. Rev.*, 104(10):4245–69, October 2004.

[127] Uday Narayan Maiti, Won Jun Lee, Ju Min Lee, Youngtak Oh, Ju Young Kim, Ji Eun Kim, Jongwon Shim, Tae Hee Han, and Sang Ouk Kim. 25th anniversary article: Chemically modified/doped carbon nanotubes & graphene for optimized nanostructures & nanodevices. *Adv. Mater.*, 26(1):40–66, January 2014.

[128] Patrice Simon and Yury Gogotsi. Materials for electrochemical capacitors. *Nat. Mater.*, 7(11):845–54, November 2008.

[129] Yunhui Zhao, Mingxian Liu, Lihua Gan, Xiaomei Ma, Dazhang Zhu, Zijie Xu, and Longwu Chen. Ultramicroporous Carbon Nanoparticles for the High-Performance Electrical Double-Layer Capacitor Electrode. *Energy & Fuels*, 28(2):1561–1568, February 2014.

[130] Zhi Li, Zhanwei Xu, Xuehai Tan, Huanlei Wang, Chris M. B. Holt, Tyler Stephenson, Brian C. Olsen, and David Mitlin. Mesoporous nitrogen-rich carbons derived from protein for ultra-high capacity battery anodes and supercapacitors. *Energy Environ. Sci.*, 6(3):871, 2013.

[131] Jilei Liu, Lili Zhang, Hao Bin Wu, Jianyi Lin, Zexiang Shen, and Xiong Wen (David) Lou. High-performance flexible asymmetric supercapacitors based on a new graphene foam/carbon nanotube hybrid film. *Energy Environ. Sci.*, 7(11):3709–3719, August 2014.

[132] Grzegorz Milczarek and Olle Inganäs. Renewable cathode materials from biopolymer/conjugated polymer interpenetrating networks. *Science*, 335(6075):1468–71, March 2012.

[133] Zheng Yan, Lulu Ma, Yu Zhu, Indranil Lahiri, Myung Gwan Hahm, Zheng Liu, Shubin Yang, Changsheng Xiang, Wei Lu, Zhiwei Peng, Zhengzong Sun, Carter Kittrell, Jun Lou, Wonbong Choi, Pulickel M. Ajayan, and James M. Tour. Three-dimensional metal-graphene-nanotube multifunctional hybrid materials. *ACS Nano*, 7(1):58–64, January 2013.

[134] Radu Reit, Justin Nguyen, and W. Jud Ready. Growth time performance dependence of vertically aligned carbon nanotube supercapacitors grown on aluminum substrates. *Electrochim. Acta*, 91:96–100, February 2013.

[135] Reza Kavian, Antonello Vicenzo, and Massimiliano Bestetti. Growth of carbon nanotubes on aluminium foil for supercapacitors electrodes. *J. Mater. Sci.*, 46(5):1487–1493, October 2010.

[136] Mazdak Hashempour, Antonello Vicenzo, Fu Zhao, and Massimiliano Bestetti. Effects of CVD direct growth of carbon nanotubes and nanofibers on microstructure and electrochemical corrosion behavior of 316 stainless steel. *Mater. Charact.*, 92:64–76, June 2014.

[137] S. Talapatra, S. Kar, S.K. Pal, R. Vajtai, L. Ci, P. Victor, M.M. Shaijumon, S. Kaur, O. Nalamasu, and P.M. Ajayan. Direct growth of aligned carbon nanotubes on bulk metals. *Nature Nanotechnology*, 1(2):112–6, November 2006.

[138] Yingwen Cheng, Songtao Lu, Hongbo Zhang, Chakrapani V. Varanasi, and Jie Liu. Synergistic effects from graphene and carbon nanotubes enable flexible and robust electrodes for high-performance supercapacitors. *Nano Lett.*, 12(8):4206–11, August 2012.

[139] Chun Xian Guo and Chang Ming Li. A self-assembled hierarchical nanostructure comprising carbon spheres and graphene nanosheets for enhanced supercapacitor performance. *Energy Environ. Sci.*, 4(11):4504, October 2011.

[140] Qian Wang, Jun Yan, Yanbo Wang, Tong Wei, Milin Zhang, Xiaoyan Jing, and Zhuangjun Fan. Three-dimensional flower-like and hierarchical porous carbon materials as high-rate performance electrodes for supercapacitors. *Carbon N. Y.*, 67:119–127, February 2014.

[141] Nam Dong Kim, D. Bruce Buchholz, Gilberto Casillas, Miguel José-Yacaman, and Robert P. H. Chang. Hierarchical Design for Fabricating Cost-Effective High Performance Supercapacitors. *Adv. Funct. Mater.*, 24(26):4186–4194, July 2014.

[142] Shiping Wang, Chuanlong Han, Jing Wang, Jiang Deng, Minglei Zhu, Jia Yao, Haoran Li, and Yong Wang. Controlled Synthesis of Ordered Mesoporous Carbohydrate-Derived Carbons with Flower-like Structure and N-Doping by Self-Transformation. *Chem. Mater.*, 26(23):6872–6877, December 2014.

[143] R. Baker. Nucleation and growth of carbon deposits from the nickel catalyzed decomposition of acetylene. *Journal of Catalysis*, 26(1):51–62, July 1972.

[144] L.S. Lobo, J.L. Figueiredo, and C.A. Bernardo. Carbon formation and gasification on metals. Bulk diffusion mechanism: A reassessment. *Catal. Today*, 178(1):110–116, December 2011.

[145] Y. Nishiyama. Carbon formation on copper-nickel alloys from benzene. *Journal of Catalysis*, 33(1):98–107, April 1974.

[146] Jennifer Lu, Sung Soo Yi, Thomas Kopley, Cheng Qian, Jie Liu, and Erdogan Gulari. Fabrication of ordered catalytically active nanoparticles derived from block copolymer micelle templates for controllable synthesis of single-walled carbon nanotubes. *J. Phys. Chem. B*, 110(13):6655–60, April 2006.

[147] I. Alstrup. A new model explaining carbon filament growth on nickel, iron, and Ni–Cu alloy catalysts. *Journal of Catalysis*, 109(2):241–251, February 1988.

[148] Yoshikazu Ito, Christos Christodoulou, Marco Vittorio Nardi, Norbert Koch, Hermann Sachdev, and Klaus Müllen. Chemical vapor deposition of N-doped graphene and carbon films: the role of precursors and gas phase. *ACS Nano*, 8(4):3337–46, April 2014.

[149] A.C. Dillon, T. Gennett, K.M. Jones, J.L. Alleman, P.A. Parilla, and M.J. Heben. A Simple and Complete Purification of Single-Walled Carbon Nanotube Materials. *Adv. Mater.*, 11(16):1354–1358, November 1999.

[150] Hyeon Gu Cho, Sang Won Kim, Hyeong Jun Lim, Chang Hoon Yun, Heon Sang Lee, and Chong Rae Park. A simple and highly effective process for the purification of single-walled carbon nanotubes synthesized with arc-discharge. *Carbon N. Y.*, 47(15):3544–3549, December 2009.

[151] Tak Jeong, Wan-Young Kim, and Yoon-Bong Hahn. A new purification method of single-wall carbon nanotubes using H2S and O2 mixture gas. *Chem. Phys. Lett.*, 344(1-2):18–22, August 2001.

[152] Kenji Hata, Don N Futaba, Kohei Mizuno, Tatsunori Namai, Motoo Yumura, and Sumio Iijima. Water-assisted highly efficient synthesis of impurity-free single-walled carbon nanotubes. *Science*, 306(5700):1362–4, November 2004.

[153] Kuanping Gong, Feng Du, Zhenhai Xia, Michael Durstock, and Liming Dai. Nitrogen-doped carbon nanotube arrays with high electrocatalytic activity for oxygen reduction. *Science*, 323(5915):760–4, March 2009.

[154] Jing Gao, Jun Zhong, Lili Bai, Jinyin Liu, Guanqi Zhao, and Xuhui Sun. Revealing the role of catalysts in carbon nanotubes and nanofibers by scanning transmission X-ray microscopy. *Sci. Rep.*, 4:3606, January 2014.

[155] Hidetaka Konno, Teruhiko Ito, Mariko Ushiro, Koji Fushimi, and Kazuhisa Azumi. High capacitance B/C/N composites for capacitor electrodes synthesized by a simple method. *J. Power Sources*, 195(6):1739–1746, March 2010.

[156] Li Zhao, Li-Zhen Fan, Meng-Qi Zhou, Hui Guan, Suyan Qiao, Markus Antonietti, and Maria-Magdalena Titirici. Nitrogen-containing hydrothermal carbons with superior performance in supercapacitors. *Adv. Mater.*, 22(45):5202–6, December 2010.

[157] Jing Wei, Dandan Zhou, Zhenkun Sun, Yonghui Deng, Yongyao Xia, and Dongyuan Zhao. A Controllable Synthesis of Rich Nitrogen-Doped Ordered Mesoporous Carbon for CO2 Capture and Supercapacitors. *Adv. Funct. Mater.*, 23(18):2322–2328, May 2013.

[158] Michio Inagaki, Hidetaka Konno, and Osamu Tanaike. Carbon materials for electrochemical capacitors. *J. Power Sources*, 195(24):7880–7903, December 2010.

[159] Kun Yang, Liangbo Peng, Dong Shu, Cuijuan Lv, Chun He, and Lu Long. Capacitive performance of a heteroatom-enriched activated carbon inconcentrated sulfuric acid. *J. Power Sources*, 239:553–560, October 2013.

[160] Jinpeng Han, Guiyin Xu, Bing Ding, Jin Pan, Hui Dou, and Douglas R. MacFarlane. Porous nitrogen-doped hollow carbon spheres derived from polyaniline for high performance supercapacitors. *J. Mater. Chem. A*, 2(15):5352, March 2014.

[161] Dhanya Puthusseri, Vanchiappan Aravindan, Srinivasan Madhavi, and Satishchandra Ogale. 3D micro-porous conducting carbon beehive by single step polymer carbonization for high performance supercapacitors: the magic of in situ porogen formation. *Energy Environ. Sci.*, 7(2):728, January 2014.

[162] Hyung Mo Jeong, Jung Woo Lee, Weon Ho Shin, Yoon Jeong Choi, Hyun Joon Shin, Jeung Ku Kang, and Jang Wook Choi. Nitrogen-doped graphene for high-performance ultracapacitors and the importance of nitrogen-doped sites at basal planes. *Nano Lett.*, 11(6):2472–7, June 2011.

[163] Young Soo Yun, Changbin Im, Hyun Ho Park, Imgon Hwang, Yongsug Tak, and Hyoung-Joon Jin. Hierarchically porous carbon nanofibers containing numerous heteroatoms forsupercapacitors. *J. Power Sources*, 234:285–291, July 2013.

[164] Zhenhai Wen, Xinchen Wang, Shun Mao, Zheng Bo, Haejune Kim, Shumao Cui, Ganhua Lu, Xinliang Feng, and Junhong Chen. Crumpled nitrogen-doped graphene nanosheets with ultrahigh pore volume for high-performance supercapacitor. *Adv. Mater.*, 24(41):5610–6, November 2012.

[165] Zaiyong Mo, Ruiping Zheng, Hongliang Peng, Huagen Liang, and Shijun Liao. Nitrogen-doped graphene prepared by a transfer doping approach forthe oxygen reduction reaction application. *J. Power Sources*, 245:801–807, January 2014.

[166] Arava Leela Mohana Reddy, Anchal Srivastava, Sanketh R. Gowda, Hemtej Gullapalli, Madan Dubey, and Pulickel M. Ajayan. Synthesis of nitrogen-doped graphene films for lithium battery application. *ACS Nano*, 4(11):6337–42, November 2010.

[167] Liangti Qu, Yong Liu, Jong-Beom Baek, and Liming Dai. Nitrogen-doped graphene as efficient metal-free electrocatalyst for oxygen reduction in fuel cells. *ACS Nano*, 4(3):1321–6, March 2010.

[168] Yanguang Li, Ming Gong, Yongye Liang, Ju Feng, Ji-Eun Kim, Hailiang Wang, Guosong Hong, Bo Zhang, and Hongjie Dai. Advanced zinc-air batteries based on high-performance hybrid electrocatalysts. *Nat. Commun.*, 4(May):1805, January 2013.

[169] Ruifeng Zhou, Yao Zheng, Denisa Hulicova-Jurcakova, and Shi Zhang Qiao. Enhanced electrochemical catalytic activity by copper oxide grown on nitrogen-doped reduced graphene oxide. *J. Mater. Chem. A*, 1(42):13179, October 2013.

[170] Chang Hyuck Choi, Min Wook Chung, Han Chang Kwon, Jae Hoon Chung, and Seong Ihl Woo. Nitrogen-doped graphene/carbon nanotube self-assembly for efficient oxygen reduction reaction in acid media. *Appl. Catal. B Environ.*, 144:760–766, January 2014.

[171] Xiaosi Zhou, Li-Jun Wan, and Yu-Guo Guo. Binding SnO2 nanocrystals in nitrogen-doped graphene sheets as anode materials for lithium-ion batteries. *Adv. Mater.*, 25(15):2152–7, April 2013.

[172] Seung Woo Lee, Naoaki Yabuuchi, Betar M Gallant, Shuo Chen, Byeong-Su Kim, Paula T Hammond, and Yang Shao-Horn. High-power lithium batteries from functionalized carbon-nanotube electrodes. *Nat. Nanotechnol.*, 5(7):531–7, July 2010.

[173] Shankhamala Kundu, Yuemin Wang, Wei Xia, and Martin Muhler. Thermal Stability and Reducibility of Oxygen-Containing Functional Groups on Multiwalled Carbon Nanotube Surfaces: A Quantitative High-Resolution XPS and TPD/TPR Study. *J. Phys. Chem. C*, 112(43):16869–16878, October 2008.

[174] M.A. Montes-Morán, D. Suárez, J.A. Menéndez, and E. Fuente. On the nature of basic sites on carbon surfaces: an overview. *Carbon N. Y.*, 42(7):1219–1225, January 2004.

[175] K. Kinoshita and J.A.S. Bett. Potentiodynamic analysis of surface oxides on carbon blacks. *Carbon N. Y.*, 11(4):403–411, August 1973.

[176] Chunming Niu, Enid K. Sichel, Robert Hoch, David Moy, and Howard Tennent. High power electrochemical capacitors based on carbon nanotube electrodes. *Appl. Phys. Lett.*, 70(11):1480, March 1997.

[177] M. Bauscher and W. Maentele. Electrochemical and infrared-spectroscopic characterization of redox reactions of p-quinones. *J. Phys. Chem.*, 96(26):11101–11108, December 1992.

[178] Andrew F. Holloway, Gregory G. Wildgoose, Richard G. Compton, Lidong Shao, and Malcolm L. H. Green. The influence of edge-plane defects and oxygen-containing surface groups on the voltammetry of acid-treated, annealed and "super-annealed" multiwalled carbon nanotubes. *J. Solid State Electrochem.*, 12(10):1337–1348, May 2008.

[179] Tie-Zhen Ren, Lei Liu, Yuanyuan Zhang, and Zhong-Yong Yuan. Nitric acid oxidation of ordered mesoporous carbons for use in electrochemical supercapacitors. *J. Solid State Electrochem.*, 17(8):2223–2233, April 2013.

[180] Sebastian Osswald, Mickael Havel, and Yury Gogotsi. Monitoring oxidation of multiwalled carbon nanotubes by Raman spectroscopy. *J. Raman Spectrosc.*, 38(6):728–736, June 2007.

[181] Bing Zhao, Peng Liu, Yong Jiang, Dengyu Pan, Haihua Tao, Jinsong Song, Tao Fang, and Weiwen Xu. Supercapacitor performances of thermally reduced graphene oxide. *J. Power Sources*, 198:423–427, January 2012.

[182] Gea Jürmann, David J. Schiffrin, and Kaido Tammeveski. The pH-dependence of oxygen reduction on quinone-modified glassy carbon electrodes. *Electrochim. Acta*, 53(2):390–399, December 2007.

[183] F. Avilés, J.V. Cauich-Rodríguez, L. Moo-Tah, A. May-Pat, and R. Vargas-Coronado. Evaluation of mild acid oxidation treatments for MWCNT functionalization. *Carbon N. Y.*, 47(13):2970–2975, November 2009.

[184] Chien-To Hsieh and Hsisheng Teng. Influence of oxygen treatment on electric double-layer capacitance of activated carbon fabrics. *Carbon N. Y.*, 40(5):667–674, April 2002.

[185] Jun Yan, Qian Wang, Tong Wei, and Zhuangjun Fan. Recent Advances in Design and Fabrication of Electrochemical Supercapacitors with High Energy Densities. *Adv. Energy Mater.*, 4(4):1300816, March 2014.

[186] Chang Liu, Feng Li, Lai-Peng Ma, and Hui-Ming Cheng. Advanced materials for energy storage. *Adv. Mater.*, 22(8):E28–62, February 2010.

[187] François Béguin, Volker Presser, Andrea Balducci, and Elzbieta Frackowiak. Carbons and electrolytes for advanced supercapacitors. *Adv. Mater.*, 26(14):2219–51, 2283, April 2014.

[188] H.K. Jeong, H.J. Noh, J.Y. Kim, M.H. Jin, C.Y. Park, and Y.H. Lee. X-ray absorption spectroscopy of graphite oxide. *EPL (Europhysics Lett.)*, 82(6):67004, June 2008.

[189] Jigang Zhou, Paul N Duchesne, Yongfeng Hu, Jian Wang, Peng Zhang, Yanguang Li, Tom Regier, and Hongjie Dai. Fe-N bonding in a carbon nanotube-graphene complex for oxygen reduction: an XAS study. *Phys. Chem. Chem. Phys.*, 16(30):15787–91, August 2014.

[190] B.M. Messer, C.D. Cappa, J.D. Smith, K.R. Wilson, M.K. Gilles, R.C. Cohen, and R.J. Saykally. pH dependence of the electronic structure of glycine. *J. Phys. Chem. B*, 109(11):5375–82, March 2005.

[191] Jun Zhong, Jie Meng, Xianqing Liang, Li Song, Ting Zhao, Sishen Xie, Kurash Ibrahim, Haijie Qian, Jiaou Wang, Jinghua Guo, Haiyan Xu, and Ziyu Wu. XANES study of phenylalanine and glycine adsorption on single-walled carbon nanotubes. *Mater. Lett.*, 63(3-4):431–433, February 2009.

[192] Dah-Shyang Tsai, Chuan-hua Chang, Wei-Wen Chiang, Kuei-Yi Lee, and Ying-Sheng Huang. Effects of ion insertion on cycling performance of miniaturized electrochemical capacitor of carbon nanotubes array. *Nanotechnology*, 25(42):425401, October 2014.

[193] Denisa Hulicova-Jurcakova, Mykola Seredych, Gao Qing Lu, and Teresa J. Bandosz. Combined Effect of Nitrogen- and Oxygen-Containing Functional Groups of Microporous Activated Carbon on its Electrochemical Performance in Supercapacitors. *Adv. Funct. Mater.*, 19(3):438–447, February 2009.

[194] Xu Xiao, Tianqi Li, Peihua Yang, Yuan Gao, Huanyu Jin, Weijian Ni, Wenhui Zhan, Xianghui Zhang, Yuanzhi Cao, Junwen Zhong, Li Gong, WenChun Yen, Wenjie Mai, Jian Chen, Kaifu Huo, Yu-Lun Chueh, Zhong Lin Wang, and Jun Zhou. Fiber-based all-solid-state flexible supercapacitors for self-powered systems. *ACS Nano*, 6(10):9200–6, October 2012.

[195] Taeyoung Kim, Gyujin Jung, Seonmi Yoo, Kwang S. Suh, and Rodney S. Ruoff. Activated graphene-based carbons as supercapacitor electrodes with macro- and mesopores. *ACS Nano*, 7(8):6899–905, August 2013.

[196] Saikat Dutta, Asim Bhaumik, and Kevin C.-W. Wu. Hierarchically porous carbon derived from polymers and biomass: effect of interconnected pores on energy applications. *Energy Environ. Sci.*, 7(11):3574–3592, May 2014.

[197] Long Qie, Weimin Chen, Henghui Xu, Xiaoqin Xiong, Yan Jiang, Feng Zou, Xianluo Hu, Ying Xin, Zhaoliang Zhang, and Yunhui Huang. Synthesis of functionalized 3D hierarchical porous carbon for high-performance supercapacitors. *Energy Environ. Sci.*, 6(8):2497, July 2013.

[198] Da-Wei Wang, Feng Li, Min Liu, Gao Qing Lu, and Hui-Ming Cheng. 3D aperiodic hierarchical porous graphitic carbon material for high-rate electrochemical capacitive energy storage. *Angew. Chem. Int. Ed. Engl.*, 47(2):373–6, January 2008.

[199] Zhe Gui, Hongli Zhu, Eleanor Gillette, Xiaogang Han, Gary W Rubloff, Liangbing Hu, and Sang Bok Lee. Natural cellulose fiber as substrate for supercapacitor. *ACS Nano*, 7(7):6037–46, July 2013.

[200] Matthew E. Suss, Theodore F. Baumann, Marcus A. Worsley, Klint A. Rose, Thomas F. Jaramillo, Michael Stadermann, and Juan G. Santiago. Impedance-based study of capacitive porous carbon electrodes with hierarchical and bimodal porosity. *J. Power Sources*, 241:266–273, November 2013.

[201] Chau Tran and Vibha Kalra. Fabrication of porous carbon nanofibers with adjustable pore sizes as electrodes for supercapacitors. *J. Power Sources*, 235:289–296, August 2013.

[202] Charan Masarapu, Venkatachalam Subramanian, Hongwei Zhu, and Bingqing Wei. Long-Cycle Electrochemical Behavior of Multiwall Carbon Nanotubes Synthesized on Stainless Steel in Li Ion Batteries. *Adv. Funct. Mater.*, 19(7):1008–1014, April 2009.

[203] Randall L. Vander Wal and Lee J. Hall. Carbon nanotube synthesis upon stainless steel meshes. *Carbon N. Y.*, 41(4):659–672, January 2003.

[204] Carole E. Baddour, Faysal Fadlallah, Deniz Nasuhoglu, Reema Mitra, Leron Vandsburger, and Jean-Luc Meunier. A simple thermal CVD method for carbon nanotube synthesis on stainless steel 304 without the addition of an external catalyst. *Carbon N. Y.*, 47(1):313–318, January 2009.

[205] Apollo Expeditions to the Moon: Chapter 4. `http://history.nasa.gov/SP-350/ch-4-3.html`.

[206] Drew C. Higgins and Zhongwei Chen. Recent progress in non-precious metal catalysts for PEM fuel cell applications. *Can. J. Chem. Eng.*, 91(12):1881–1895, December 2013.

[207] Gang Wu, Karren L. More, Christina M. Johnston, and Piotr Zelenay. High-performance electrocatalysts for oxygen reduction derived from polyaniline, iron, and cobalt. *Science*, 332(6028):443–7, April 2011.

[208] Huilong Fei, Ruquan Ye, Gonglan Ye, Yongji Gong, Zhiwei Peng, Xiujun Fan, Errol L.G. Samuel, Pulickel M. Ajayan, and James M. Tour. Boron- and Nitrogen-Doped Graphene Quantum Dots/Graphene Hybrid Nanoplatelets as Efficient Electrocatalysts for Oxygen Reduction. *ACS Nano*, 8(10):10837–10843, October 2014.

[209] Yongye Liang, Hailiang Wang, Peng Diao, Wesley Chang, Guosong Hong, Yanguang Li, Ming Gong, Liming Xie, Jigang Zhou, Jian Wang, Tom Z Regier, Fei Wei, and Hongjie Dai. Oxygen reduction electrocatalyst based on strongly coupled cobalt oxide nanocrystals and carbon nanotubes. *J. Am. Chem. Soc.*, 134(38):15849–57, September 2012.

[210] P. Matter, L. Zhang, and U. Ozkan. The role of nanostructure in nitrogen-containing carbon catalysts for the oxygen reduction reaction. *J. Catal.*, 239(1):83–96, April 2006.

[211] Giuliano Mengoli. Feasibility of Polymer Film Coatings Through Electroinitiated Polymerization in Aqueous Medium. In *Electr. Phenom. Polym. Sci.*, pages 1–31. Springer, 1979.

[212] Frédéric Houzé, Lionel Boyer, Sophie Noël, Pascal Viel, Gérard Lécayon, and Jean-Michel Bourin. Electrical properties of very thin heat-treated polyacrylonitrile layers electropolymerized on nickel for contact application. *Synth. Met.*, 62(3):207–216, February 1994.

[213] Sabine Gabriel, Robert Jérôme, and Christine Jérôme. Cathodic electro-grafting of acrylics: From fundamentals to functional coatings. *Prog. Polym. Sci.*, 35(1-2):113–140, January 2010.

[214] Johanna Reuber, Helke Reinhardt, and Diethelm Johannsmann. Formation of surface-attached responsive gel layers via electrochemically induced free-radical polymerization. *Langmuir*, 22(7):3362–7, March 2006.

[215] Luís Miguel Santos, Jalal Ghilane, Claire Fave, Pierre-Camille Lacaze, Hyacinthe Randriamahazaka, Luisa Maria Abrantes, and Jean-Christophe Lacroix. Electrografting Polyaniline on Carbon through the Electroreduction of Diazonium Salts and the Electrochemical Polymerization of Aniline. *J. Phys. Chem. C*, 112(41):16103–16109, October 2008.

[216] Sarra Gam-Derouich, Samia Mahouche-Chergui, Mireille Turmine, Jean-Yves Piquemal, Dalila Ben Hassen-Chehimi, Mária Omastová, and Mohamed M. Chehimi. A versatile route for surface modification of carbon, metals and semi-conductors by diazonium salt-initiated photopolymerization. *Surf. Sci.*, 605(21):1889–1899, 2011.

[217] Seul Ki Kim and Seungwon Jeon. Improved electrocatalytic effect of carbon nanomaterials by covalently anchoring with CoTAPP via diazonium salt reactions. *Electrochem. commun.*, 22:141–144, August 2012.

[218] Yuewei Zhang, Jun Ge, Lu Wang, Donghong Wang, Feng Ding, Xiaoming Tao, and Wei Chen. Manageable N-doped graphene for high performance oxygen reduction reaction. *Sci. Rep.*, 3:2771, January 2013.

[219] Li-feng Chen, Xu-dong Zhang, Hai-wei Liang, Mingguang Kong, Qing-fang Guan, Ping Chen, and Chen E T Al. Synthesis of Nitrogen-Doped Porous Carbon Nanofibers as an Efficient Electrode Material for Supercapacitors. *ACS Nano*, 6(8):7092–7102, 2012.

[220] U.A. Paulus, T.J. Schmidt, H.A. Gasteiger, and R.J. Behm. Oxygen reduction on a high-surface area Pt/Vulcan carbon catalyst: A thin-film rotating ring-disk electrode study. *J. Electroanal. Chem.*, 495(2):134–145, January 2001.

[221] Rajesh Bashyam and Piotr Zelenay. A class of non-precious metal composite catalysts for fuel cells. *Nature*, 443(7107):63–6, September 2006.

[222] Shengwen Yuan, Jiang-Lan Shui, Lauren Grabstanowicz, Chen Chen, Sean Commet, Briana Reprogle, Tao Xu, Luping Yu, and Di-Jia Liu. A highly active and support-free oxygen reduction catalyst prepared from ultrahigh-surface-area porous polyporphyrin. *Angew. Chem. Int. Ed. Engl.*, 52(32):8349–53, August 2013.

[223] Jae Yeong Cheon, Taeyoung Kim, Yongman Choi, Hu Young Jeong, Min Gyu Kim, Young Jin Sa, Jaesik Kim, Zonghoon Lee, Tae-Hyun Yang, Kyungjung Kwon, Osamu Terasaki, Gu-Gon Park, Radoslav R Adzic, and

Sang Hoon Joo. Ordered mesoporous porphyrinic carbons with very high electrocatalytic activity for the oxygen reduction reaction. *Sci. Rep.*, 3:2715, January 2013.

[224] Rafael Silva, Damien Voiry, Manish Chhowalla, and Tewodros Asefa. Efficient metal-free electrocatalysts for oxygen reduction: polyaniline-derived N- and O-doped mesoporous carbons. *J. Am. Chem. Soc.*, 135(21):7823–6, May 2013.

[225] Chengzhou Zhu and Shaojun Dong. Recent progress in graphene-based nanomaterials as advanced electrocatalysts towards oxygen reduction reaction. *Nanoscale*, 5(5):1753–67, March 2013.

[226] Alexey Serov, Michael H. Robson, Mayat Smolnik, and Plamen Atanassov. Templated bi-metallic non-PGM catalysts for oxygen reduction. *Electrochim. Acta*, 80:213–218, October 2012.

Part III

Appendices

Appendix A

Stainless Steel Cleaning and Composition

Cleaning:

1) 316 Stainless steel is either used without roughening or roughen by hand using Dremel power tool with a Carbon Steel brush head.

2) Strips of roughen or non-roughen stainless steel are cleaned by sonication:

   (i) acetone for 15 mins

   (ii) isopropyl alcohol for 15 mins

   (iii) DI water for 15 mins

   (iv) samples are stored in DI water until ready

Please note that roughen samples left in DI water for too long will develop oxides in the rough crevices. These can easily be removed by quick (<30 sec) acid treatment.

Chemical composition:
The chemical composition of 316 stainless steel is: 65.345% Fe, 17% Cr, 12% Ni, 2.5% Mo, 2% Mn, 1% Si, 0.08% C, 0.045% P, 0.03% S.

Appendix B

Electropolymerization

To test the availability of metal-ions to produce polymeric films, 4VP monomer was tried to make P4VP. $ZnCl_2$, $Ni(NO_3)_2$, $FeCl_2$, and $CuCl_2$ were used as metal catalysts for polymerization. Polymerization took place in a 3-electrode cell following process detailed in **3.1.2**. Clean stainless steel strips are used as working electrodes, graphite rod as counter, and Ag/AgCl saturated in KCl as reference electrode. After deposition and drying, samples were analyzed with FTIR to check for C-C (1350–1500 cm^{-1}) and C-N ($\sim$1600 cm^{-1}) peaks, which are analogous to a successful polymerization. Figure B.1 compares the FTIR spectra of different metal-catalyzed polymer electrodepositions demonstrating that Zn and Ni are effective at producing polymer films.
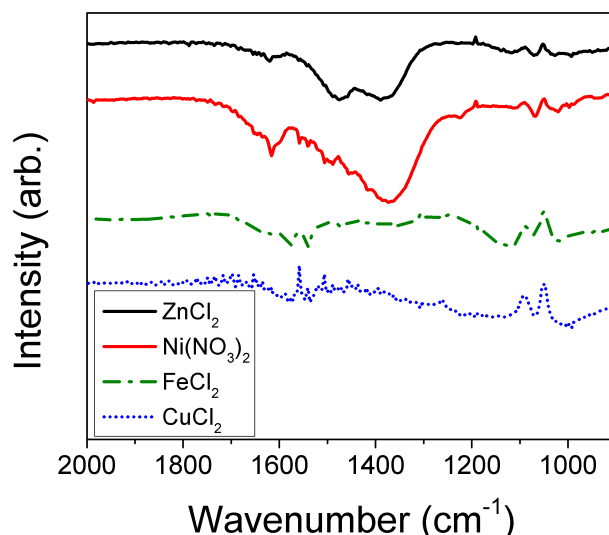

Figure B.1: FTIR comparison of different metal catalyst efficiency in electropolymerizing poly(4-vinylpyridine). Only zinc chloride and nickel nitrate are effective at producing polymer films.